

# UNDERWATER COMMUNICATIONS AND NETWORKING

GUEST EDITORS: CHARALAMPOS C. TSIMENIDIS, YURIY ZAKHAROV, CHRISTOPHE LAOT,  
KONSTANTINOS PELEKANAKIS, PAOLO CASARI, AND ANDREY K. MOROZOV





---

# **Underwater Communications and Networking**

## **Underwater Communications and Networking**

Guest Editors: Charalampos C. Tsimenidis, Yuriy Zakharov,  
Christophe Laot, Konstantinos Pelekanakis, Paolo Casari,  
and Andrey K. Morozov



---

Copyright © 2012 Hindawi Publishing Corporation. All rights reserved.

This is a special issue published in “Journal of Electrical and Computer Engineering.” All articles are open access articles distributed under the Creative Commons Attribution License, which permits unrestricted use, distribution, and reproduction in any medium, provided the original work is properly cited.

## Editorial Board

The editorial board of the journal is organized into sections that correspond to the subject areas covered by the journal.

### Circuits and Systems

M. T. Abuelma'atti, Saudi Arabia	Yong-Bin Kim, USA	Gabriel Robins, USA
Ishfaq Ahmad, USA	H. Kuntman, Turkey	Mohamad Sawan, Canada
Dhamin Al-Khalili, Canada	Parag K. Lala, USA	Raj Senani, India
Wael M. Badawy, Canada	Shen-Iuan Liu, Taiwan	Gianluca Setti, Italy
Ivo Barbi, Brazil	Bin-Da Liu, Taiwan	Jose Silva-Martinez, USA
Martin A. Brooke, USA	João A. Martino, Brazil	Nicolas Sklavos, Greece
Chip Hong Chang, Singapore	Pianki Mazumder, USA	Ahmed M. Soliman, Egypt
Y. W. Chang, Taiwan	Michel Nakhla, Canada	Dimitrios Soudris, Greece
Tian-Sheuan Chang, Taiwan	Sing K. Nguang, New Zealand	Charles E. Stroud, USA
Tzi-Dar Chiueh, Taiwan	Shun-ichiro Ohmi, Japan	Ephraim Suhir, USA
Henry S. H. Chung, Hong Kong	Mohamed A. Osman, USA	Hannu Tenhunen, Sweden
M. Jamal Deen, Canada	Ping Feng Pai, Taiwan	George S. Tombras, Greece
Ahmed El Wakil, UAE	Marcelo A. Pavanello, Brazil	Spyros Tragoudas, USA
Denis Flandre, Belgium	Marco Platzner, Germany	Chi Kong Tse, Hong Kong
P. Franzon, USA	Massimo Poncino, Italy	Chi-Ying Tsui, Hong Kong
Andre Ivanov, Canada	Dhiraj K. Pradhan, UK	Jan Van der Spiegel, USA
Ebroul Izquierdo, UK	F. Ren, USA	Chin-Long Wey, USA
Wen-Ben Jone, USA		

### Communications

Sofiène Affes, Canada	Amoakoh Gyasi-Agyei, Ghana	Samuel Pierre, Canada
Dharma Agrawal, USA	Yaohui Jin, China	Nikos C. Sagias, Greece
H. Arslan, USA	Mandeep Jit Singh, Malaysia	John N. Sahalos, Greece
Edward Au, China	Peter Jung, Germany	Christian Schlegel, Canada
Enzo Baccarelli, Italy	Adnan Kavak, Turkey	Vinod Sharma, India
Stefano Basagni, USA	Rajesh Khanna, India	Ickho Song, Korea
Jun Bi, China	Kiseon Kim, Republic of Korea	Ioannis Tomkos, Greece
Z. Chen, Singapore	D. I. Laurenson, UK	Chien Cheng Tseng, Taiwan
René Cumplido, Mexico	Tho Le-Ngoc, Canada	George Tsoulos, Greece
Luca De Nardis, Italy	C. Leung, Canada	Laura Vanzago, Italy
M.-Gabriella Di Benedetto, Italy	Petri Mähönen, Germany	Roberto Verdone, Italy
J. Fiorina, France	Mohammad A. Matin, Bangladesh	Guosen Yue, USA
Lijia Ge, China	M. Nájjar, Spain	Jian-Kang Zhang, Canada
Z. Ghassemlooy, UK	M. S. Obaidat, USA	
K. Giridhar, India	Adam Panagos, USA	

### Signal Processing

S. S. Aghaian, USA	A. G. Constantinides, UK	Karen Egiazarian, Finland
Panajotis Agathoklis, Canada	Paul Dan Cristea, Romania	W.-S. Gan, Singapore
Jaakko Astola, Finland	Petar M. Djuric, USA	Z. F. Ghassemlooy, UK
Tamal Bose, USA	Igor Djurović, Montenegro	Ling Guan, Canada



---

Martin Haardt, Germany  
Peter Handel, Sweden  
Andreas Jakobsson, Sweden  
Jiri Jan, Czech Republic  
S. Jensen, Denmark  
Chi Chung Ko, Singapore  
M. A. Lagunas, Spain  
J. Lam, Hong Kong  
D. I. Laurenson, UK  
Riccardo Leonardi, Italy  
S. Marshall, UK

Antonio Napolitano, Italy  
Sven Nordholm, Australia  
S. Panchanathan, USA  
Periasamy K. Rajan, USA  
Cédric Richard, France  
W. Sandham, UK  
Ravi Sankar, USA  
Dan Schonfeld, USA  
Ling Shao, UK  
John J. Shynk, USA  
Andreas Spanias, USA

Yannis Stylianou, Greece  
Ioan Tabus, Finland  
Jarmo Henrik Takala, Finland  
Clark N. Taylor, USA  
A. H. Tewfik, USA  
Jitendra Kumar Tugnait, USA  
Vesa Valimaki, Finland  
Luc Vandendorpe, Belgium  
Ari J. Visa, Finland  
Jar Ferr Yang, Taiwan

# Contents

---

**Underwater Communications and Networking**, Charalampos C. Tsimenidis, Yuriy Zakharov, Christophe Laot, Konstantinos Pelekanakis, Paolo Casari, and Andrey K. Morozov  
Volume 2012, Article ID 214012, 2 pages

**Location-Aware Source Routing Protocol for Underwater Acoustic Networks of AUVs**, Edward A. Carlson, Pierre-Philippe J. Beaujean, and Edgar An  
Volume 2012, Article ID 765924, 18 pages

**Information-Theoretic Analysis of Underwater Acoustic OFDM Systems in Highly Dispersive Channels**, Francois-Xavier Socheleau, Milica Stojanovic, Christophe Laot, and Jean-Michel Passerieux  
Volume 2012, Article ID 716720, 15 pages

**Compensation of Linear Multiscale Doppler for OFDM-Based Underwater Acoustic Communication Systems**, A. E. Abdelkareem, B. S. Sharif, C. C. Tsimenidis, and J. A. Neasham  
Volume 2012, Article ID 139416, 16 pages

**Underwater Localization and Tracking of Physical Systems**, Patrick Carroll, Shengli Zhou, Hao Zhou, Xiaoka Xu, Jun-Hong Cui, and Peter Willett  
Volume 2012, Article ID 683919, 11 pages

**Performance Comparison of Doppler Scale Estimation Methods for Underwater Acoustic OFDM**, Lei Wan, Zhaohui Wang, Shengli Zhou, T. C. Yang, and Zhijie Shi  
Volume 2012, Article ID 703243, 11 pages

## Editorial

# Underwater Communications and Networking

**Charalampos C. Tsimenidis,<sup>1</sup> Yuriy Zakharov,<sup>2</sup> Christophe Laot,<sup>3</sup>  
Konstantinos Pelekanakis,<sup>4</sup> Paolo Casari,<sup>5</sup> and Andrey K. Morozov<sup>6</sup>**

<sup>1</sup> School of Electrical and Electronic Engineering, Newcastle University, Merz Court, Newcastle upon Tyne NE1 7RU, UK

<sup>2</sup> Department of Electronics, University of York, Heslington, York YO10 5DD, UK

<sup>3</sup> Institut Mines-Télécom, Telecom Bretagne, UMR CNRS 6285 Lab—STICC, Université Européenne de Bretagne, Technopôle Brest Iroise, CS 83818, 29238 Brest Cedex, France

<sup>4</sup> Acoustic Research Laboratory, National University of Singapore, 12A Kent Ridge Road, Singapore 119223

<sup>5</sup> Department of Information Engineering, University of Padova, Via G. Gradenigo, 6/B, 35131 Padova, Italy

<sup>6</sup> Applied Ocean Physics and Engineering, Woods Hole Oceanographic Institution, MS No. 9, Bigelow 404, Woods Hole, MA 02543, USA

Correspondence should be addressed to Charalampos C. Tsimenidis, charalampos.tsimenidis@ncl.ac.uk

Received 13 December 2012; Accepted 13 December 2012

Copyright © 2012 Charalampos C. Tsimenidis et al. This is an open access article distributed under the Creative Commons Attribution License, which permits unrestricted use, distribution, and reproduction in any medium, provided the original work is properly cited.

In the last two decades, we have witnessed growing research interest in underwater communications and networks for civilian and scientific, as well as military type of applications. Despite the plethora of studies in this area, the hostile nature of the propagation medium poses many challenging issues, many of which are still to be solved. The underwater acoustic communications channel (UAC) can be characterized in most cases as a doubly spread channel. This implies that UAC exhibits both delay and Doppler spread. Delay spread leads to time dispersion and frequency selective fading effects. In contrast, time dispersion dilates the transmitted symbol duration in time and needs to be compensated prior to detection. In this special issue, five original technical contributions are addressing problems that will advance the development of next generation underwater communication technologies.

One core high data rate modulation technology that has found its way in modern underwater modem design is Orthogonal Frequency Division Multiplexing (OFDM). OFDM is an efficient method to tackle delay spread induced intersymbol interference (ISI) in underwater acoustic communications. However, a long cyclic prefix is often required and therefore the bandwidth efficiency of the system is reduced. The authors in “*Information-theoretic analysis of underwater acoustic OFDM systems in highly dispersive*

*channels*” quantitatively analyze the interplay between interference, namely ISI and intercarrier interference (ICI), and maximum transmission rate of the OFDM system. This is accomplished by computing the capacity of OFDM in a doubly spread channel but without relying on the commonly used assumption of the uncorrelated scattering model.

The motion induced time-selectivity of UAC manifests itself as a both frequency or Doppler shift and signal dilation. In multicarrier transmissions employing OFDM, a Doppler shift will introduce ICI to the adjacent subcarriers. Resampling of the received signal will remove both effects, however, leaving residual carrier frequency offsets that need to be compensated. The authors in “*Compensation of linear multiscale doppler for OFDM-based underwater acoustic communication systems*” investigate the performance of multi-scale Doppler shift compensation in OFDM UAC. It was demonstrated that the proposed algorithms employing coarse timing synchronization can deal with time-varying linear acceleration during a packet made of multiple OFDM frames. In “*Performance comparison of Doppler scale estimation methods for underwater acoustic OFDM*”, the authors compared several Doppler scale estimation methods for zero-padded OFDM systems using a cyclic-prefixed preamble. It is demonstrated that blind approaches exploiting the underlying packet structure work very well at medium to

high signal to noise ratio ranges, although full or partial knowledge of the transmitted waveform may be required.

The authors in “*Underwater localization and tracking of physical systems*” address the problem of localization in underwater wireless sensor networks using an OFDM-based physical layer. In many applications, whether civilian or military, the meaningful interpretation of sensed data requires location-aware sensors. This paper presents an underwater localization approach based on one-way message broadcasting from multiple surface nodes. The performance of the proposed solution is evaluated using both simulation and measured results from experiments conducted in a swimming pool and in a local lake using a mobile receiver.

The problem of routing over multihop paths with time-varying link quality is considered in “*Location-aware source routing protocol for underwater acoustic networks of AUVs*”. The authors present the design of a location-aware source routing (LASR) protocol for underwater networks. LASR is based on the sharing of a common time reference between network nodes. Such reference is exploited both for administering multiple access, and for the timely detection of topological changes in the network. LASR is loosely inspired to the Dynamic Source Routing (DSR) protocol. With respect to DSR, LASR employs a different routing metric (cf., the expected number of transmissions before correctly delivering a packet to its destination) and relaxes the source routing approach, by letting the nodes downstream modify the route if topological changes occur. Several mechanisms are employed to improve the effectiveness of multihop communications: these include imposing time constraints over implicit or explicit acknowledging, and performing route maintenance via opportunistic overhearing of neighboring control and data traffic. Simulation results show the good performance of LASR with respect both to a baseline flooding protocol and to DSR, under several environmental and link reliability conditions.

We hope that both academic researchers and engineers working in the area of underwater communications and networking will find the papers presented in this special issue useful and that the contributions and research outcomes in these papers may act as a stepping stone to support future research in this subject.

*Charalampos C. Tsimenidis*

*Yuriy Zakharov*

*Christophe Laot*

*Konstantinos Pelekanakis*

*Paolo Casari*

*Andrey K. Morozov*

## Research Article

# Location-Aware Source Routing Protocol for Underwater Acoustic Networks of AUVs

**Edward A. Carlson, Pierre-Philippe J. Beaujean, and Edgar An**

*Department of Ocean and Mechanical Engineering, Florida Atlantic University, 777 Glades Road, Boca Raton, FL 33431, USA*

Correspondence should be addressed to Pierre-Philippe J. Beaujean, pbeaujea@fau.edu

Received 9 May 2012; Revised 13 August 2012; Accepted 6 September 2012

Academic Editor: Paolo Casari

Copyright © 2012 Edward A. Carlson et al. This is an open access article distributed under the Creative Commons Attribution License, which permits unrestricted use, distribution, and reproduction in any medium, provided the original work is properly cited.

Acoustic networks of autonomous underwater vehicles (AUVs) cannot typically rely on protocols intended for terrestrial radio networks. This work describes a new location-aware source routing (LASR) protocol shown to provide superior network performance over two commonly used network protocols—flooding and dynamic source routing (DSR)—in simulation studies of underwater acoustic networks of AUVs. LASR shares some features with DSR but also includes an improved link/route metric and a node tracking system. LASR also replaces DSR's shortest-path routing with the expected transmission count (ETX) metric. This allows LASR to make more informed routing decisions, which greatly increases performance compared to DSR. Provision for a node tracking system is another novel addition: using the time-division multiple access (TDMA) feature of the simulated acoustic modem, LASR includes a tracking system that predicts node locations, so that LASR can proactively respond to topology changes. LASR delivers 2–3 times as many messages as flooding in 72% of the simulated missions and delivers 2–4 times as many messages as DSR in 100% of the missions. In 67% of the simulated missions, LASR delivers messages requiring multiple hops to cross the network with 2–5 times greater reliability than flooding or DSR.

## 1. Introduction

As autonomous underwater vehicles (AUVs) continue to become less expensive and more capable, they are being deployed in larger groups. As a result, the need to communicate between multiple, mobile underwater systems is growing as well. Underwater communication is best accomplished through the use of acoustic links, and interconnecting multiple underwater vehicles is best accomplished through the use of an acoustic network. Such a network, one using a shared medium and comprising mobile nodes, is called a mobile ad hoc network (MANET). It is difficult to efficiently forward data across a MANET because node mobility means network topology—the overall set of connections between nodes—changes over time. The network must spontaneously organize, learn the topology, and begin routing with a minimum of overhead traffic for route discovery and maintenance. There has been a great deal of attention paid to this problem, but almost exclusively as it applies to wireless radio networks [1–4].

In a network, a node is a communication endpoint able to send and receive data. When two nodes can communicate with one another, they are said to have a link between them. Links can be of varying quality: some links may deliver almost every message without error, others may deliver only a small fraction of the messages sent across them. In shared-medium communications like underwater acoustics, every transmission has exactly one sender but can have one or more receivers.

A message may have to be forwarded across one or more links to intermediate nodes before reaching its intended destination. Routing is the process of choosing the links that will comprise the route the message will follow across the network. A routing protocol is responsible for selecting the route. Most routing protocols collect, manage, and disseminate information about the network in order to function, for example, by monitoring network topology, specifying the next hop of a message, queuing messages awaiting routes, and tracking which messages have already been processed. Unlike in a traditional, wired network,

routing in a mobile ad hoc network (MANET) is complicated by the possibly rapid and unpredictable topological changes caused by movement of the nodes. A given routing protocol is typically intended for a particular type of network, and many have been developed specifically for MANETs [5–9].

Little of the existing research into MANET routing protocols addresses the specific limitations of underwater acoustics [10]. While few MANETs are as drastically low-bandwidth as an underwater acoustic network, many have little bandwidth when compared with wired networks, and some MANET techniques specifically address this by reducing protocol overhead [11–13]. The greater problem is that the existing research assumes—almost without exception—that wireless networks in general, and MANETs in particular, use radio links.

The particular problem is the speed of the nodes compared to the communication latency. Most advanced routing protocols need to propagate topology information throughout the network. The high latency of acoustic links means that the movement of underwater vehicles can change the network topology more quickly than updates can be propagated. This is especially a problem for protocols developed for radio MANETs, which overall assume a much slower rate of topology change compared to communication latency [11–17].

This paper describes the location-aware source routing (LASR) protocol, a network routing protocol specifically designed for use in low-bandwidth, high-latency underwater acoustic networks of mobile nodes. LASR is loosely based on the dynamic source routing (DSR) [9] protocol and is specifically designed for use in underwater acoustic networks where the topology changes frequently. The results presented here show that, in simulated underwater acoustic networks of AUVs, LASR outperforms both blind flooding and DSR in throughput and packet delivery ratio. Note that LASR is intended for use in missions where vehicle movement dominates energy consumption, so that it maximizes successful communication rather than energy conservation. A performance comparison between protocols in terms of energy consumption is not the focus of this publication, but it is an important future study.

The remainder of this paper is organized as follows. Related work is discussed in Section 2. The new LASR protocol is described in Section 3. Specifics of handling routes and messages are covered in Section 4. Section 5 presents some results of LASR in a simulated underwater network. Section 6 summarizes our conclusions.

## 2. Literature Review and Background

**2.1. Medium Access Control.** Radio and acoustics are both shared medium techniques: multiple senders and receivers use the same medium (e.g., the water of the ocean) and there must be some sort of medium access control (MAC) to keep them from all “talking at once”. Inherent in shared-medium systems is the problem of collision—the interference among multiple, simultaneously-received signals. A large number of

MAC protocols have been developed, some better suited to mobile underwater acoustic use than others [10, 18–24].

Time-division multiple access (TDMA) divides the medium into time-slots [4]. Each node may use the entire bandwidth, but may only transmit according to a given schedule. LASR must use TDMA as its MAC protocol. The TDMA transmit-time information is what allows LASR to collect implicit time-of-flight information for the nodes in the network and is crucial for effective use of its tracking system.

**2.2. Blind Flooding.** Blind flooding is a network broadcasting protocol [4], and the simplest of the flooding protocols. It delivers its messages to every node in the network, and does so without knowledge of the topology. The basic operation is simple: the first time a node receives a given message, the node automatically rebroadcasts it. Because blind flooding does not require the topology to be known, many of the more-sophisticated routing protocols employ it before routes are known, for example, during route discovery. Blind flooding’s advantages include operation without topological information and low end-to-end delay. The main disadvantage of blind flooding is that it can produce a significant amount of unnecessary traffic, especially as the size of the network increases.

**2.3. Shortest-Path Routing.** Flooding delivers a message by network broadcast, and every node in the network receives the message. This is very inefficient when the destination is a single node. An alternative is shortest-path routing, where a message follows the path with the fewest hops. This is much more efficient: rather than every node in the network forwarding the message to all its neighbors by broadcast, each node along the shortest path forwards the message to the next hop by unicast. However, this makes it necessary for the network nodes to have at least partial knowledge of the network topology. It is also important to avoid routing loops, which occur when mismatches in topology information across several nodes cause messages to be routed in circles.

Examples of shortest-path routing include the Destination-Sequenced Distance Vector (DSDV) protocol [5], Ad hoc On-demand Distance Vector (AODV) [6], Topology Dissemination Based on Reverse-Path Forwarding (TBRPF) [8], and the Temporally-Ordered Routing Algorithm (TORA) [7]. Of particular interest here is the Dynamic Source Routing (DSR) protocol [9], a reactive protocol which, depending on the implementation, uses either distance-vector or link-state routing. In source routing, the entire route to the destination is determined by the originator (the source) and is carried along with the message. Routes are discovered as needed via a route-request/route-reply process, and there are no periodic updates.

**2.4. Delay-Tolerant Routing.** In some networks, there may never be an end-to-end connection. Instead, individual mobile nodes must hold data until a forwarding opportunity arises [25]. For example, a protocol can exploit vehicles’ non-random mobility patterns to improve routing performance

[26]. These routing techniques are not necessarily suitable to the cooperating-AUVs problem. When cooperating, the nodes will likely actively work to stay connected, that is, each node will maneuver such that it always stays within range of the network. More importantly, certain types of data do not need to be delivered immediately and can tolerate significant delay in their delivery, but when cooperating on short time-scales, some communication is very likely to be time-sensitive and delivery cannot wait long periods for an opportune vehicle motion to put it in range.

*2.5. Position-Based and Location-Aware Routing.* A routing protocol spends most of its time determining and tracking the network topology. With communication technologies such as radio and acoustics, which links are available largely depends on the distance between the various nodes. Some routing protocols use knowledge of the location of network nodes to provide or augment topology information. These are known as location-aware or position-based protocols.

Routing by absolute geographical location typically employs a locating service that is queried by nodes to look-up the current location of a destination node. Messages are routed to the neighbor that is geographically nearest to the destination. Routing by relative location typically requires both relative location (e.g., range and bearing) as well as traditional topology information. LASR routes by relative location.

A protocol similar to LASR is [27], which also estimates range from one-way time-of-flight using TDMA and uses it to discover network topology for routing via DSR. However, it includes pseudonoise probe patterns as a part of each frame because localization is of primary importance in that system. The network supports only very few nodes and the overall communication rate is extremely low.

### 3. New Protocol

*3.1. Overview of the Specific Aspects of LASR.* The new LASR protocol has been specifically designed to address the problems of routing in low-bandwidth, high-latency underwater acoustic networks of mobile nodes. It is loosely based on the DSR [9] protocol. Like DSR, LASR is a self-organizing, infrastructureless, distributed protocol. It learns and maintains only those routes that are in use.

LASR uses the source route principally as a means to communicate topology information. Each intermediate node updates the source route in every message it forwards, applying the route most likely to require the fewest transmissions (which does not necessarily correspond to the fewest hops) to reach the destination. Every message transmission is therefore routed according to the most current topological knowledge, rather than DSR's approach which routes according to the topological knowledge at the time the message was originated.

*3.2. Assumptions.* The LASR protocol is designed for small underwater networks using low-speed acoustic links. The

network should not contain more than 20–30 nodes, a reasonable assumption given typical multiple-AUV operations such as [28]. This network size limitation is due in lesser part to the source route header overhead in each message. The size of the source route grows linearly with the length of the longest path through the network. In greater part, this assumption is due to LASR's required use of TDMA, which does not scale well into large networks.

Nodes may move at any time and in any direction. The only restriction on node motion is that speeds should be in the range 0–3 m/s; this speed range is typical for most current AUVs. This assumption is necessary to limit the rate at which node motion can change the network topology.

All nodes must use identical LASR algorithms, and all must fully participate in the protocol, including forwarding the messages of others.

Every node must have accurate timekeeping, for example, by means of a low-drift clock. No two node clocks may differ by more than 50 milliseconds throughout a mission, although this network time may differ from true time by any amount. This is necessary for TDMA window timing. Equipped with the optional time synchronization feature, the FAU Dual Purpose Acoustic Modem (DPAM) fits this requirement over 8 hours using low-drift clocks [29]. Also, prior work [30] has shown that for LASR, this is the minimum timekeeping precision necessary to preserve the accuracy of the time-of-flight range estimates based on TDMA window timing.

The communication link endpoints should be identical acoustic modems, and these modems should be effectively omnidirectional. They must support overhearing—the reception of messages not specifically addressed to them. Overhearing is an important source of topology information. To allow the tracking system to function, each modem must report the time at which any incoming transmission is detected, regardless of whether or not the transmission can be successfully decoded. The detection time reporting must be accurate to within 30 milliseconds. As with the timekeeping precision, this reporting precision has been shown [30] to be the minimum necessary for time-of-flight range estimate accuracy.

LASR's implementation of ETX assumes that network links are bidirectional (acoustic modem links are traditionally bidirectional, albeit half-duplex) and symmetrical, meaning packets can cross the link between any pair of nodes in either direction with equal probability of success. In practice, the links are not perfectly symmetrical, but symmetry is a fair assumption so long as the transducer is assumed omnidirectional and the environmental conditions (and range between nodes) do not change significantly between two transmissions. The development of a nonsymmetrical and unidirectional version of LASR is beyond the scope of this article, but constitutes a future key for development of LASR. The links are assumed to be through a shared medium. The network must use TDMA as the MAC protocol so that implicit time-of-flight range estimate is possible.

The ETX implementation also assumes that a medium model exists for the modem, which can provide a reasonably accurate estimate of the frame-error rate (FER) between

two modems given the distance between them. The FER is the probability that a given transmission (a frame) on the link will be received in error. All nodes must use identical medium models and the FER estimate must be deterministic: every use of the model at every node must return the same FER for a given range. Note that the FER model includes other input parameters (sea state, ambient noise, water depth, bottom type . . .). A complete list is provided in [31]. The FER model used in the simulation was developed from field data [32]. For simplicity, the study assumes that every input parameter is constant, with the exception of range. These other parameters impact the FER, thus the LASR performance. At fixed range, the authors showed in [33] that the LASR performance drops with ambient noise and sea state, as the FER increases with these two parameters.

A range-only tracking system is assumed to be available at each node. Regular measurements of the distance from the local node to each of the various other nodes within detection range will be available from a combination of the modem's transmission detection and TDMA window timing. The tracking system must use those time-of-flight based range measurements to predict the current location of those nodes relative to the local node. Prior work [30] has shown that the tracking system must predict relative node position to within 200 m of the true relative node position. If the estimated prediction error exceeds this amount for a given node, the tracking system must cease reporting the predicted position of that node.

**3.3. Link Metric.** The expected transmission count (ETX) [34] estimates the number of times a node will have to transmit a message before it successfully receives an acknowledgment. The ETX of a route is simply the sum of the ETXs of each link in the route, and any two ETX route metrics are directly comparable. The ETX is calculated from a link's FER. The technique described in [34] to calculate the ETX uses probe messages sent periodically across a link—once a sufficient number of probe messages have been sent, it is possible to estimate the link's FER, and then to calculate the ETX.

In a MANET however, node motion can cause considerable variation in link quality over short time scales. This is a problem because, while ETX outperforms hop-count in a static network, hop-count can react more quickly to link changes and outperforms ETX when nodes are moving [35].

LASR uses expected transmission count (ETX), but overcomes this mobile-node measurement-delay problem by calculating the delivery ratio directly from the FER estimated by the medium model. LASR assumes symmetric links, so the probability that a message and its acknowledgement will cross a link successfully is  $(1 - \text{FER})^2$ , making the equation for ETX:

$$\text{ETX} = \frac{1}{(1 - \text{FER})^2}. \quad (1)$$

How LASR handles the ETX information is described in Appendix B.

**3.4. Tracking System.** Neighborhood topology is predicted by the tracking system based on information from both implicit and explicit communication. Combining the time-of-detection information from the modem with the current TDMA state provides both an estimated time-of-flight and the identity of the transmitter. The range to the transmitter can then be estimated using the medium model.

A series of range estimates to other nodes, coupled with knowledge of a node's own motion, can form the basis for localization and tracking of the other nodes. When combined with minimal information from the other nodes about their ranges to each other, the relative, progressive location of the other nodes can usually be uniquely determined to some accuracy.

A tracking system was not implemented as part of this work. The behavior of the tracking system was simulated based on the minimum established performance requirements. A recursive state-estimation filter, such as a particle filter, is expected to be able to localize and track some or all of the network nodes, depending on the amount of information available about each node. The more information that is available about another node, the more accurate tracking and location prediction can be. Even a low-order motion model (e.g., maximum, minimum, and typical speed and turning rate) will help constrain tracking and prediction uncertainty. A behavior model providing knowledge of the types of behaviors the node may exhibit (e.g., lawn mowing, line-following or hovering) can further reduce uncertainty.

Information for tracking can be characterized as either explicit or implicit. Explicit information is carried as overhead in network messages. The LASR source routes, for example, carry explicit link range information. Implicit information is communicated without overhead, simply by the act of communicating. An example of implicit information is the time-of-flight measured when a message is received.

Some modems, such as the FAU DPAM [31], preface each packet with a known sequence of symbols. The optional time synchronization feature of the FAU DPAM is used for TDMA communications and tracking [29]. This detection sequence is used by the receiver to identify an incoming transmission because, unlike the coded variable data in a message, the symbols in the detection sequence are known a priori, making them substantially easier to identify, even in very weak signals. It is frequently possible to correctly identify the detection sequence in transmissions from ranges far beyond the range at which there is sufficient signal to successfully decode the variable data.

Under such modems, incoming transmissions fall into three categories: strong enough to decode (providing implicit range and explicit data), strong enough to detect but too weak to decode (providing implicit range only), and too weak to detect (providing nothing). Because the detection sequence can be reliably identified even across a link with an extremely high FER, the second category includes transmissions from nodes far beyond the useful explicit range of the modem. A comparison of implicit and explicit data is shown in Figure 1.

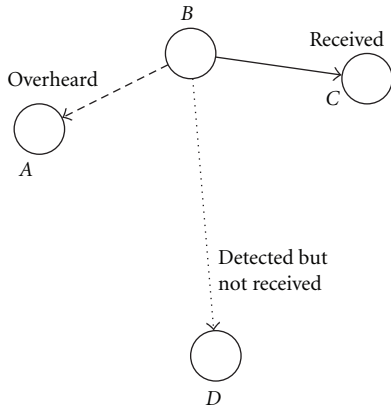


FIGURE 1: Implicit versus explicit data. Node B transmits a message for node C. Nodes A and C each detect and receive it (the message is intended for C, but A has overheard it). The detection provides an implicit range estimate to node B; the reception provides all of the explicit routing information contained in the message (e.g., in the source route). Node D detects but does not receive the message, thus D gains an implicit range estimate to node B but gets none of the explicit data.

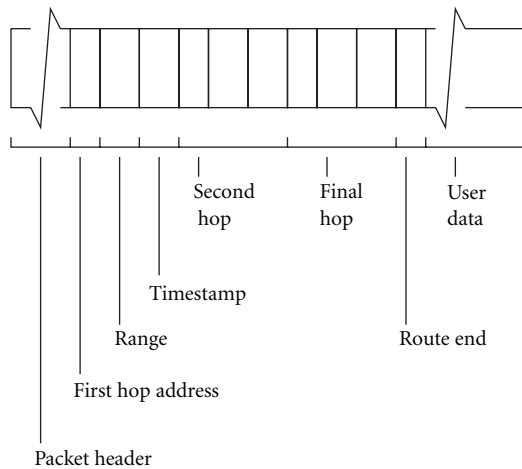


FIGURE 2: The LASR header is a variable-size stack of bits. This shows the source route portion of a three-hop route.

3.5. *LASR Packet Structure.* Each LASR packet contains one or more messages. A message can contain user data or protocol data. A user-data message contains a source-route in addition to the user data. There are several protocol message types; these are described in Appendix A.

Packets are small in a typical acoustic network, typically on the order of tens to hundreds of bytes only. This makes header overhead very expensive as even a small header can represent a large fraction of a packet. LASR uses a different header structure than DSR in order to reduce the size of the header as much as possible. LASR's header structure is shown in Figure 2. The number of bits added to the header by a given layer can change from message to message. To accommodate this, the header is implemented as a stack of bits.

A source route is structured as a series of triples followed by an end marker. Each triple is a hop in the route starting at the originator and ending one hop before the destination. A triple comprises the address of the node, the best-available estimate of the range from the node to the next hop (or the destination) and the timestamp of the range estimate. Both the range and its timestamp are quantized to conserve space in the header, see [30] for details on the quantization. The route end is the special network address zero, which is never a valid address. The network addresses are represented as the smallest number of bits that can represent the number of nodes in the network, plus one for the special zero address. For example, a 16 node network would require 17 unique addresses and would therefore require 5-bit addresses.

3.6. *Data Structures.* The protocol maintains several data structures at each node to maintain knowledge of the topology and the state of the various messages that the node must handle. The pending buffer holds messages awaiting transmission. The link cache stores network topology as information on links between pairs of nodes. The buffers are limited only by available memory. Tables such as the route-discovery, route-reply and route-request tables are used to limit the transmission of unnecessary or redundant protocol messages. The route-advice table prioritizes topology propagation messages. The data structures are described in Appendix C.

## 4. Management of Routes and Messages

4.1. *Route Discovery.* LASR is source-routed: when a message is sent across the network, the message must carry its route as part of its data. If a node, either the originator or an intermediate, has a message to transmit but is not able to find a suitable route in the data provided by its link cache and tracking system, it must defer sending the message and initiate route discovery by sending a route-request message.

The originated route-request message contains only an ID assigned by the originator. This ID, combined with the address of the originator, allows the route request to be uniquely identified in the network. A circular ID is used to conserve space in the message.

Before originating a route-request message to a given destination, a node must first check its route-discovery table. If a route request for that destination is already outstanding, the route request is not sent. This prevents a node from overloading the network with redundant route requests.

The route-request message is propagated through the network by flooding, as flooding is an efficient way to reach all the nodes in the network when the network topology is not known. When a node receives a route-request message, it is handled in one of three ways.

- (1) If the route-request's destination is the local node, it checks its route-reply table to determine if it should respond with a route-reply message. If it should, a route reply is originated with the destination set to be the originator of the route request. If not, the route request is dropped.

- (2) If the local node is not the destination and the route request has already been forwarded (if its unique ID appears in the route-request table), the route request is dropped.
- (3) Otherwise, the route request is enqueued for forwarding.

Whenever a route-request message is forwarded, it contains the best-available route from the originator to the forwarding node. This route is added to the link cache of each intermediate node and the destination node. In this way, route requests propagate topology information through the network, eventually providing the destination with a route back to the originator.

Due to the nature of flooding, a given route-request message can be duplicated many times as it propagates through the network and different copies can arrive at the destination at different times. When sending, LASR always chooses the best route currently available; if the same route is always best over multiple receptions of the same route request, multiple route replies would be sent, all containing the same data. To avoid such redundancy, a second or further route-reply message is originated only if a better route is available than the previous route reply to the same route request. This is determined by consulting the route-reply table (see Appendix C).

**4.2. Route Maintenance.** Route maintenance uses the implicit data from detected transmissions and the explicit data from received messages. A detected transmission provides an update to the tracking system. If a received message contains topology information, for example, the route in a route-request or route-reply message, this is used to update the link cache (see Appendix C). Received messages do not need to be for the local node to be useful. Overheard messages are an important source of topological information.

Received explicit topological information, whether from overheard messages or not, is processed by the link cache. Newer data are used to update the link cache. Older received data are used to update the route-advice table to help prioritize the sending of topology updates.

**4.3. Send Algorithm and Route Handling.** LASR sends a packet every time the local TDMA time-slot is open. It chooses the next message based from its fair-queue of user-data and protocol messages. If there are no pending messages, LASR will send a route-advice protocol message. This results in additional energy consumption, justified by the fact that LASR is designed to maximize successful communication rather than energy conservation. Again, LASR is intended for use in AUVs where vehicle movement dominates power consumption.

In DSR, a source route does not change except in special circumstances, for example, when a message is salvaged following the detection of a failed link. However, in an underwater acoustic network, the topology may change extremely quickly compared to the network latency, and a source route that was valid when a message was originated may become stale before the message has reached its destination.

To overcome this, LASR recomputes the route at every hop: the source routes serve mainly to disseminate topology information. When a message carrying a route is received, its route is read, the link cache is updated with any newer data, and older data are noted for future advising. The message then is queued without its route but with sufficient information for LASR to find for it a replacement route.

Immediately before a routed message is transmitted, it receives a completely new route from the cache. Timestamped link information ensures that a message always departs with the most up-to-date route information possible. When searching for a route, the cache first gets an updated prediction of the network topology from the tracking system. It then searches the updated network graph using Dijkstra's algorithm [36]. An example of an intermediate node updating a route is shown in Figure 3.

If a route cannot be found for a message, the resulting behavior depends on the message type. A user-data message remains in the queue, and route discovery begins to find a route to the destination. A route-request or a route-reply message with no route is silently discarded to prevent stale information from propagating through the network.

**4.4. Receive Algorithm.** The first step in processing a received message is to extract any topological information and use it to update the link cache. The link cache processes the data and updates the route-advice table as needed. The implicit data from the detection of the transmission is handled separately and is passed directly to the tracking system.

The next step is to discard overheard messages. Though a valuable source of topology data, nontopology-related message contents must not otherwise be processed or forwarded.

The remaining messages are those intended for the local node, either as an intermediate or as the destination. All of these messages update the acknowledgment-equivalence table to ensure they will be acknowledged properly. A message whose destination is the local node is handled and discarded. User data are passed up to the next-highest layer in the stack. Protocol data are processed, which may include originating a route-reply message in response to a route-request message. Other messages intended for the local node, but not destined there, are to be forwarded. These messages are passed to the pending buffer to be enqueued for transmission.

## 5. New Protocol Results

This section discusses the simulation results for the new LASR protocol for underwater acoustic networks. The new protocol has been tested under a variety of simulated underwater missions, each in several operational scenarios. For comparison purposes, these tests are also conducted with the flooding and DSR protocols. The results demonstrate that the LASR protocol provides improved network communication performance compared to flooding and DSR.

DSR is run without any of its optional features enabled as initial work demonstrated that each of the optional

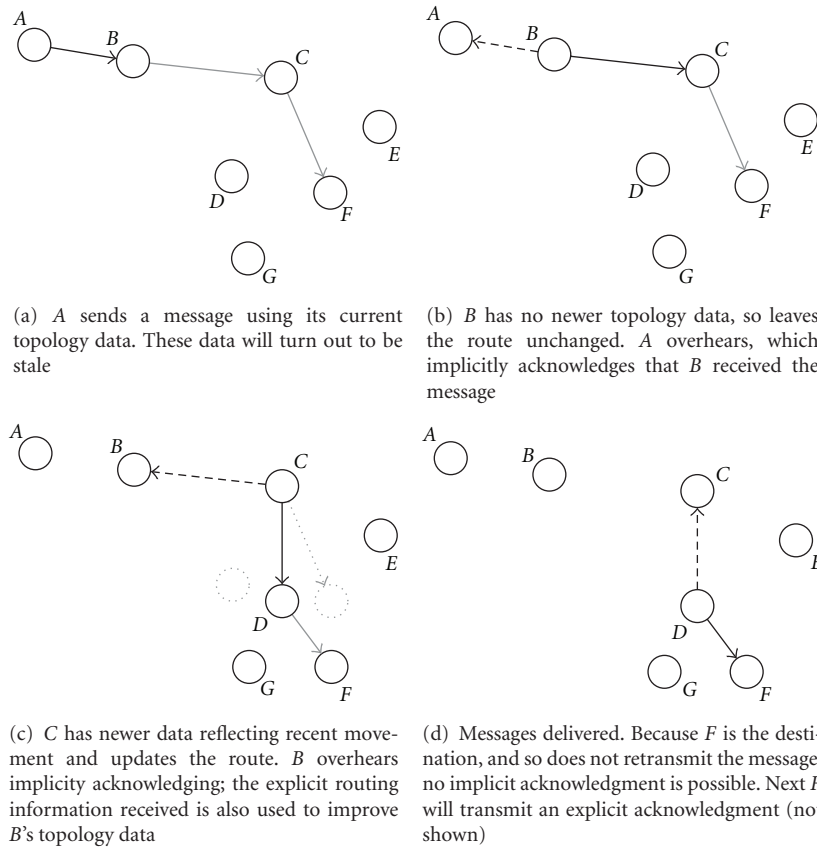


FIGURE 3: An example of LASR's route handling, where an inaccurate route is automatically corrected. For clarity, only the overheard message at the previous transmitter is shown. In actuality, some or all of the other nodes would detect or overhear each transmission, improving the topology data in those other nodes.

features negatively impacted DSR performance in an acoustic network. Three configurations of the LASR protocol are tested, which differ in number of retries and time spent waiting for acknowledgment. The LASR acknowledgment guarantee means that a receiver will acknowledge receipt within the specified time; this controls how much delay is introduced when a message, or its acknowledgment, fails to cross a link. The acknowledgment period is a multiple of the TDMA frame duration, to give each possible receiver some number of opportunities to transmit an acknowledgment (either implicit or explicit). The three LASR configurations are as follows.

- LASR-0+3: no retries, unacknowledged messages are never retransmitted. However, receivers are still obligated to send an acknowledgment within three TDMA frames.
- LASR-2+3: two retries, acknowledgment required within three TDMA frames.
- LASR-2+6: two retries, acknowledgment required within six TDMA frames.

**5.1. Scenarios.** Every scenario uses 16 vehicles, which is selected as an average network size for LASR. The parameters are exhaustively combined, with each combination defining

a scene. Each scenario contains all scenes. Due to the stochastic nature of the communication model, each scene is run 20 times and the results averaged to smooth the performance results. The authors limit the study to 20 runs per scene due to computation time. This paper shows only a small fraction of the extensive simulation results; full results are available in [33].

The vehicles originate messages containing arbitrary data and send the messages to randomly chosen destinations. Every node transmits at every opportunity. If no message is ready to be sent when the node's transmission time-slot opened, a new message is generated by either the application layer or a protocol layer. Here, we assume that there is always at least one packet in the buffer of each transmitting node, with the objective to discover the maximum possible throughput (in practice, the LASR performance is also related to the mean packet generation rate). The random selection of the destination node is according to a uniform distribution: each node (except the originating node itself) has an equal probability of being selected as the destination. This means the network had full utilization at all times: there is never a TDMA time-slot that passes without a transmission, either to forward a protocol or user-data message or to originate a new user-data message.

Each vehicle is equipped with an FAU dual-purpose acoustic modem (DPAM). Every modem uses Frequency-Hopped, M-ary Frequency Shift Keying (FH-MFSK) modulation with convolutional coding [31]. Packets are fixed-size, carrying 32 source bytes each. Each transmission takes 2.65 s and has a guard time of 2.35 s, for a total TDMA time-slot duration of 5 s.

The FER is determined at run-time using the FAU DPAM medium model [32], a stochastic model derived from the Nakagami model, which considers channel geometry, fading characteristics, background noise, bottom type, modulation, and error coding. The network simulation tool was developed at FAU and is described in detail in [32, 33]. The best-case conditions for communication are when Nakagami- $m$  is 2.0 and noise PSD is 55 dB/ $\sqrt{\text{Hz}}$ , the worst-case when Nakagami- $m$  is 1.5 and noise PSD is 65 dB/ $\sqrt{\text{Hz}}$ .

**5.2. Graph Methodology.** There are two graphed network metrics: messages-delivered versus range and message success ratio. These metrics measure different aspects of the network performance: messages-delivered measures throughput, success ratio measures reliability. Note that every message size is fixed to 32 bytes, so that the message-based analysis can be easily converted to a byte-based analysis. The graphs count as delivered or successful only unique user-data messages that reach the intended destination. User-data messages which never reached their destination, duplicate user-data messages received at the destination and protocol-only messages are not counted as delivered or successful. The uncounted messages are the protocol's message overhead.

The messages-delivered graphs show the total number of originated user-data messages that are successfully delivered versus the distance between the originating node and the delivery node at the time of message origination. It does not consider protocol messages (e.g., route requests and route replies) and counts only messages containing user data. The successful delivery of a protocol message is not counted towards messages-delivered, so in general, the greater a protocol's message overhead, the lower its messages-delivered count. These graphs provide a measure of throughput versus range. The messages-delivered graphs should be consulted if throughput is of primary importance, especially if the loss of packets can be tolerated.

The delivery success ratio graphs show the ratio of user-data messages successfully delivered to user-data messages originated. Again, only user-data messages are considered. This ratio is graphed versus the same distances as the messages-delivered graphs. Messages still in the network when the simulation ends are considered lost, and so reduce the success ratio. This metric provides a measure of reliability versus range, that is, the probability that a user-data message sent over a given range will eventually be delivered. The success ratio graphs should be consulted if assured delivery is of primary importance, especially if a loss of throughput can be tolerated.

Note that it is not valid to assume that delivering a greater volume of messages implies that messages are also delivered with greater reliability, or vice versa. They are

commonly *inversely* related because increasing the delivery reliability generally requires increasing protocol overhead, which reduces the total number of messages that can be delivered for a given network bandwidth. A protocol with little overhead may be able to send a tremendous number of user-data messages, losing most but still delivering a large number. On the other hand, a protocol with large overhead may be able to send only a few user-data messages, but may deliver almost all of them.

These metrics both count messages, not bytes. Larger packets would likely increase byte throughput but are also likely slightly decrease both messages-delivered and message success ratio because larger packets would take longer to transmit, thus lengthening the TDMA window, and would probably increase the FER of the links.

**5.3. 16-Vehicle Line.** The line scenario simulates a variety of possible real-life missions where the vehicles are arranged in a line, possibly with active station-keeping. The 16-vehicle line-scenario results are shown in Figures 4 and 5. The data in each figure are obtained using a specific average FER measured between any two adjacent nodes (noted  $FER_{NN}$ ). The distance between neighboring nodes is fixed to provide a specific  $FER_{NN}$  for each scenario, these  $FER_{NN}$  values are 0.01 and 0.40. Under best-case communication conditions,  $FER_{NN} = 0.01$  is achieved when neighbors are separated by 1875 m and  $FER_{NN} = 0.4$  when separated by 3012 m. Under worst-case communication conditions,  $FER_{NN} = 0.01$  is achieved when neighbors are separated by 492 m and  $FER_{NN} = 0.4$  when separated by 1315 m.

LASR proves superior in total number of messages delivered, though not by a substantial margin except for  $FER_{NN} = 0.01$  under the worst-case conditions, shown in Figure 4(c).

Generally, flooding in the line configuration benefits under poor communication conditions because the destination node, which does not retransmit, is often able to halt propagation of a message down the line in one direction. In contrast, flooding actually suffers under good communication conditions. Virtually every originated message reaches every node, as evidenced by its excellent delivery success ratio shown in Figure 4(c). However this also means that every node rebroadcast almost every message, producing message overhead that leaves the network so busy that very few messages can be originated, as shown by the small number of messages delivered shown in Figure 4(c).

Delivered message counts from DSR are consistently bad across the line scenarios due to poor handling of link failure in the high-latency acoustic network. The loss of a message forces route-error propagation in a congested network, which triggers numerous route-request/route-reply cycles, greatly increasing protocol packet overhead.

Three of the protocols do not retry unacknowledged transmissions: flooding which does not support retries, DSR which is found to perform spectacularly poorly when retries are enabled and so is used with retries disabled, and LASR configuration LASR-0+3. Delivery success for the 0.40 case is shown in Figures 5(a) and 5(c). This

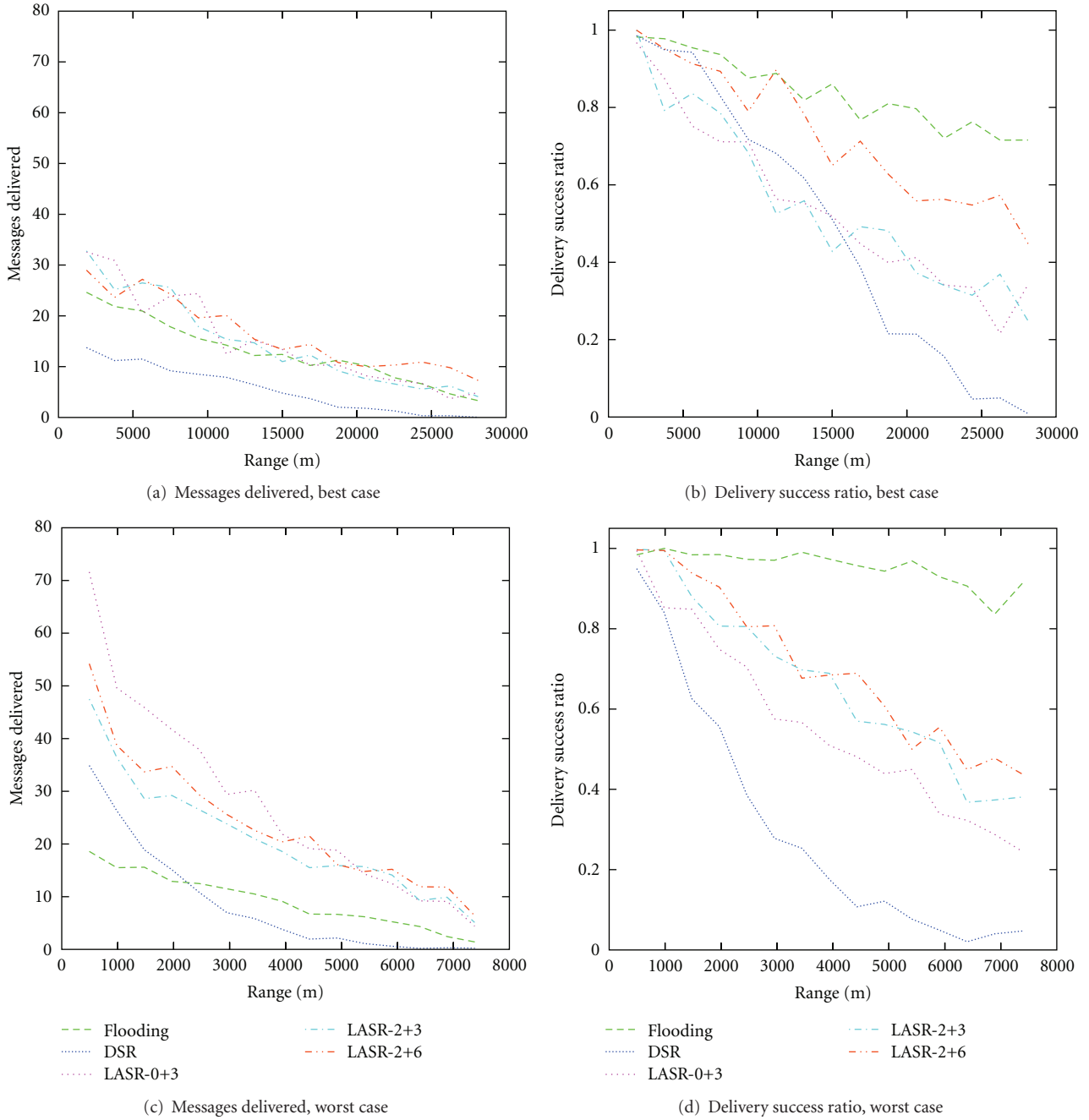


FIGURE 4: Messages delivered and message success: 16-vehicle line,  $FER_{NN} = 0.01$ .

shows that the paths used by each have very similar loss patterns: under any protocol, a message has a roughly equal probability of crossing a given distance in the network. This is as expected—in the 0.40 configuration of the line scenario, there is effectively only one path between any two nodes.

The LASR-2+3 and LASR-2+6 configurations do support retries. These two have similar delivery success across the scenario configurations, degrading only slightly as the communication conditions worsens. Using retries trades network latency and message origination rate for delivery success.

As communication becomes more difficult, the retrying LASR configurations suffer a greater decrease in number of delivered messages over short ranges where the nonretrying protocols profit from their greater origination rate. At the same time, retries become increasingly important to successful delivery over longer ranges, where the retrying protocols consistently maintain greater delivery success. Waiting longer for a retry (LASR-2+6 waiting six frames versus LASR-2+3 waiting three) also improves performance slightly as it requires fewer explicit acknowledgments, reducing protocol packet overhead.

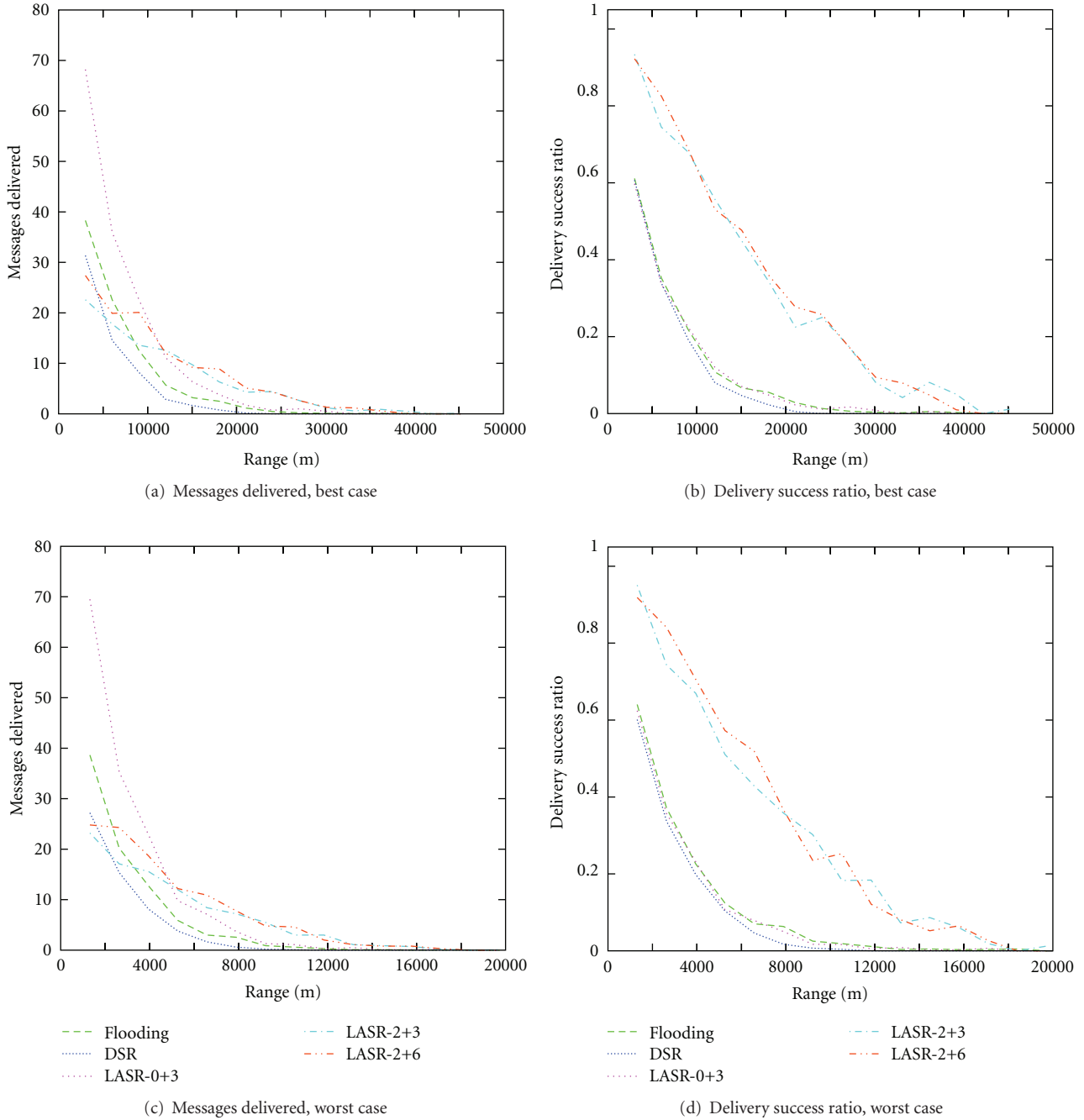


FIGURE 5: Messages delivered and message success: 16-vehicle line,  $FER_{NN} = 0.40$ .

**5.4. 16-Vehicle Spiral.** The spiral mission is a simulation of a search (or survey) mission in shallow waters. Each vehicle follows its own spiral path out from the center. On reaching a predetermined distance from the center, each vehicle follows another spiral back to the center. All vehicles begin and end the mission at the central launch point, and all vehicles remain at the same fixed depth throughout the mission. The spiral paths are calculated to maintain a fixed distance between any two paths, for example, to simulate complete coverage while bottom-mapping with side-scan sonar. All vehicles move at 1.5 m/s.

The  $FER_{NN}$  increases constantly as the vehicles spiral outwards from the central point, reaching a maximum at the turn-back radius, then decreases constantly as the vehicles spiral back to the center. The maximum  $FER_{NN}$  is noted as  $FER_{NN,max}$ . The spiral scenarios are identified by  $FER_{NN,max}$ , rather than by turn-back radius.

The message-success graphs for the spiral are averaged at 500-meter increments. This represents a change from the earlier graphs—nodes in the line and the grid topologies are stationary, remaining at a small number of fixed distances. The movement of the nodes in the spiral mission means

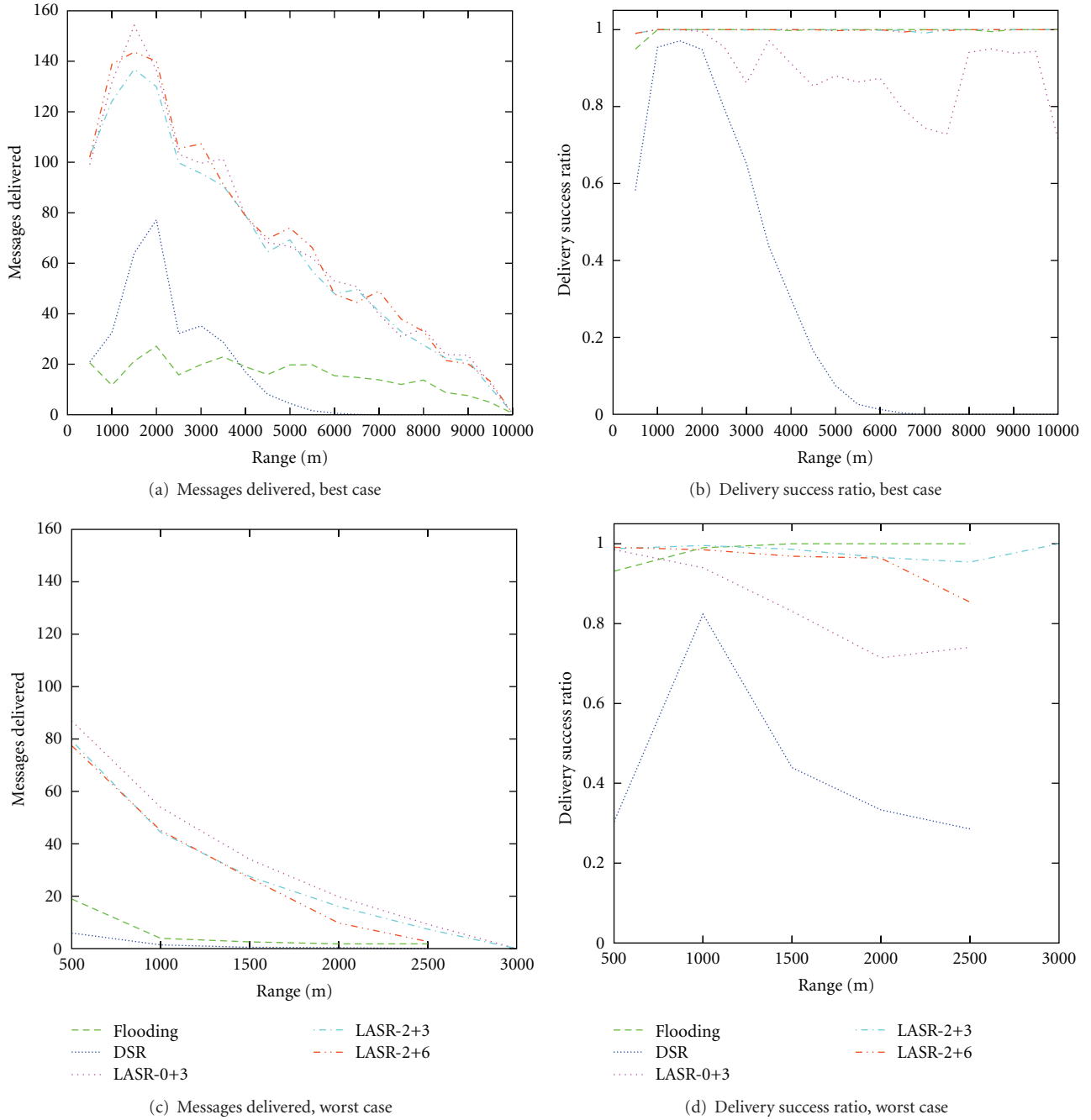


FIGURE 6: Messages delivered and message success: 16-vehicle spiral,  $FER_{N,max} = 0.01$ .

that source-destination distance at message origination is constantly changing. The 16-vehicle spiral results are shown in Figures 6 and 7.

The large peaks in the message-delivery graphs are caused by the motion of the nodes. As the nodes moved, there are certain ranges which occur more frequently than others. For example, as the spiral expands, a given range is encountered first in a link directly across the spiral, then to successively closer vehicles until reaching the neighboring node. This process is repeated as the vehicles return to the launch point. The shortest ranges are passed quickly while the longer

ranges do not occur until late in the spiral, and then suffer from the problems of increased path length and greater message loss. Medium ranges show pronounced peaks in the message-delivery graphs. Those ranges are present for a longer period of time than the shorter ranges. They also have lower network latency and smaller probability of message loss due to shorter paths than the longer ranges do.

At the beginning of the mission, all of the vehicles are very close together and the network is fully-connected: every vehicle can communicate directly with every other vehicle. DSR route discovery learns this topology and routes each

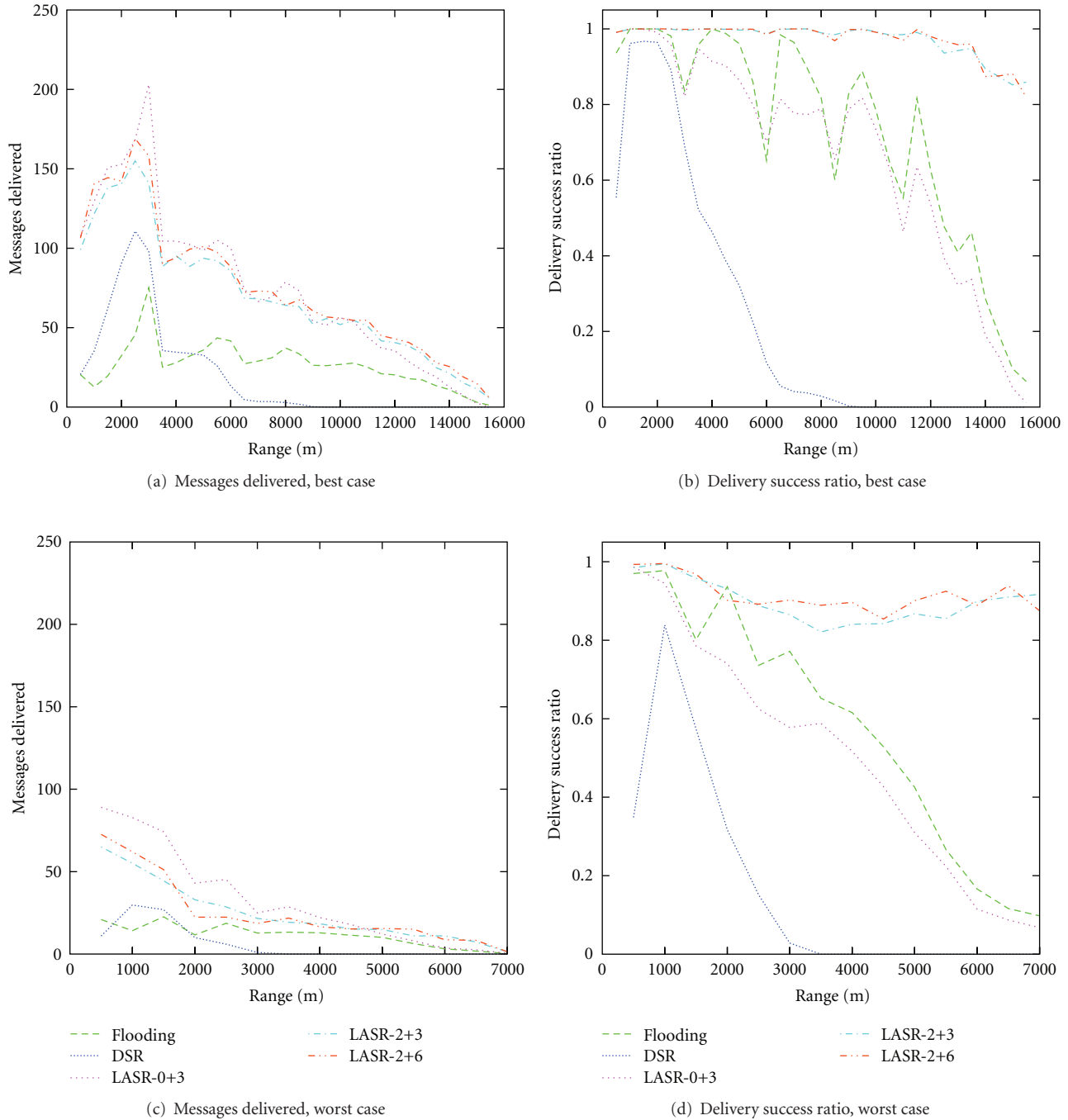


FIGURE 7: Messages delivered and message success: 16-vehicle spiral,  $FER_{NN,max} = 0.40$ .

message directly to its destination. During the expansion period of the mission, the longer links become untenable as the FER sharply increases and DSR begins to lose the messages sent across those links. The lost messages are never acknowledged, so DSR route maintenance marks the links as broken; any subsequent communication between distant links requires multiple hops. Since DSR must wait for an acknowledgment before it gives up on a link, the multiple hops introduce a delay between the actual failure of the link and the removal of the link from the vehicles' link caches.

This delay is responsible for the poor performance of DSR over mid- and long-ranges.

LASR is able to learn the initial, fully-connected network topology within the first TDMA frame. As the vehicles begin to spread out, LASR is able to consistently predict good network routes. The tracking system is kept updated by the constant distribution of network topology information in message source routes and by the regular estimation of node location by detected incoming packet headers. Unlike DSR, LASR does not suffer a lag in its topology information.

Flooding suffers a reverse problem as compared with DSR. When vehicles are close, many receive each transmission, causing the network to become saturated with messages that need to be forwarded. This means that when many reliable links are available, many fewer new messages can be originated, thus there are fewer messages that can be delivered. When vehicles are distant, flooding becomes more efficient. Message loss and a variation on the destination-blocking effect seen in the line scenarios help reduce the number of nodes that have to needlessly forward a message. This explains why flooding maintains largely consistent message delivery counts over all ranges.

*5.5. LASR Benefits and Limitations.* LASR provides an overall improvement in message delivery volume and reliability. Its tracking system gives it the ability to predict network topology with sufficient accuracy for effective routing. The use of the ETX metric means that LASR consistently selects good routes. The acknowledgment guarantee means that LASR can react quickly when transmission fails. In mobile networks, the guarantee also helps ensure that LASR completes link-level acknowledgment quickly, before network topology can change so dramatically that acknowledgment become impossible. The most significant drawback to the LASR protocol is its large header-overhead, which reduces the amount of data that can be contained in a given message. However, LASR have a relatively small message-overhead (most messages are user-data messages rather than protocol messages). Message overhead is a greater hindrance to message delivery in the simulated networks. The simulations demonstrate that LASR provides a better balance between message reliability and message delivery volume than either flooding or DSR.

*5.6. LASR Performance Summary.* In the context of the results presented in this paper, LASR delivers up to 2-3 times as many messages as flooding in 50% of the simulated missions, and delivers up to 2-4 times as many messages as DSR in 100% of the missions. In 50% of the missions with marginal communication conditions, LASR delivers messages requiring multiple hops to cross the network with up to 2-5 times greater reliability than flooding or DSR.

The results presented in this paper cover only a portion of the scenarios tested. A complete description of the tests is given in [33]. The full set of scenarios comprises exhaustive combinations of

- (i) line, grid, or spiral network configurations,
- (ii) 9 or 16 vehicles,
- (iii)  $FER_{NN}/FER_{NN,max}$  of 0.01, 0.20, or 0.40, and
- (iv) best- or worst-case environmental conditions.

Over the full set of simulations, LASR delivers 2-3 times as many messages as flooding in 72% of the simulated missions, and delivers 2-4 times as many messages as DSR in 100% of the missions. In 67% of the missions with fair or marginal communication conditions, LASR delivers messages requiring multiple hops to cross the network with 2-5 times greater reliability than flooding or DSR.

## 6. Conclusion

The new location-aware source routing (LASR) is a reactive, link-state MANET routing protocol specifically designed to the constraints of an underwater acoustic network. It was intended for small underwater networks using low-bandwidth, high-latency acoustic links. Nodes were assumed to be mobile, moving at any time (including continuously) and in any direction with node speeds in the range of 0-3 m/s. LASR used the implicit information drawn from incoming transmissions to estimate ranges to neighboring nodes; these ranges were continuously fed into a tracking system which estimated local network topology. Other improvements included the addition of the ETX route metric to replace minimum hop-count, the use of an acknowledgment guarantee and aggressive, preemptive rerouting.

Simulated missions showed that the flooding protocol and DSR performed poorly in an underwater acoustic network. The flooding protocol provided reliable delivery at the cost of decreased message delivery counts. The DSR protocol regularly delivered the fewest messages with the least reliability.

The simulations showed the new LASR protocol to be superior to the DSR and blind-flooding routing protocols. In many of the simulated missions, LASR delivered more messages than flooding. In all of the simulated missions, LASR delivered more messages than DSR. Under fair or marginal communication conditions, LASR delivered messages requiring multiple hops to cross the network with greater reliability than flooding or DSR in more than half of the missions.

## Appendices

### A. Protocol Messages

A user-data message comprises: user data, source network address, destination network address, a source-assigned ID, and a route.

A route-request message comprises a source network address, destination network address, a source-assigned ID, and a route. It is flooded through the network and the route is built as the message travels.

A route-reply message comprises a source network address, destination network address, a source-assigned ID, and a route. It is sent in response to a route request and is routed to the originator of the request.

A route-advice message comprises topology data on one link. It is never forwarded.

An explicit-acknowledgment message comprises a source network address, a destination network address, and an identifying message-originator network address/message-ID pair. It is sent only when implicit acknowledgment is not possible.

### B. Link Metric

LASR does not store the ETX, instead it stores the range and calculates the ETX as it is needed. This means the link quality

```

(1) for each msg in data-queue do
(2)   if IS-PENDING-TIME-EXPIRED(msg) then
(3)     ▷The message has been waiting too long for a route. It cannot be delivered.
(4)     DELETE-MESSAGE(msg)
(5)   else
(6)     if STATE(msg) = WAITING-FOR-ACK
(7)       and IS-ACK-TIME-EXPIRED(msg) then
(8)         STATE(msg) ← PENDING
(9)       end if
(10)      if STATE(msg) = PENDING then
(11)        route ← ROUTE-SEARCH (ORIG(msg), DEST(msg))
(12)        if route = ∅ then
(13)          ▷Enqueue a route-request message if one isn't already outstanding according to
(14)          the route-request table.
(15)          ROUTE-REQ-MAYBE (DEST(msg))
(16)        else
(17)          ▷Stop searching and return this message for transmission.
(18)          STATE(msg) ← WAITING-FOR-ACK
(19)          return msg
(20)        end if
(21)      end if
(22)    end if
(23)  end for
(24)  ▷There are no data messages to transmit at this time
(25)  return NO-MSG

```

ALGORITHM 1: The algorithm for obtaining the next user-data message from the data queue.

fields contain the distance in meters between the endpoints of the link, as estimated at the time of the timestamp.

In order to reduce the size of the protocol header, distances are stored as a 4 bit value to represent distances from 0–4080 meters in increments of 256 m. Link distance estimates are capped at 4080 m, the maximum range of the simulated acoustic modem (DPAM) [32]. An additional bit is used to flag the distance as estimated (by a time-of-flight measurement) or predicted (by the tracking system).

The timestamp communicates the age of the link data to ensure that only the newest link data are used and that stale link data are discarded. The timestamp represents the absolute age of the associated link data as a number of seconds before the start of the time window in which they are transmitted. On reception, timestamps are converted back to absolute times. Link data are considered fresh if 0–1019 seconds old, aging if 1020–2039 s old and stale if 2040 s or older. Fresh and aging link data are added to the receiver's link cache if no newer version already exists. If a newer version does exist, the link's advise priority is increased in the route-advice table. Link data are discarded if they become stale while in the cache.

### C. Data Structures

The pending buffer contains all of the messages awaiting transmission: a data queue stores the outgoing user-data messages, a protocol queue stores all the protocol messages. Two data-queue messages are sent for every protocol-queue message sent.

User-data messages in the data queue exist in one of two states: pending or waiting for acknowledgment. A pending message is ready for transmission once one or more routes to the destination become available. The best route is systematically used.

Every transmitted message must be acknowledged. The message returns to pending status if the acknowledgment times out.

An unsent message in the queue will eventually expire and be removed. The algorithm for selecting the next message to transmit from the data queue is shown in Algorithm 1.

The protocol queue stores route requests and route replies. A pending route-request message or a route-reply message which does not have a route is silently discarded. If a protocol message is not acknowledged within the acknowledgment timeout, its state reverts to pending. The algorithm for selecting the next message to transmit (if any) from the protocol queue is shown in Algorithm 2.

- (1) Link Cache: The link cache stores all of the information currently available about the topology of the network. Information is added or updated whenever topology data become available and is removed when data become stale. When a route between two network nodes is needed, the first step is to search these topology data. The link cache communicates with the tracking system to receive predicted topology information that is used to supplement the cached information.

```

(1) for each msg in protocol-queue do
(2)   if STATE(msg) = WAITING-FOR-ACK
      and IS-ACK-TIME-EXPIRED(msg) then
(3)     STATE(msg) ← PENDING
(4)   end if
(5)   if STATE(msg) = PENDING then
(6)     if MSG-TYPE(msg) = ROUTE-REQUEST then
      ▷Route request message contain a route ending at the local node.
(7)       dest ← local-node
(8)     else
      ▷Route reply message contain a route ending at the message's destination.
(9)       dest ← DEST(msg)
(10)    end if
      ▷Both message type contain a route starting at message's originator.
(11)    route ← ROUTE-SEARCH (ORIG(msg), dest)
(12)    if route = ∅ then
      ▷A protocol message without a route is deleted.
(13)      DELETE-MESSAGE(msg)
(14)    else
      ▷Stop searching and return this message for transmission
(15)      STATE(msg) ← WAITING-FOR-ACK
(16)      return msg
(17)    end if
(18)  end if
(19) end for
      ▷There are no protocol messages to transmit at this time.
(20) return NO-MSG

```

ALGORITHM 2: The algorithm for obtaining the next user-data message from the data queue.

The cache is organized as a link cache: it stores data on the links between pairs of nodes. This organization allows route searches across all known and predicted topology data, potentially returning completely novel routes. Searching for routes is done with Dijkstra's algorithm [36], using weights calculated according to the link metric. Before searching for a route, the tracking system returns all predicted links and these are merged with the cached links into a temporary link table using a modified merge sort. When both the tracking system and the cache provide information about the same link, one of the two is chosen. If the link cache is unable to find a route between the requested nodes, a route request must be sent to obtain the link data necessary to build the route. A simplified version of the link data merge algorithm is shown in Algorithm 3.

The cache stores several pieces of data for each known link: endpoints, range, origin, and age. The link endpoints are the network addresses of the nodes at either end of the link. The link range is the distance between the endpoints. Origin is a flag indicating whether the distance was estimated (by a time-of-flight measurement) or predicted (by the tracking system). The link age is the time the distance was obtained: the time of the time-of-flight measurement for estimated distances or the time from the tracking system for a predicted distance. Currently, the tracking system reports the age of a prediction as the time of the most recent update to the data underlying that prediction. To prevent the use of stale data, the cache monitors age and automatically purges expired data.

Two types of data are used to update the link cache: explicit and implicit. The explicit data are extracted from received and overheard messages, including source routes, route requests, route replies, and route advice. The data include link endpoints, link range, and range age. Implicit data are recovered from received transmissions, but are not a part of the transmission data. When a transmission is received, the receiver is able to identify the transmitting node and estimate the range to that node using only on the medium model, the current time, and knowledge of the current TDMA time-slot. This provides data on the link between the receiving node and the transmitting node. These data are also used to update the tracking system.

The route-discovery table stores information about outstanding route-request messages. When a route request is originated to a given destination, an entry is added to the route-discovery table. This entry records the destination and the time the route-request message was sent. Further route requests for that destination will not be sent for as long as the entry remains in the table. This provides a delay between route requests to the same destination, allowing time for a route request to cross the network to the destination and for a route reply to return to the originator.

An entry is removed from the route-discovery table in one of two cases:

- (1) a route-reply message is received from that destination.

```

    ▷Links are sorted into ascending order of the node IDs of their endpoints.
(1)  $P \leftarrow \text{SORT-PREDICTED-LINKS}()$ 
(2)  $C \leftarrow \text{SORT-CACHED-LINKS}()$ 
    ▷Initialize the temporary merged link table.
(3)  $M \leftarrow \emptyset$ 
    ▷POP removes and returns the head element.
(4)  $p \leftarrow \text{POP}(P)$ 
(5)  $c \leftarrow \text{POP}(C)$ 
    ▷Loop until both link tables are empty.
(6) while  $p = \emptyset$  or  $c = \emptyset$ 
(7)   if  $p = c$  then
        ▷They represent the same link. Choose one based on origin and age.
(8)      $M \leftarrow \text{CHOOSE-LINK}(p, c)$ 
(9)      $p \leftarrow \text{POP}(P)$ 
(10)     $c \leftarrow \text{POP}(C)$ 
(11)   else if  $p < c$  then
(12)      $M \leftarrow p$ 
(13)      $p \leftarrow \text{POP}(P)$ 
(14)   else
(15)      $M \leftarrow c$ 
(16)      $c \leftarrow \text{POP}(C)$ 
(17)   end if
(18) end while

```

ALGORITHM 3: A simplified version of the algorithm used to merge the link data from the link cache and the tracking system. At the conclusion of the merge,  $M$  contains the merged link table.

```

    ▷Look for an earlier reply to route request  $req$ .
(1)  $prior\_route \leftarrow \text{LOOKUP-REPLY-ROUTE}(req)$ 
    ▷Get the best route from the local node to the originator of the route request.
(2)  $new\_route \leftarrow \text{ROUTE}(local\_node, \text{ORIG}(req))$ 
(3) if  $prior\_route = \emptyset$ 
        or  $\text{ETX}(new\_route) < \text{ETX}(prior\_route)$  then
        ▷No reply has ever been sent or a better route is now available.
(4)    $\text{UPDATED-REPLY-TABLE}(req, new\_route)$ 
(5)    $\text{ENQUEUE-ROUTE-REPLY}(\text{ORIG}(req))$ 
(6) end if

```

ALGORITHM 4: The route-reply algorithm.

- (2) the route-request message times out. Another route-request message may be sent after the timeout if the route is still needed.

The route-reply table stores information about outstanding route-reply messages. Each route request is uniquely identifiable in the network, but multiple copies of the same route request may be received by the destination. An entry in the route-reply table contains the unique ID of a given route request, the route sent in reply and the time the route request was first received.

If a route-request message is received with the local node as the destination, the node checks its route-reply table. If no entry exists for the unique ID of the route request, a route-reply message is returned to the request's originator. If an entry does exist, the best-available route is compared to the route stored in the entry. If the best-available route is better than the stored route, a new route reply is originated

containing the new route and the stored route is updated. When an entry expires, it is removed from the table. The route-reply algorithm is shown in Algorithm 4.

The route-request table ensures a node processes a given route-request message only once, regardless of the number of times it is received. When a route-request message is received it will be enqueued for resending if there is no corresponding entry in the route-request table. An entry containing that route request's unique ID and the time is then added to the table. If a route request is received and there is a corresponding entry in the table, the request is dropped. The time is used to determine the expiration of the entry, which depends on the size of the route request circular ID used by the network. An entry is removed from the table when it expires.

The route-advice table serves to prioritize the sending of route-advice messages. When topology data are received,

either implicitly or explicitly, they are processed by the link cache. If the received data are older than the data in the cache, the route-advice table is updated. The table stores link data along with a priority value; the priority is updated based on the age of the received data. When the opportunity arises to send a route-advice message, the message data are selected randomly from the route-advice table using the priority as a weight. The priorities ensure that it is more likely for older and more commonly used data to be advised first. Advice data selected for transmission are removed from the table.

## References

- [1] J. J.-N. Liu and I. Chlamtac, "Mobile Ad Hoc networking with a view of 4G wireless: Imperatives and challenges," in *Mobile Ad Hoc Networking*, S. Basagni, M. Conti, S. Giordano, and I. Stojmenovic, Eds., chapter 1, pp. 1–45, Wiley-Interscience, 2004.
- [2] J. P. Macker and M. S. Corson, "Mobile Ad Hoc networks (MANETs): routing technology for dynamic wireless networking," in *Mobile Ad Hoc Networking*, S. Basagni, M. Conti, S. Giordano, and I. Stojmenovic, Eds., chapter 9, pp. 255–273, Wiley-Interscience, 2004.
- [3] R. Rajaraman, "Topology control and routing in Ad Hoc networks: a survey," *SIGACT News*, vol. 33, no. 2, pp. 60–73, 2002.
- [4] S. Basagni, M. Conti, S. Giordano, and I. Stojmenovic, Eds., *Ad Hoc Networking*, Wiley-Interscience, 2004.
- [5] C. Perkins and P. Bhagwat, "Highly dynamic destination-sequenced distance-vector routing (DSDV) for mobile computers," in *Proceedings of the Conference on Communications Architectures, Protocols and Applications (SIGCOMM '94)*, pp. 234–244, ACM Press, New York, NY, USA, 1994.
- [6] E. M. Belding-Royer and C. E. Perkins, "Evolution and future directions of the Ad Hoc on-demand distance-vector routing protocol," *Ad Hoc Networks*, vol. 1, no. 1, pp. 125–150, 2003.
- [7] R. Ogier, F. Templin, and M. Lewis, "Topology dissemination based on reverse-path forwarding (TBRPF)," RFC 3684, IETF MANET Working Group, February 2004.
- [8] V. D. Park and M. S. Corson, "Highly adaptive distributed routing algorithm for mobile wireless networks," in *Proceedings of the 16th IEEE Annual Conference on Computer Communications (INFOCOM '97)*, pp. 1405–1413, April 1997.
- [9] D. B. Johnson, D. A. Maltz, and Y.-C. Hu, "The dynamic source routing protocol for mobile Ad Hoc networks (DSR)," INTERNET-DRAFT, IETF MANET Working Group, July 2004.
- [10] E. M. Sozer, M. Stojanovic, and J. G. Proakis, "Underwater acoustic networks," *IEEE Journal of Oceanic Engineering*, vol. 25, no. 1, pp. 72–83, 2000.
- [11] H. Ju, I. Rubin, K. Ni, and C. Wu, "A distributed mobile backbone formation algorithm for wireless Ad Hoc networks," in *Proceedings of the 1st International Conference on Broadband Networks (BroadNets '04)*, pp. 661–670, October 2004.
- [12] M. K. Marina and S. R. Das, "Performance of route caching strategies in dynamic source routing," in *Proceedings of the International Conference on Distributed Computing Systems Workshop*, pp. 425–432, 2001.
- [13] B. C. Seet, B. S. Lee, and C. T. Lau, "Optimisation of route discovery for dynamic source routing in mobile Ad Hoc networks," *Electronics Letters*, vol. 39, no. 22, pp. 1606–1607, 2003.
- [14] F. Bai, N. Sadagopan, B. Krishnamachari, and A. Helmy, "Modeling path duration distributions in MANETs and their impact on reactive routing protocols," *IEEE Journal on Selected Areas in Communications*, vol. 22, no. 7, pp. 1357–1373, 2004.
- [15] S. R. Medidi and K. H. Vik, "Quality of service-aware source-initiated Ad Hoc routing," in *Proceedings of the 1st Annual IEEE Communications Society Conference on Sensor and Ad Hoc Communications and Networks (IEEE SECON '04)*, pp. 108–117, October 2004.
- [16] C.-H. Chuan and S.-Y. Kuo, "Cache management of dynamic source routing for fault tolerance in mobile Ad Hoc networks," in *Proceedings of the Pacific Rim International Symposium on Dependable Computing*, pp. 199–205, 2001.
- [17] W. P. Chen and J. C. Hou, "Dynamic, Ad Hoc source routing with connection-aware link-state exchange and differentiation," in *Proceedings of the IEEE Global Telecommunications Conference (GLOBECOM '02)*, vol. 1, pp. 188–194, November 2002.
- [18] J. R. Potter, A. Berni, J. Alves, D. Merani, G. Zappa, and R. Been, "Underwater communications protocols and architecture developments at NURC," in *Proceedings of the OCEAN*, pp. 1–6, Santander, Spain, 2011.
- [19] J. Ahn, A. Syed, B. Krishnamachari, and J. Heidemann, "Design and analysis of a propagation delay tolerant ALOHA protocol for underwater networks," *Ad Hoc Networks*, vol. 9, no. 5, pp. 752–766, 2011.
- [20] M. S. Rahim, P. Casari, F. Guerra, and M. Zorzi, "On the performance of delay-tolerant routing protocols in underwater networks," in *Proceedings of the OCEAN*, pp. 1–7, Santander, Spain, 2011.
- [21] A. Patil and M. Stojanovic, "A node discovery protocol for Ad Hoc underwater acoustic networks," in *Proceedings of the OCEAN*, pp. 1–9, Spain, June 2011.
- [22] M. Chitre, S. Shahabudeen, and M. Stojanovic, "Underwater acoustic communications and networking: recent advances and future challenges," *Marine Technology Society Journal*, vol. 42, no. 1, pp. 103–116, 2008.
- [23] J. Heidemann, W. Ye, J. Wills, A. Syed, and Y. Li, "Research challenges and applications for underwater sensor networking," in *Proceedings of the IEEE Wireless Communications and Networking Conference (WCNC '06)*, vol. 1, pp. 228–235, April 2006.
- [24] D. Pompili and I. Akyildiz, "Overview of networking protocols for underwater wireless communications," *Communications Magazine, IEEE*, vol. 47, no. 1, pp. 97–102, 2009.
- [25] E. P. C. Jones and P. A. S. Ward, "Routing strategies for delay-tolerant networks," in *ACM Computer Communication Review*, 2006.
- [26] I. Cardei, C. Liu, J. Wu, and Q. Yuan, "DTN routing with probabilistic trajectory prediction," in *Proceedings of the Wireless Algorithms, Systems, and Applications (WASA '08)*, vol. 5258 of *Lecture Notes in Computer Science*, pp. 40–51, 2008.
- [27] M. Stojanovic, L. Freitag, J. Leonard, and P. Newman, "A network protocol for multiple AUV localization," in *Proceedings of the MTS/IEEE Oceans Conference*, vol. 1, pp. 604–611, Biloxi, Miss, USA, October 2002.
- [28] R. Bachmayer, J. A. Rice, R. Crebert, and C. Fletcher, "Navigation and control of multiple gliders in an underwater acoustic network," in *Proceedings of the IEEE/OES Autonomous Underwater Vehicles*, pp. 54–58, June 2004.
- [29] O. Normand, *Synchronous spatial array processing for underwater vehicle tracking [M.S. thesis]*, Florida Atlantic University, 2002.

- [30] E. A. Carlson, P. P. Beaujean, and E. An, "An improved location-aware routing protocol for mobile underwater acoustic networks," in *Proceedings of the MTS/IEEE Oceans Conference*, Vancouver, Canada, October 2007.
- [31] P. P. J. Beaujean and E. P. Bernault, "A new multi-channel spatial diversity technique for long range acoustic communications in shallow water," in *Proceedings of the MTS/IEEE Oceans Conference*, pp. 1533–1538, September 2003.
- [32] E. A. Carlson, P. - Beaujean, and E. An, "An Ad Hoc wireless acoustic network simulator applied to multiple underwater vehicle operations in shallow waters using high-frequency acoustic modems," *U.S. Navy Journal of Underwater Acoustics*, vol. 56, pp. 113–139, 2006.
- [33] E. A. Carlson, *Simulator and location-aware routing protocol for mobile Ad Hoc acoustic networks of AUVs [Ph.D. dissertation]*, Florida Atlantic University, 2009.
- [34] D. S. J. De Couto, D. Aguayo, J. Bicket, and R. Morris, "A high-throughput path metric for multi-hop wireless routing," in *Proceedings of the 9th Annual International Conference on Mobile Computing and Networking (MobiCom '03)*, pp. 134–146, ACM Press, New York, NY, USA, September 2003.
- [35] R. Draves, J. Padhye, and B. Zill, "Comparison of routing metrics for static multi-hop wireless networks," in *Proceedings of the Conference on Computer Communications (ACM SIGCOMM '04)*, pp. 133–144, ACM Press, New York, NY, USA, September 2004.
- [36] E. W. Dijkstra, "A note on two problems in connexion with graphs," *Numerische Mathematik*, vol. 1, no. 1, pp. 269–271, 1959.

## Research Article

# Information-Theoretic Analysis of Underwater Acoustic OFDM Systems in Highly Dispersive Channels

Francois-Xavier Socheleau,<sup>1</sup> Milica Stojanovic,<sup>2</sup>  
Christophe Laot,<sup>3</sup> and Jean-Michel Passerieux<sup>4</sup>

<sup>1</sup>ENSTA Bretagne, UMR CNRS 6285 Lab-STICC, Université Européenne de Bretagne, 2 rue Francois Verny, 29806 Brest Cedex 9, France

<sup>2</sup>Department of Electrical and Computer Engineering, Northeastern University, Boston, MA 02115, USA

<sup>3</sup>Institut Mines-Télécom, Telecom Bretagne, UMR CNRS 6285 Lab-STICC, Université Européenne de Bretagne, Technopôle Brest Iroise-CS 83818, 29238 Brest Cedex, France

<sup>4</sup>General Sonar Studies Group, Thales Underwater Systems, 525 route des Dolines, 06903 Sophia Antipolis Cedex, France

Correspondence should be addressed to Francois-Xavier Socheleau, francois-xavier.socheleau@ensta-bretagne.fr

Received 10 February 2012; Accepted 24 April 2012

Academic Editor: Konstantinos Pelekanakis

Copyright © 2012 Francois-Xavier Socheleau et al. This is an open access article distributed under the Creative Commons Attribution License, which permits unrestricted use, distribution, and reproduction in any medium, provided the original work is properly cited.

This paper investigates the signal-to-interference ratio and the achievable rates of underwater acoustic (UA) OFDM systems over channels where time and frequency dispersion are high enough that (i) neither the transmitter nor the receiver can have a priori knowledge of the channel state information and (ii) intersymbol/intercarrier interference (ISI/ICI) cannot be neglected in the information-theoretic treatment. The goal of this study is to obtain a better understanding of the interplay between interference and the achievable transmission rates. Expressions for these rates take into account the “cross-channels” established by the ISI/ICI and are based on lower bounds on mutual information that assume independent and identically distributed input data symbols. In agreement with recent statistical analyses of experimental shallow-water data, the channel is modeled as a multivariate Rician fading process with a slowly time-varying mean and with potentially correlated scatterers, which is more general than the common wide-sense stationary uncorrelated scattering model. Numerical assessments on real UA channels with spread factors around  $10^{-1}$  show that reliable OFDM transmissions at 2 to 4 bits/sec/Hz are achievable provided an average signal-to-noise ratio of 15 to 20 dB.

## 1. Introduction

The various collections of underwater acoustic (UA) channels surveyed worldwide highlight the diversity of UA propagation environments and confirm in many cases the bad reputation of these channels as communication media [1–4]. UA communication systems are usually prone to time and frequency dispersion due to multipath propagation and Doppler effects, and the absorption of acoustic waves at high frequencies strongly limits their bandwidth. Finding systems that are robust to the environment, while maintaining acceptable data rates, remains the major difficulty faced by UA communication system designers. For a given propagation channel, this interplay between robustness and data rate results in practice in choosing different modulation

schemes according to the importance we give to one or the other characteristic, the optimal trade-off being unknown in most cases. Historically, single-carrier modulations with receivers relying on channel equalizers in the time domain have been widely studied and used in practice for high-speed underwater communications [5]. Recently, multi-carrier (MC) systems such as OFDM (orthogonal frequency division multiplexing) [6–9] have generated much interest due to the simplicity of receivers and the flexibility they offer.

For time-invariant channels, modulation-basis functions of common OFDM signals (e.g., cyclic prefix-based OFDM) can be seen as “eigen” functions of the channel operator and ensure the absence of interference at reception. This way of “diagonalizing” the channel allows the use of simple algorithms for recovering the information from the received

signal. For double-dispersive channels, and particularly in the UA context, perfect channel diagonalization can rarely be achieved as the environment is generally random so that the channel eigenstructure differs from one channel realization to another. The channel diagonalization can then only be performed in some approximate sense [10–12] and interference due to time-frequency dispersion becomes inevitable. However, even if UA-OFDM systems can hardly avoid interference, compared to single-carrier approaches, multiplexing the information to be transmitted on a time-frequency grid offers the opportunity to optimize more degrees of freedom. OFDM system design is classically approached from the viewpoint of intersymbol/intercarrier interference (ISI/ICI) through maximization of the signal-to-interference ratio (SIR) [10, 11, 13–15]. For a given set of channels, finding the MC signaling scheme that maximizes the average SIR is a way of designing robust systems that do not require complex equalization algorithms at reception. While the SIR may be a good figure of merit to assess the robustness of communications in doubly dispersive environments, it does not reveal the effect of the chosen signaling scheme on the information rate. The robustness improvement is generally paid back by the loss of spectral efficiency induced by the use of time and/or frequency guard intervals required to limit the interference. For instance, typical UA-OFDM systems use a guard interval between symbols that is lower-bounded by the maximum delay spread of the channel, which often lasts several tens of milliseconds. Compared to the active symbol duration, this interval is usually not negligible and can significantly reduce the transmission efficiency. Therefore, it remains unclear whether or not OFDM systems should tolerate slightly increased interference but operate at higher data rate.

Motivated by recent results in information theory and UA channel modeling, an information-theoretic analysis of the trade-off between maximization of SIR and minimization of guard intervals is proposed in this paper. More precisely, our main goal is to obtain a better understanding of the interplay between interference and the achievable transmission rate of UA-OFDM systems. We pay special attention to UA channels, where time and frequency dispersions are high enough so that ISI/ICI cannot be neglected in the information-theoretic treatment. Our analysis addresses two questions. First, what are the achievable rates of UA-OFDM in highly dispersive channels? And as a corollary, what are the consequences of OFDM design choices on these rates?

The target of our analysis is the investigation of UA-OFDM information rate. To this end, we believe that the following aspects need to be accounted for:

- (A1) the UA channel is selective both in time and frequency;
- (A2) the UA channel cannot systematically be modeled as a wide-sense stationary uncorrelated scattering (WSSUS) process;
- (A3) no perfect channel state information (CSI) is available at the transmitter nor the receiver;
- (A4) interference is not negligible *a priori*.

These aspects are important as they may have a strong impact on the achievable rates of UA-OFDM systems. (A1) is particularly true in shallow-water environments where the spread factor (product between the delay and Doppler spread) is usually around  $[10^{-3}, 10^{-1}]$  and can even exceed 1 in some cases [1]. The WSSUS assumption discussed in (A2) implies that the channel correlation function is time-invariant and that the scatterers with different path delays are uncorrelated so that the second-order statistics of the channel are reduced from four to two dimensions [16]. While this assumption may be valid for data transmission at low bandwidth with static communication endpoints, it is not the case with moving platforms and/or when the path-loss associated with each channel path cannot be assumed to be constant over the transmission bandwidth [2, 17]. (A3) corresponds to what is commonly referred to as the *noncoherent* setting where neither the transmitter nor the receiver knows the current realization of the channel perfectly [18–20]. This assumption has to be contrasted with the *coherent* setting where a genie provides the receiver with perfect CSI. (We warn the reader that the word *coherent* is here used in an information-theoretic context and its definition slightly differs from the one used in a demodulation context.) For most channels, the coherent model is not realistic since receivers are not genie-aided, and the effort to acquire the CSI usually induces some rate loss (pilots insertion, channel estimation errors, etc.). In addition, assuming perfect CSI at the transmitter is also optimistic for most practical cases since the low propagation speed of acoustic waves imposes strong constraints on the nature of the CSI provided by a feedback link. Since we focus on highly dispersive channels, we consider in (A4) that interference must be explicitly accounted for in the information theoretic-treatment.

To the best of our knowledge, the information rate of OFDM systems under such general assumptions has not yet been derived. However, recent works presented in [17] and more particularly in [21] give some useful ingredients to derive this rate. In [17], the authors derive bounds on the achievable rate of UA-OFDM systems and consider the aspects (A1) and (A3), and (A2) in part. Although correlated scattering is taken into account in their channel model, they assume wide-sense stationarity. As for interference, it is neglected in their analysis. In [21], Durisi et al. explicitly account for interference terms but present their results for WSSUS Rayleigh fading channels, which is not appropriate for the majority of UA channels [2, 22].

The main contributions of this paper are the following:

- (i) based on the UA channel characterization presented in [2], we present an exact analysis of ISI/ICI of UA-OFDM systems transmitting in non-WSSUS channels. The channel is modeled as a multivariate Rician fading process with a slowly time-varying mean and with potentially correlated scatterers;
- (ii) the information rate of UA-OFDM systems is analyzed under the general scenario described by the aspects (A1)–(A4);

- (iii) in order to extract guidelines useful for UA-OFDM system design, theoretical results are then numerically assessed on rectangular pulse shaping OFDM transmitting over experimental UA channels surveyed at sea.

This paper is organized as follows. Section 2 is devoted to the presentation of the system model and the main assumptions. Signal-to-interference ratio and achievable rates of OFDM systems transmitting over UA channels are derived in Section 3. In Section 4, we discuss the impact of channel and OFDM parameters on the information rate through various numerical experiments. Finally, conclusions are given in Section 5.

## 2. System Model

**2.1. Notation.** Throughout this paper, lowercase boldface letters denote vectors, for example,  $\mathbf{x}$ , and uppercase boldface letters denote matrices, for example,  $\mathbf{A}$ . The superscripts  $T$  and  $\dagger$  denote transposition and Hermitian transposition, respectively. The Hadamard (elementwise) products of two matrices  $\mathbf{A}$  and  $\mathbf{B}$  is written as  $\mathbf{A} \odot \mathbf{B}$ . The entries of a matrix  $\mathbf{A}$  are denoted by  $[\mathbf{A}]_{k,n}$ , where the indices  $k$  and  $n$  start at 0.  $\mathbf{B}^{(k,k')}$  designates a submatrix of a block matrix  $\mathbf{B}$ . The Kronecker symbol is denoted by  $\delta(k)$ . We let  $\text{diag}(\mathbf{x})$  designate a diagonal square matrix whose main diagonal contains the elements of the vector  $\mathbf{x}$ . The inner product between two signals  $y(t)$  and  $z(t)$  is denoted by  $\langle y, z \rangle = \int_{-\infty}^{+\infty} y(t)z^*(t)dt$ .  $\mathcal{CN}(\mathbf{m}, \mathbf{R})$  designates the distribution of a jointly proper Gaussian random vector [23] with mean  $\mathbf{m}$  and covariance matrix  $\mathbf{R}$ . Finally,  $\mathbb{E}\{\cdot\}$  denotes expectation.

**2.2. Channel Model.** We consider a doubly selective baseband equivalent underwater acoustic channel, modeled as a random linear time-varying system  $\mathbb{H}$  that maps input signals  $x(t)$  into output signals  $y(t)$  according to the I/O relationship:

$$y(t) = (\mathbb{H}x)(t) + w(t) = \int_{\tau} h_{\mathbb{H}}(\tau, t)x(t - \tau)d\tau + w(t), \quad (1)$$

where  $h_{\mathbb{H}}(\tau, t)$  is the channel impulse response, and  $w(t)$  denotes the ambient noise.

According to recent results on the statistical characterization of UA channels [2], the impulse response is modeled as a *trend stationary* random process so that, for all  $t, t_1$  and  $t_2 \in \mathbb{R}$

$$h_{\mathbb{H}}(\tau, t) = \tilde{h}_{\mathbb{H}}(\tau, t) + \bar{h}_{\mathbb{H}}(\tau, t), \quad (2)$$

with

$$\mathbb{E}\{h_{\mathbb{H}}(\tau, t)\} = \bar{h}_{\mathbb{H}}(\tau, t), \quad (3)$$

$$\begin{aligned} & \mathbb{E}\{(h_{\mathbb{H}}(\tau, t_1) - \mathbb{E}\{h_{\mathbb{H}}(\tau, t_1)\})(h_{\mathbb{H}}(\tau, t_2) - \mathbb{E}\{h_{\mathbb{H}}(\tau, t_2)\})^*\} \\ &= \mathbb{E}\{\tilde{h}_{\mathbb{H}}(\tau, t_1)\tilde{h}_{\mathbb{H}}^*(\tau, t_2)\} \\ &= \mathbb{E}\{\tilde{h}_{\mathbb{H}}(\tau, t)\tilde{h}_{\mathbb{H}}^*(\tau, t + t_2 - t_1)\} \end{aligned} \quad (4)$$

$\bar{h}_{\mathbb{H}}(\tau, t)$  is called the trend and is a slowly time-varying deterministic component.  $\tilde{h}_{\mathbb{H}}(\tau, t)$  is a zero-mean wide-sense stationary random process assumed to be Gaussian. This model describes the UA channel as a multivariate Rician fading process with a slowly time-varying mean.  $\bar{h}_{\mathbb{H}}(\tau, t)$  can be interpreted as the contribution of (pseudo) deterministic physical phenomena to channel fluctuations (wave undulation, range/depth dependence, bathymetry changes, etc.), and  $\tilde{h}_{\mathbb{H}}(\tau, t)$  represents the channel fluctuations attributable to scatterers that result in fast fading. Note that since no particular assumption is made about the correlation of scatterers, the model is very general and includes the WSSUS model as a subset. (Under the WSS assumption, the channel impulse response would satisfy (4) as well as  $\bar{h}_{\mathbb{H}}(\tau, t_1) = \bar{h}_{\mathbb{H}}(\tau, t_2)$ ,  $\forall t_1, t_2 \in \mathbb{R}$ . Under the assumption that  $\mathbb{E}\{\tilde{h}_{\mathbb{H}}(\tau_1, t_1)\tilde{h}_{\mathbb{H}}^*(\tau_2, t_2)\} = 0$  for  $\tau_1 \neq \tau_2$ , the channel would be said to exhibit delay uncorrelated scattering (US).) Without loss of generality, the channel is assumed to be normalized so that

$$\lim_{T \rightarrow \infty} \frac{1}{T} \int_{-T/2}^{T/2} \int_{\tau} \mathbb{E}\{|h_{\mathbb{H}}(\tau, t)|^2\} d\tau dt = 1. \quad (5)$$

We define the channel Rice factor as the power ratio between the deterministic trend and the random component, that is,

$$\kappa = \lim_{T \rightarrow \infty} \frac{1}{T} \frac{\int_{-T/2}^{T/2} \int_{\tau} |\bar{h}_{\mathbb{H}}(\tau, t)|^2 d\tau dt}{\int_{\tau} \mathbb{E}\{|\tilde{h}_{\mathbb{H}}(\tau, t)|^2\} d\tau}. \quad (6)$$

We recall that  $\bar{h}_{\mathbb{H}}(\tau, t)$  is deterministic and that  $\tilde{h}_{\mathbb{H}}(\tau, t)$  is wide-sense stationary so that  $\mathbb{E}\{|\tilde{h}_{\mathbb{H}}(\tau, t)|^2\}$  does not depend on  $t$ .

The ambient noise  $w(t)$  is assumed to be Gaussian and to result from the mixture of four sources [24]: turbulence, shipping, waves, and thermal noise with nonflat power spectral densities (PSDs). We, therefore, modeled  $w(t)$  as a nonwhite zero-mean wide-sense stationary Gaussian random process with correlation function:

$$R_w(t_2 - t_1) \triangleq \mathbb{E}\{w(t_1)w(t_2)^*\}, \quad (7)$$

and PSD

$$W(f) \triangleq \int_{\tau} R_w(\tau) e^{-j2\pi\tau f} d\tau. \quad (8)$$

Simple approximated models for  $R_w(\tau)$  and  $W(f)$  are given in Appendix A.

In addition to the channel impulse response, another channel function that will be important for our treatment is the delay-Doppler spreading function:

$$\begin{aligned} G_{\mathbb{H}}(\tau, \nu) &= \int_{-\infty}^{\infty} h_{\mathbb{H}}(\tau, t) e^{-2j\pi\nu t} dt \\ &= \underbrace{\int_{-\infty}^{\infty} \tilde{h}_{\mathbb{H}}(\tau, t) e^{-2j\pi\nu t} dt}_{\triangleq \tilde{G}_{\mathbb{H}}(\tau, \nu)} \\ &\quad + \underbrace{\int_{-\infty}^{\infty} \bar{h}_{\mathbb{H}}(\tau, t) e^{-2j\pi\nu t} dt}_{\triangleq \bar{G}_{\mathbb{H}}(\tau, \nu)}. \end{aligned} \quad (9)$$

The channel I/O relation (1) can now be written as

$$y(t) = \int_{\tau} \int_{\nu} G_{\mathbb{H}}(\tau, \nu) x(t - \tau) e^{2j\pi\nu t} d\tau d\nu + w(t). \quad (10)$$

The spreading function is assumed to be compactly supported on a rectangle and satisfies

$$\begin{aligned} G_{\mathbb{H}}(\tau, \nu) &= 0, \\ \text{for } (\tau, \nu) &\notin [0, \tau_{\max}] \times \left[-\frac{\nu_{\max}}{2}, \frac{\nu_{\max}}{2}\right], \end{aligned} \quad (11)$$

where  $\tau_{\max}$  and  $\nu_{\max}$  denote the maximum time delay spread and the maximum Doppler spread, respectively. This assumption leads to the following definition of the channel spread factor:

$$\Delta_{\mathbb{H}} \triangleq \tau_{\max} \times \nu_{\max}. \quad (12)$$

Note that this assumption eases the analysis proposed in this paper but is only an approximation of real channels behavior. In practice, to set values to  $\tau_{\max}$  and  $\nu_{\max}$ , it is often required to resort to more empirical definitions (e.g., threshold-based definitions, as used in Section 4.2). Various definitions of delay and Doppler spreads for real channels are discussed in [1, Section 4.5].

**2.3. OFDM Signal.** OFDM signaling schemes can be described by two Weyl-Heisenberg (WH) sets [10, 11, 13]: the one used at transmission, expressed as

$$(g, T, F) \triangleq \left\{ g_{k,n}(t) = g(t - kT) e^{j2\pi n F t}, \|g\|^2 = 1 \right\}_{k,n \in \mathbb{Z}}, \quad (13)$$

and the one used at reception, defined as

$$(\gamma, T, F) \triangleq \left\{ \gamma_{k,n}(t) = \gamma(t - kT) e^{j2\pi n F t}, \|\gamma\|^2 = 1 \right\}_{k,n \in \mathbb{Z}}, \quad (14)$$

where  $T, F > 0$  are the time and frequency shifts of the prototype function  $g(t)$  and  $\gamma(t)$ . The signaling scheme is here assumed to be (bi)orthogonal, so that

$$\langle g_{k,n}, \gamma_{k',n'} \rangle = \delta(k - k') \delta(n - n'). \quad (15)$$

To ease the readability of the results presented in the sequel, we shall restrict our analysis to orthogonal receive pulses (i.e.,  $\langle \gamma_{k,n}, \gamma_{k',n'} \rangle = \delta(k - k') \delta(n - n')$ ). (Note that nonorthogonal receive pulses introduce noise correlation and noise-enhancement that can be harmful for advanced equalization techniques. As an example, cyclic prefix based OFDM receiver are orthogonal whereas zero-padding receivers (with  $TF > 1$ ) are not.)

The transmitted signal is

$$x(t) = \sum_{k=0}^{K-1} \sum_{n=0}^{N-1} x_{k,n} g_{k,n}(t), \quad (16)$$

where  $N$  is the number of subcarriers, and  $KT$  is the approximate duration of the transmitted signal.  $x_{k,n}$  denotes the data symbols. Since little is known about the exact structure of optimal signaling under the general constraints listed in the introduction, we restrict our analysis to zero-mean, independent and identically distributed (i.i.d.) symbols. We assume that the average power of the input signals is limited so that

$$\frac{1}{KT} \sum_{k=0}^{K-1} \sum_{n=0}^{N-1} \mathbb{E} \{ |x_{k,n}|^2 \} = P, \quad (17)$$

where  $P < +\infty$  is the maximum average power available. The signal-to-noise ratio (SNR) is then defined as

$$\rho \triangleq \frac{P}{\int_0^B W(f)}, \quad (18)$$

where  $B = NF$  denotes the system bandwidth.

At reception, the output signal  $y(t)$  is projected onto the set  $\{\gamma_{k,n}(t)\}$  to obtain

$$y_{k,n} \triangleq \langle y, \gamma_{k,n} \rangle = \langle \mathbb{H}x, \gamma_{k,n} \rangle + \underbrace{\langle w, \gamma_{k,n} \rangle}_{\triangleq w_{k,n}}. \quad (19)$$

$y_{k,n}$  can be developed as

$$\begin{aligned} y_{k,n} &= \langle \mathbb{H}g_{k,n}, \gamma_{k,n} \rangle x_{k,n} \\ &\quad + \sum_{\substack{k'=0 \\ (k',n') \neq (k,n)}}^{K-1} \sum_{n'=0}^{N-1} \langle \mathbb{H}g_{k',n'}, \gamma_{k,n} \rangle x_{k',n'} + w_{k,n}, \end{aligned} \quad (20)$$

where the second term on the right-hand side (RHS) of (20) represents the intersymbol and intercarrier interference.

The relation (20) can be compactly expressed as

$$\mathbf{y} = \mathbf{H}\mathbf{x} + \mathbf{w}, \quad (21)$$

where the channel input and output vectors of size  $NK \times 1$  are respectively defined by

$$\begin{aligned} \mathbf{x} &\triangleq [\mathbf{x}_0^T \mathbf{x}_1^T \cdots \mathbf{x}_{K-1}^T]^T, \\ \text{with } \mathbf{x}_k &\triangleq [x_{k,0} \ x_{k,1} \ \cdots \ x_{k,N-1}]^T, \\ \mathbf{y} &\triangleq [\mathbf{y}_0^T \mathbf{y}_1^T \cdots \mathbf{y}_{K-1}^T]^T, \\ \text{with } \mathbf{y}_k &\triangleq [y_{k,0} \ y_{k,1} \ \cdots \ y_{k,N-1}]^T, \end{aligned} \quad (22)$$

and where  $\mathbf{w}$  is defined analogously. The  $NK \times NK$  channel matrix  $\mathbf{H}$  is given by

$$\mathbf{H} \triangleq \begin{pmatrix} \mathbf{H}^{(0,0)} & \dots & \mathbf{H}^{(0,K)} \\ \vdots & \ddots & \vdots \\ \mathbf{H}^{(K,0)} & \dots & \mathbf{H}^{(K,K)} \end{pmatrix}, \quad (23)$$

where the matrix block  $\mathbf{H}^{(k,k')}$  of size  $N \times N$  satisfies

$$\left[ \mathbf{H}^{(k,k')} \right]_{n,n'} \triangleq \langle \mathbb{H} g_{k',n'}, \gamma_{k,n} \rangle. \quad (24)$$

Since we do not neglect interference, the matrix  $\mathbf{H}$  is not diagonal and can be decomposed as follows:

$$\mathbf{H} = \text{diag}(\mathbf{h}) + \mathbf{Z}, \quad (25)$$

where  $\mathbf{h}$  is the direct channel vector corresponding to the main diagonal of  $\mathbf{H}$  and  $\mathbf{Z}$  is the ISI/ICI cross-channel matrix containing the offdiagonal terms of  $\mathbf{H}$ .

### 3. Information Theoretic Analysis of UA-OFDM Systems

Three fundamental characteristics of the sets  $(g, T, F)$  and  $(\gamma, T, F)$  are generally involved in the optimization/performance of MC systems:

- (i) *(bi)orthogonality*: for an ideal channel where  $y(t) = x(t)$ , perfect demodulation is obtained iff  $g(t)$ , and  $\gamma(t)$  satisfies the condition (15);
- (ii) *localization*: localization of a prototype function involves the Heisenberg uncertainty principle and characterizes its time-frequency concentration so that it directly affects the power of interference observed at reception;
- (iii) *density*: spectral efficiency of MC systems is directly proportional to the density  $1/TF$  of the time-frequency grid that supports the transmission scheme. For instance, adding guard intervals between OFDM symbols reduces the density due to the fact that  $TF > 1$  in this case, but as the product  $TF$  gets larger, the power of ISI/ICI diminishes.

Ideally, we would like to construct a MC system that is (bi)orthogonal, with well-localized prototype functions (to limit the interference) and with a dense time-frequency grid (to maximize the spectral efficiency). However, these three conditions cannot be satisfied simultaneously due to the Balian-Low theorem [25, Th. 4.1.1.] More precisely, well-localized (bi)orthogonal pulses can only be found for  $TF > 1$  (see [26, Ch. 2] for more details). This loss in spectral efficiency is usually the price to pay to mitigate ISI/ICI over double-dispersive channels. (Note that other approaches, e.g. [13] or [27], privilege localization and spectral efficiency over (bi)orthogonality.)

These elements highlight the difficulty of finding a compromise between a low interference at reception and a maximal use of the degrees of freedom offered by the channel. The optimal trade-off between low interference

and high spectral efficiency is a key ingredient in OFDM system design that has yet to be found. To provide some guidelines that will help us to progress toward the optimal solution, we suggest to study the signal-to-interference ratio as well as the information rate of UA-OFDM systems. The information rate, defined as the amount of information that can be transmitted with arbitrarily small error probability, appears as a good figure of merit for system design as it jointly considers interference and spectral efficiency.

**3.1. Signal-to-Interference Ratio.** The signal-to-interference ratio at the symbol  $k$  and the subcarrier  $n$  is defined as

$$\text{SIR}_{k,n} \triangleq \frac{\mathbb{E} \left\{ \left| \left[ \mathbf{H}^{(k,k)} \right]_{n,n} x_{k,n} \right|^2 \right\}}{\mathbb{E} \left\{ \left| \sum_{\substack{k'=0 \\ (k',n') \neq (k,n)}}^{K-1} \sum_{n'=0}^{N-1} \left[ \mathbf{H}^{(k,k')} \right]_{n,n'} x_{k',n'} \right|^2 \right\}} \quad (26)$$

$$\stackrel{(a)}{=} \frac{\mathbb{E} \left\{ \left| \left[ \mathbf{H}^{(k,k)} \right]_{n,n} \right|^2 \right\}}{\sum_{\substack{k'=0 \\ (k',n') \neq (k,n)}}^{K-1} \sum_{n'=0}^{N-1} \mathbb{E} \left\{ \left| \left[ \mathbf{H}^{(k,k')} \right]_{n,n'} \right|^2 \right\}},$$

where (a) follows from the assumption that the  $x_{k,n}$  are i.i.d. with zero mean. The numerator represents the average power of the diagonal entries of  $\mathbf{H}$ , and the denominator the power of its offdiagonal entries. Let  $A_{g,\gamma}(\tau, \nu)$  be the cross-ambiguity function of  $g(t)$  and  $\gamma(t)$  defined as follows:

$$A_{g,\gamma}(\tau, \nu) \triangleq \int_t g(t) \gamma^*(t - \tau) e^{-j2\pi\nu t} dt. \quad (27)$$

The signal as well as the interference power can be expressed as a function of  $A_{g,\gamma}(\tau, \nu)$ . More precisely, as shown in Appendix B:

$$\mathbb{E} \left\{ \left| \left[ \mathbf{H}^{(k,k)} \right]_{n,n} \right|^2 \right\} \approx \int_{\tau} \int_{\tau'} \int_{\nu} \tilde{S}_{\text{FH}}(\tau, \tau', \nu) A_{\gamma,g}^*(\tau, \nu) \times A_{\gamma,g}(\tau', \nu) e^{j2\pi n F(\tau' - \tau)} d\nu d\tau' d\tau + \left| \int_{\tau} \bar{h}_{\text{FH}}(\tau, kT) A_{\gamma,g}^*(\tau, 0) e^{-j2\pi n F\tau} d\tau \right|^2, \quad (28)$$

where  $\tilde{S}_{\text{FH}}(\tau, \tau', \nu)$  is the channel scattering function defined as

$$\tilde{S}_{\text{FH}}(\tau, \tau', \nu) = \int_u \tilde{R}_{\text{FH}}(\tau, \tau', u) e^{-2j\pi\nu u} du, \quad (29)$$

with  $\tilde{R}_{\text{FH}}(\tau, \tau', u) \triangleq \mathbb{E} \{ \tilde{h}_{\text{FH}}(\tau, t) \tilde{h}_{\text{FH}}^*(\tau', t + u) \}$ . Note that in the case where the scatterers are assumed to be uncorrelated, the scattering function is simplified to  $\tilde{S}_{\text{FH}}(\tau, \tau', \nu) \delta(\tau' - \tau)$ .

The first term on the RHS of (28) represents the power carried by the fast fading random part of the channel,

and the second term corresponds to the deterministic part of the channel. Similarly, the interference power satisfies

$$\sum_{k'=0}^{K-1} \sum_{n'=0}^{N-1} \mathbb{E} \left\{ \left| \left[ \mathbf{H}^{(k,k')} \right]_{n,n'} \right|^2 \right\} \triangleq \tilde{\sigma}_{I_n}^2 + \bar{\sigma}_{I_{k,n}}^2, \quad (30)$$

where  $\tilde{\sigma}_{I_n}^2$  is the interference power corresponding to the random part of the channel and is expressed as

$$\begin{aligned} \tilde{\sigma}_{I_n}^2 = & \sum_{k'=1-K}^{K-1} \sum_{n'=1-N}^{N-1} \int_{\tau} \int_{\tau'} \int_{\nu} \tilde{S}_{\mathbb{H}}(\tau, \tau', \nu) \\ & \times A_{\gamma,g}^*(\tau + k'T, \nu + n'F) \quad (31) \\ & \times A_{\gamma,g}(\tau' + k'T, \nu + n'F) \\ & \times e^{j2\pi F(n'+n)(\tau'-\tau)} d\nu d\tau' d\tau. \end{aligned}$$

Note that  $\tilde{\sigma}_{I_n}^2$  does not depend on  $k$  since, according to (4),  $\tilde{h}_{\mathbb{H}}(\tau, t)$  is wide-sense stationary.

$\bar{\sigma}_{I_{k,n}}^2$  is the interference power due to the deterministic part of the channel and is given by

$$\begin{aligned} \bar{\sigma}_{I_{k,n}}^2 = & \sum_{k'=1-K}^{K-1} \sum_{n'=1-N}^{N-1} \left| \int_{\tau} \bar{h}_{\mathbb{H}}(\tau, (k'+k)T) \right. \\ & \times A_{\gamma,g}^*(\tau + k'T, n'F) \quad (32) \\ & \left. e^{-j2\pi F(n'+n)\tau} d\tau \right|^2. \end{aligned}$$

Using the above quantities, we now define the average signal-to-interference ratio as

$$\overline{\text{SIR}} \triangleq \lim_{K \rightarrow \infty} \frac{1}{KN} \sum_{k=0}^{K-1} \sum_{n=0}^{N-1} \text{SIR}_{k,n}. \quad (33)$$

**3.2. Achievable Rate.** Let  $\mathcal{P}_{\mathbf{x}}$  be the set of probability distributions on  $\mathbf{x}$  that satisfy the constraints given in (17). The maximum achievable rate for an OFDM system is then given by [28]

$$C = \lim_{K \rightarrow \infty} \frac{1}{KT} \sup_{\mathcal{P}_{\mathbf{x}}} I(\mathbf{y}; \mathbf{x}), \quad (34)$$

where  $I(\mathbf{y}; \mathbf{x}) = h_E(\mathbf{y}) - h_E(\mathbf{y} | \mathbf{x})$  is the mutual information between  $\mathbf{y}$  and  $\mathbf{x}$  with  $h_E(\mathbf{y})$ , the differential entropy of  $\mathbf{y}$ . In the *noncoherent* setting, the maximum achievable rate is notoriously hard to characterize analytically. However, by evaluating the mutual information  $I(\mathbf{y}; \mathbf{x})$  for a specific input distribution, and by relying on the following inequality on mutual information [29]:

$$I(\mathbf{y}; \mathbf{x}) \geq I(\mathbf{y}; \mathbf{x} | \mathbf{H}) - I(\mathbf{y}; \mathbf{H} | \mathbf{x}), \quad (35)$$

we can get a lower bound on  $C$  that yields an information-theoretic criterion useful for the analysis of UA-OFDM

systems. Note that the first term on the right-hand side of (35) corresponds to the *coherent* information rate under perfect channel knowledge at reception, and the second term can be interpreted as a penalty term that quantifies the rate loss due to the lack of channel knowledge.

**Theorem 1.** *The maximum achievable rate of an OFDM system with i.i.d. input symbols satisfying the average-power constraint (17) and transmitting over the channel modeled by (2) is lower-bounded as  $C^{L1} \leq C$ , where*

$$\begin{aligned} C^{L1} = & \lim_{K \rightarrow \infty} \frac{1}{KT} \mathbb{E}_{\mathbf{H}} \left\{ \log \det \left( \mathbf{I} + \frac{PT}{N} \mathbf{H} \mathbf{H}^{\dagger} \text{diag}(\mathbf{r}_w)^{-1} \right) \right\} \\ & - \inf_{0 < \alpha < 1} \frac{1}{KT} \left[ \log \det \left( \mathbf{I} + \frac{PT}{N\alpha} \mathbf{R}_{\mathbf{h}} \text{diag}(\mathbf{r}_w)^{-1} \right) \right. \\ & \left. + K \sum_{n=0}^{N-1} \log \left( 1 + \frac{PT}{N(1-\alpha)r_w(n)} \tilde{\sigma}_{I_n}^2 \right) \right]. \quad (36) \end{aligned}$$

Here, the entries of the  $NK \times 1$  noise power vector  $\mathbf{r}_w$  are defined as

$$r_w(n+kK) \triangleq W(nF), \quad n \in [0, N-1], \quad k \in [0, K-1], \quad (37)$$

and  $\mathbf{R}_{\mathbf{h}}$  denotes the covariance matrix of the direct channel vector  $\mathbf{h}$ , whose entries are expressed as

$$\begin{aligned} \left[ \mathbf{R}_{\mathbf{h}}^{(k,k')} \right]_{n,n'} = & \int_{\tau} \int_{\tau'} \int_{\nu} \tilde{S}_{\mathbb{H}}(\tau, \tau', \nu) A_{\gamma,g}^*(\tau, \nu) A_{\gamma,g}(\tau', \nu) \\ & \times e^{j2\pi\nu T(k-k')} e^{j2\pi F(n'\tau' - n\tau)} d\nu d\tau' d\tau. \quad (38) \end{aligned}$$

*Proof.* See Appendix C.  $\square$

Note that the penalty term in (36) only depends on the random component of the channel so that acquiring CSI at reception gets more costly as the channel gets more fluctuating (e.g., estimating  $\mathbf{H}$  gets more difficult as the power of its off-diagonal entries increases).

To get a better insight into the achievable rate, the following corollary presents a simplified scenario of transmission that leads to a more tractable expression of the lower bound.

**Corollary 2.** *In the case where the noise is assumed to be white and the scatterers uncorrelated, the maximum achievable rate is lower bounded as  $C^{L2} \leq C$ , where*

$$\begin{aligned} C^{L2} = & \lim_{K \rightarrow \infty} \frac{1}{KT} \mathbb{E}_{\mathbf{H}} \left\{ \log \det \left( \mathbf{I} + \rho TF \mathbf{H} \mathbf{H}^{\dagger} \right) \right\} \\ & - \inf_{0 < \alpha < 1} \frac{B}{TF} \left[ \int_{-1/2}^{1/2} \log \left( 1 + \frac{\rho TF}{\alpha} \tilde{s}(\theta) \right) d\theta \quad (39) \right. \\ & \left. + \log \left( 1 + \frac{\rho TF}{1-\alpha} \tilde{\sigma}_I^2 \right) \right]. \end{aligned}$$

Here,  $\rho$  denotes the SNR defined in (18),  $\tilde{s}(\theta)$  is the PSD of the zero-mean stationary channel process  $\{h_{k,n} - \mathbb{E}\{h_{k,n}\}\}_k$ , and is expressed as

$$\tilde{s}(\theta) = \sum_{k=-\infty}^{\infty} \int_{\tau} \int_{\nu} \tilde{S}_{\mathbb{H}}(\tau, \nu) |A_{\nu, g}(\tau, \nu)|^2 e^{j2\pi\nu k T} d\nu d\tau e^{-j2\pi k \theta}, \quad (40)$$

and  $\tilde{\sigma}_I^2$  satisfies

$$\begin{aligned} \tilde{\sigma}_I^2 = & \sum_{\substack{k'=1-K \\ (k', n') \neq (0,0)}}^{K-1} \sum_{n'=1-N}^{N-1} \int_{\tau} \int_{\nu} \tilde{S}_{\mathbb{H}}(\tau, \nu) \\ & \times |A_{\nu, g}^*(\tau + k'T, \nu + n'F)|^2 d\nu d\tau. \end{aligned} \quad (41)$$

*Proof.* See Appendix D.  $\square$

Note that the scenario depicted in Corollary 2 may be acceptable for systems transmitting in small bandwidth (on the order of kHz), where the noise PSD can be assumed flat and where the propagation loss associated with each channel path is approximately constant over the transmit bandwidth, thus reducing the correlation between channel arrival paths.

#### 4. Numerical Analysis

We next examine the signal-to-interference ratio and the bounds of the previous section in various scenarios. Using a synthetic channel model, impact of time-frequency dispersion on the information rate is first discussed in Section 4.1. Bounds on the information rate applied to experimental double-dispersive UA channels surveyed at sea are then analyzed in Section 4.2. Common OFDM systems with rectangular pulse shaping are used as a framework in our investigation.  $g(t)$  and  $\gamma(t)$  are thus defined as

$$\begin{aligned} g(t) &= \begin{cases} \frac{1}{\sqrt{T}} & \text{if } 0 < t \leq T, \\ 0 & \text{otherwise,} \end{cases} \\ \gamma(t) &= \begin{cases} \frac{1}{\sqrt{T - T_g}} & \text{if } T_g < t \leq T, \\ 0 & \text{otherwise,} \end{cases} \end{aligned} \quad (42)$$

where  $T_g = T - 1/F$  denotes the guard time between OFDM symbols.

**4.1. Synthetic Channel Model.** To illustrate the impact of channel dispersion on the performance of OFDM systems, we first consider a canonical channel model. It has no particular physical justification, but mimics a bad scenario from the viewpoint of a communication system [20] and will help us to provide general trends on OFDM system robustness against channel dispersion.

We assume the following environment:

- (i) Rayleigh fading, that is,  $\kappa = 0$ ;

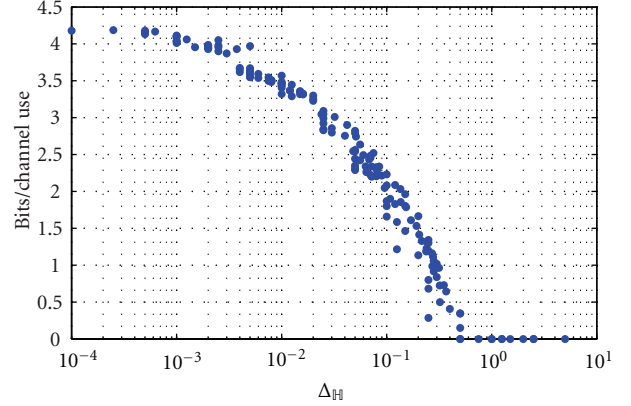


FIGURE 1: Lower bound (39) as a function of the channel spread factor for a Rayleigh fading channel with a brick-shaped scattering function and white Gaussian Noise.  $\rho = 15$  dB and  $B = 5$  kHz.

- (ii) uncorrelated scatterers with a brick-shaped scattering function  $\tilde{S}_{\mathbb{H}}(\tau, \nu) = 1/\Delta_{\mathbb{H}}$ ;
- (iii) white Gaussian noise.

Figure 1 shows the information rate as a function of the channel spread factor  $\Delta_{\mathbb{H}}$  defined in (12). The grid parameters  $T$  and  $F$  are chosen according to the grid-matching rule [30]:  $T/F = \tau_{\max}/\nu_{\max}$ , and  $TF$  is chosen so as to maximize (39).  $\rho$  is set to 15 dB and  $B = 5$  kHz.  $\tau_{\max}$  is randomly chosen between 1 and 50 ms, and  $\nu_{\max}$  between 0.1 and 50 Hz. As expected, the achievable rate of OFDM systems is strongly affected by both the delay and the Doppler spread and decreases as the channel gets more dispersive. Note that as the rectangular prototype function is not equally localized in time and frequency, there is not a single performance point for a given spread factor. For  $\Delta_{\mathbb{H}} \leq 10^{-3}$  and  $\rho = 15$  dB, OFDM systems should be able to communicate at roughly 4 bits/s/Hz, which represents 80% of the achievable rate in an AWGN channel at the same SNR. Such systems can be relatively efficient as long as  $\Delta_{\mathbb{H}} < 10^{-1}$ . However, for  $\Delta_{\mathbb{H}} > 1$ , there is no guarantee that any data can be reliably transmitted.

**4.2. Experimental UA Channels Recorded at Sea.** Three different shallow water channels, recorded in the Atlantic ocean and the Mediterranean sea, are considered. Table 1 summarizes the main characteristics of these channels, and Figure 2 shows the evolution of their respective power delay profiles as a function of time. Channel (a) results from data collected by the DGA-TN (Direction Générale de l'Armement-Techniques Navales) in the Atlantic ocean off Brest (France) in October 2007, and channels (b) and (c) result from sea trials performed by Thales Underwater Systems in the Mediterranean sea off La Ciotat (France) in October 2004. From the raw data and for each channel, the trend  $\bar{h}_{\mathbb{H}}(\tau, t)$  is separated from the random component  $\tilde{h}_{\mathbb{H}}(\tau, t)$  using the empirical mode decomposition method [2]. The maximum time delay spread is estimated as the difference between the longest and the shortest delay, where

TABLE 1: Summary of at sea experiments.

Channel	Center frequency (kHz)	Bandwidth (kHz)	Distance (m)	Water depth (m)	$\tau_{\max}$ (ms)	$\nu_{\max}$ (Hz)	$\kappa$ (dB)
(a)	17.5	2.9	1000	10–40	2.1	1.5	15.5
(b)	6	1	2500	60–120	35	2.7	4.9
(c)	6	1	5000	60–120	47	3.2	1.6

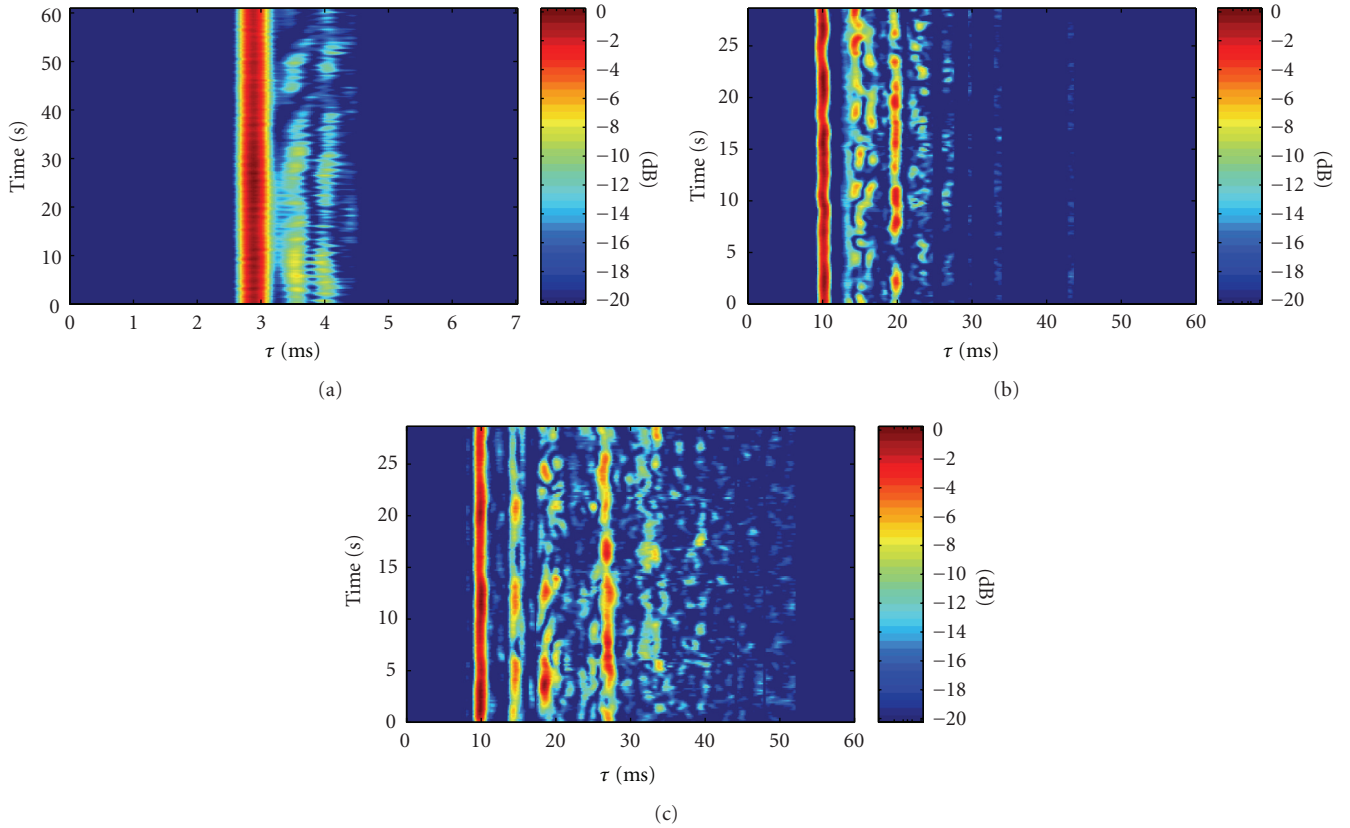
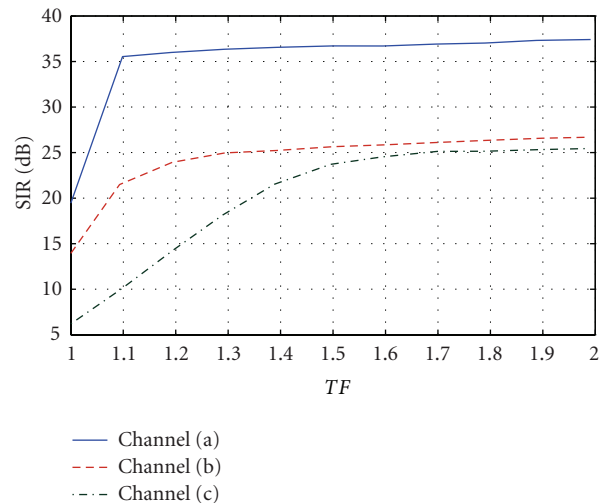


FIGURE 2: Time evolution of the power delay profiles of the channels depicted in Table 1.

the average power delay profile exceeds 1% of its maximum value (i.e., taps that are 20 dB below the strongest tap are assumed to result from noise and are artificially set to 0). The scattering function  $\tilde{S}_{\text{H}}(\tau, \tau', \nu)$  is obtained from a correlogram estimate of PSD. The maximum Doppler spread is similarly defined from the Doppler power spectrum as the maximum delay spread from the average power delay profile. (The Doppler power spectrum is defined as  $\int_{\tau} \int_{\tau'} \tilde{S}_{\text{H}}(\tau, \tau', \nu) d\tau' d\tau$ .) To compute the various expectations required to evaluate the bound  $C^{L1}$ , a large number of channel realizations are generated using the channel stochastic replay approach presented in [2]. Throughout this analysis,  $T$  and  $F$  satisfy the grid-matching rule mentioned previously (i.e.,  $T/F = \tau_{\max}/\nu_{\max}$ ).

In Figure 3, the average SIR is plotted as a function of  $TF$  for the three channels. It can be noticed that as  $TF$  increases, the duration of the guard interval increases as well, which results in a lower interference at reception. The SIR increases

FIGURE 3: Average signal-to-interference ratio as a function of  $TF$ .

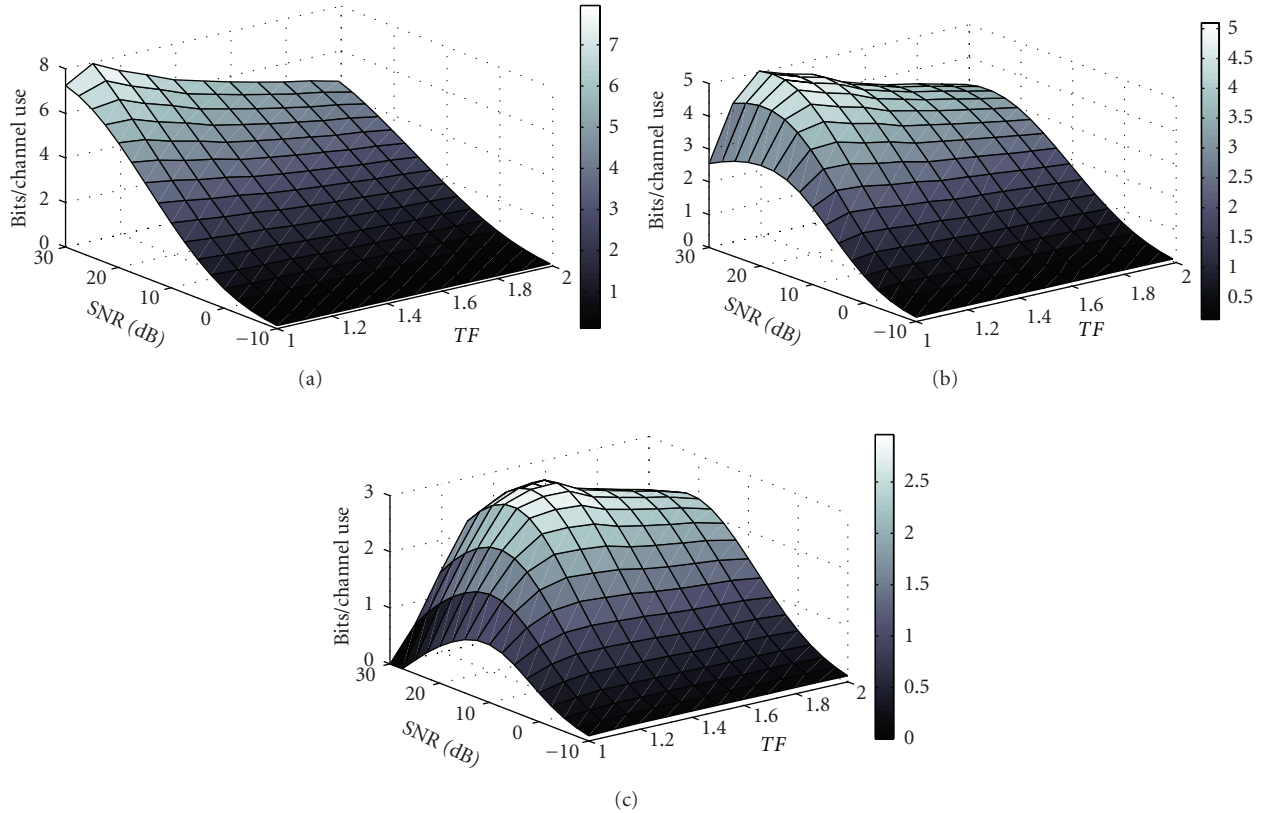


FIGURE 4: Lower-bound  $C^{L1}$  as a function of  $TF$  and the SNR  $\rho$  for the three channels depicted in Table 1.

significantly as long as  $TF$  is such that the guard interval duration is lower than the maximum time delay spread. A further increase of  $TF$  produces a slighter increase of the SIR, which indicates that ISI is more detrimental than ICI. The average SIR also depends on the channel properties. As expected, for a given  $TF$ , the larger the spread factor, the smaller the SIR.

Through the evolution of the achievable rate (36) as a function of  $TF$  and the SNR, Figure 4 shows possible trade-offs between interference minimization and loss of signal-space dimensions. It provides a measure of reassurance that current practice in designing OFDM systems for underwater channels is reasonable. That is, oversizing guard intervals duration (i.e., choosing large  $TF$ ) compared to the channel maximum delay spread is not much detrimental to the information rate, whereas a too small  $TF$  can significantly decrease this rate, especially in highly dispersive channels such as channel (c). The results of Figure 4 also suggest that significant rate improvements are possible compared to state-of-the-art UA-OFDM systems. For instance, in channels (b) and (c), reliable OFDM transmissions at 2 to 4 bits/sec/Hz are achievable provided an average signal-to-noise ratio of 15 to 20 dB, whereas in the same SNR range, single-input single-output UA-OFDM systems usually operate with a spectral efficiency around 1 bit/sec/Hz [6–8]. The lower bound (36) obtained for channel (a) corroborates the results of the previous subsection related to channels with

small spread factors, that is, over such channels we should be able to communicate at 80% of the theoretical rate obtained over AWGN channels.

UA-OFDM systems are not genie-aided and have to spend some resources to acquire CSI at reception, with the consequence of decreasing the data rate. Insights on how CSI impact the information rate can be obtained through the numerical analysis of the ratio  $C^{L1}/C^{\text{coh}}$ , where  $C^{\text{coh}}$  is defined as the achievable rate of UA-OFDM systems with perfect channel knowledge at reception. According to Appendix C, we have

$$C^{\text{coh}} = \lim_{K \rightarrow \infty} \frac{1}{KT} \mathbb{E}_{\mathbf{H}} \left\{ \log \det \left( \mathbf{I} + \frac{PT}{N} \mathbf{H} \mathbf{H}^{\dagger} \text{diag}(\mathbf{r}_w)^{-1} \right) \right\}, \quad (43)$$

which corresponds to the first term on the RHS of (36). Note that  $C^{\text{coh}}$  is also an upperbound on  $C$ . (This can easily be shown by noticing that  $I(\mathbf{y}; \mathbf{x}) \leq I(\mathbf{y}; \mathbf{x} | \mathbf{H})$ .) As shown in Figure 5, the penalty induced by the absence of CSI is stronger for channels with larger Doppler spread (estimating  $\mathbf{H}$  gets more difficult as the channel starts to fluctuate more rapidly) and can lead up to a 30% rate loss for a SNR of 20 dB. In addition,  $C^{L1}/C^{\text{coh}}$  decreases with the SNR, which indicates that CSI acquisition may become a rate-limiting factor at high SNR.

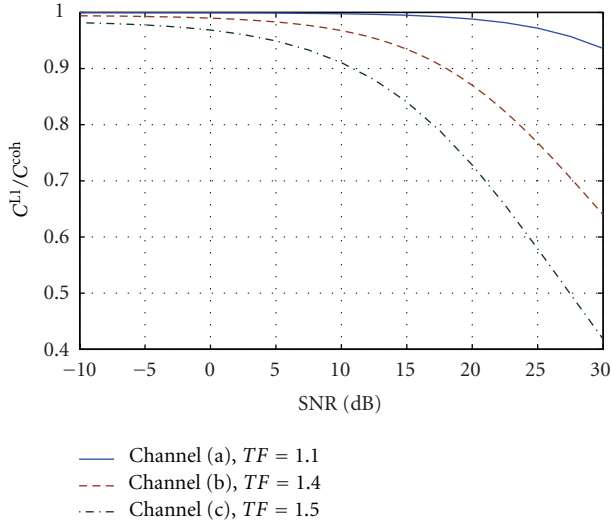


FIGURE 5: Lower-bound  $C^{L1}$  normalized with respect to coherent information rate  $C^{\text{coh}}$ . For each channel,  $TF$  is chosen such that there is no ISI.

## 5. Conclusions and Perspectives

The information-theoretic analysis provided in this paper led to the following conclusions:

- (i) the information rate decreases with the channel spread factor but remains acceptable (i.e., greater than 1 bits/sec/Hz) as long as this factor is smaller than  $10^{-1}$  and the signal-to-noise ratio is greater than 15 dB;
- (ii) numerical assessments on real UA channels with spread factors around  $10^{-1}$  showed that reliable OFDM transmissions at 2 to 4 bits/sec/Hz are achievable provided an average signal-to-noise ratio of 15 to 20 dB;
- (iii) current practices in designing OFDM systems for underwater channels are reasonable. More precisely, slightly oversizing guard intervals duration compared to the channel maximum delay spread is not much detrimental to the information rate, whereas underestimating this duration can be devastating.

Although quite realistic, the system model used in this paper could be more constrained. In particular, to strengthen our results, it would be interesting to add to our model a peak-power limitation, as in [31]. It is well known that OFDM systems can be sensitive to this limitation when power amplifiers do not operate with a large backoff. One way to tackle the problem would be to consider, in the information theoretic-treatment, the nonlinear distortion due to possible clipping as additional noise. Another point that deserves further attention is to study the information rate bound  $C^{L1}$  as a figure of merit for pulse-shaping optimization. While experimental results showed that large rates can be achieved with rectangular pulses, the bound

provided in this paper could be tightened by maximizing it over all Weyl-Heisenberg sets.

## Appendices

### A. Noise Model Approximation

To model the ambient noise in the sea, four sources are usually considered: turbulence, shipping, waves, and thermal noise. These four noise components can be modeled by a colored Gaussian noise with the following empirical power spectral density (PSD) given in dB re  $\mu\text{Pa}^2$  per Hz as a function of frequency  $f$  in Hz [24]:

$$\text{turbulence: } 10 \log W_t(f) = 17 - 30 \log(10^{-3} f),$$

$$\begin{aligned} \text{shipping: } 10 \log W_s(f) = & 40 + 20(s - 0.5) + 26 \log(10^{-3} f) \\ & - 60 \log(10^{-3} f + 0.03), \end{aligned}$$

$$\begin{aligned} \text{waves: } 10 \log W_w(f) = & 50 + 7.5v^2 + 20 \log(10^{-3} f) \\ & - 40 \log(10^{-3} f + 0.4), \end{aligned}$$

$$\text{thermal noise: } 10 \log W_{\text{th}}(f) = -15 + 20 \log(10^{-3} f), \quad (\text{A.1})$$

where  $0 \leq s \leq 1$  is the shipping activity, and  $v$  is the wind speed in m/s. The baseband equivalent noise PSD, as defined in (8), is then given by

$$\begin{aligned} W(f) = & W_t(f + f_c) + W_s(f + f_c) \\ & + W_w(f + f_c) + W_{\text{th}}(f + f_c), \end{aligned} \quad (\text{A.2})$$

where  $f_c$  is the carrier frequency corresponding the 0th subcarrier.

As noticed in [24], in the frequency region where most OFDM communication systems operate (1 kHz to 100 kHz), the noise PSD decays almost linearly on the logarithmic scale. (Surface motion, caused by wind-driven waves is the main contributor to the noise in that frequency range.) This indicates that a simple expression may be found for the auto-correlation function  $R_w(\tau)$ . In fact, by expressing  $R_w(\tau)$  as

$$R_w(\tau) = \beta e^{-\mu|\tau|} e^{-j2\pi f_c \tau}, \quad (\text{A.3})$$

where  $\beta > 0$  and  $\mu > 0$ , we get the following PSD [32]:

$$W(f) = \beta \frac{2\mu}{\mu^2 + 4\pi(f + f_c)^2}, \quad (\text{A.4})$$

that turns out to be a good approximation of the noise PSD in frequency range of interest. This approximation is shown in Figure 6 with  $\mu = 5 \cdot 10^3$ , and  $\beta$  is chosen such that the noise powers of models (A.2) and (A.4) perfectly match at 10 kHz.

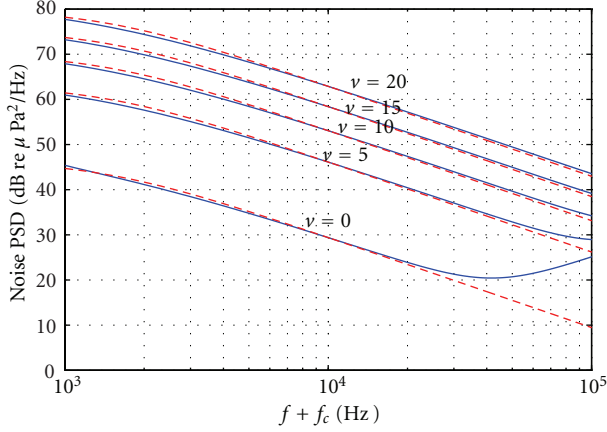


FIGURE 6: Power spectral density of the ambient noise for various wind speeds  $\nu$ ,  $s$  is set to 0.5. The solid lines show the model (A.2) and dashed lines the one of (A.4).  $f_c$  is the carrier frequency corresponding the 0th subcarrier.

## B. Computation of the Signal and the Interference Power

For all  $k, k', n, n' \in \mathbb{Z}$ , we have that

$$\begin{aligned}
 \left[ \mathbf{H}^{(k,k')} \right]_{n,n'} &\triangleq \langle \mathbb{H} g_{k',n'}, \gamma_{k,n} \rangle \\
 &\stackrel{(a)}{=} \int_t \int_\tau \int_\nu G_{\mathbb{H}}(\tau, \nu) g(t - k'T - \tau) e^{j2\pi n' F(t-\tau)} \\
 &\quad \times e^{j2\pi \nu t} \gamma^*(t - kT) e^{-j2\pi n F t} d\nu d\tau dt \\
 &\stackrel{(b)}{=} \int_\tau \int_\nu G_{\mathbb{H}}(\tau, \nu) e^{-j2\pi n' F \tau} \\
 &\quad \times \left[ \int_t g^*(t - k'T - \tau) \gamma(t - kT) \right. \\
 &\quad \left. \times e^{-j2\pi \nu t} e^{-j2\pi(n'-n)Ft} dt \right]^* d\nu d\tau \\
 &\stackrel{(c)}{=} \int_\tau \int_\nu G_{\mathbb{H}}(\tau, \nu) \\
 &\quad \times A_{\gamma,g}^*(\tau + (k' - k)T, \nu + (n' - n)F) \\
 &\quad \times e^{-j2\pi n' F \tau} e^{j2\pi(\nu + (n'-n)F)kT} d\nu d\tau, \tag{B.1}
 \end{aligned}$$

where (a) and (b) follows from (9), (13), and (14), and (c) follows from the change of variables  $t' = t - kT$  and from (27).

From this expression, we can now derive the signal power

$$\begin{aligned}
 &\mathbb{E} \left\{ \left| \left[ \mathbf{H}^{(k,k)} \right]_{n,n} \right|^2 \right\} \\
 &\stackrel{(a)}{=} \mathbb{E} \left\{ \left| \int_\tau \int_\nu (\bar{G}_{\mathbb{H}}(\tau, \nu) + \tilde{G}_{\mathbb{H}}(\tau, \nu)) \right|^2 \right\}
 \end{aligned}$$

$$\begin{aligned}
 &\times A_{\gamma,g}^*(\tau, \nu) e^{j2\pi(\nu kT - nF\tau)} d\nu d\tau \Big|^2 \Big\}, \\
 &\stackrel{(b)}{\approx} \mathbb{E} \left\{ \left| \int_\tau \int_\nu \tilde{G}_{\mathbb{H}}(\tau, \nu) A_{\gamma,g}^*(\tau, \nu) e^{j2\pi(\nu kT - nF\tau)} d\nu d\tau \right|^2 \right\} \\
 &\quad + \left| \int_\tau \bar{h}_{\mathbb{H}}(\tau, kT) A_{\gamma,g}^*(\tau, 0) e^{-j2\pi n F \tau} d\tau \right|^2, \\
 &\stackrel{(c)}{=} \int_\tau \int_\nu \int_{\tau'} \int_{\nu'} \mathbb{E} \left\{ \tilde{G}_{\mathbb{H}}(\tau, \nu) \tilde{G}_{\mathbb{H}}^*(\tau', \nu') \right\} A_{\gamma,g}^*(\tau, \nu) A_{\gamma,g}(\tau', \nu') \\
 &\quad \times e^{j2\pi(\nu kT - nF\tau)} \\
 &\quad \times e^{-j2\pi(\nu' kT - nF\tau')} d\nu' d\tau' d\nu d\tau \\
 &\quad + \left| \int_\tau \bar{h}_{\mathbb{H}}(\tau, kT) A_{\gamma,g}^*(\tau, 0) e^{-j2\pi n F \tau} d\tau \right|^2, \\
 &\stackrel{(d)}{=} \int_\tau \int_{\tau'} \int_\nu \tilde{S}_{\mathbb{H}}(\tau, \tau', \nu) A_{\gamma,g}^*(\tau, \nu) A_{\gamma,g}(\tau', \nu) \\
 &\quad \times e^{j2\pi n F(\tau' - \tau)} d\nu d\tau' d\tau \\
 &\quad + \left| \int_\tau \bar{h}_{\mathbb{H}}(\tau, kT) A_{\gamma,g}^*(\tau, 0) e^{-j2\pi n F \tau} d\tau \right|^2, \tag{B.2}
 \end{aligned}$$

where (a) follows from (B.1) and (9). In (b), we use that  $\mathbb{E}\{\tilde{G}_{\mathbb{H}}(\tau, \nu)\} = 0$ , and we implicitly assume that the prototype functions  $g(t)$  and  $\gamma(t)$  have a compact support and that the channel average component  $\bar{h}_{\mathbb{H}}(\tau, t)$  is approximately constant (in  $t$ ) over that support. If we consider rectangular prototype functions, the duration of their support is upper-bounded by  $T$ , which represents a few tens or hundreds of milliseconds. This has to be compared with the fluctuation period of  $\bar{h}_{\mathbb{H}}(\tau, t)$ , which is rather a few tens or hundreds of seconds [2]. Note that, theoretically, some prototype functions can have an infinite support. However, the contribution to the received power from the part of the pulse that has a support greater than few times the symbol period  $T$  is rather negligible (e.g., for most infinite-length prototype functions such as Gaussian, Raised-Cosine, etc., we usually have that  $\int_{-5T}^{5T} |g(t)|^2 dt \approx \int_{-\infty}^{\infty} |g(t)|^2 dt$ ). (d) holds because, according to (4), the zero-mean random part  $\tilde{h}_{\mathbb{H}}(\tau, t)$  of the channel is wide-sense stationary so that  $\mathbb{E}\{\tilde{G}_{\mathbb{H}}(\tau, \nu) \tilde{G}_{\mathbb{H}}^*(\tau', \nu')\} = \tilde{S}_{\mathbb{H}}(\tau, \tau', \nu) \delta(\nu' - \nu)$ , where  $\tilde{S}_{\mathbb{H}}(\tau, \tau', \nu)$  is the channel scattering function defined in (29). Note that in the case where the scatterers are assumed to be uncorrelated  $\mathbb{E}\{\tilde{G}_{\mathbb{H}}(\tau, \nu) \tilde{G}_{\mathbb{H}}^*(\tau', \nu')\} = \tilde{S}_{\mathbb{H}}(\tau, \nu) \delta(\nu' - \nu) \delta(\tau' - \tau)$ , so that (B.2) simplifies to

$$\begin{aligned}
 &\mathbb{E} \left\{ \left| \left[ \mathbf{H}^{(k,k)} \right]_{n,n} \right|^2 \right\} \\
 &\approx \int_\tau \int_\nu \tilde{S}_{\mathbb{H}}(\tau, \nu) |A_{\gamma,g}(\tau, \nu)|^2 d\nu d\tau \\
 &\quad + \left| \int_\tau \bar{h}_{\mathbb{H}}(\tau, kT) A_{\gamma,g}^*(\tau, 0) e^{-j2\pi n F \tau} d\tau \right|^2. \tag{B.3}
 \end{aligned}$$

Similarly to (B.2), the interference power can be derived from the following development:

$$\begin{aligned}
& \mathbb{E} \left\{ \left| \left[ \mathbf{H}^{(k,k')} \right]_{n,n'} \right|^2 \right\} \\
& \stackrel{(a)}{=} \mathbb{E} \left\{ \left| \int_{\tau} \int_{\nu} \left( \bar{G}_{\text{H}}(\tau, \nu) + \tilde{G}_{\text{H}}(\tau, \nu) \right) \right. \right. \\
& \quad \times A_{\gamma,g}^*(\tau + (k' - k)T, \nu + (n' - n)F) \\
& \quad \left. \left. \times e^{-j2\pi n' F \tau} e^{j2\pi(\nu + (n' - n)F)kT} d\nu d\tau \right|^2 \right\} \\
& \stackrel{(b)}{\approx} \mathbb{E} \left\{ \left| \int_{\tau} \int_{\nu} \tilde{G}_{\text{H}}(\tau, \nu) A_{\gamma,g}^*(\tau + (k' - k)T, \nu + (n' - n)F) \right. \right. \\
& \quad \left. \left. \times e^{-j2\pi n' F \tau} e^{j2\pi(\nu + (n' - n)F)kT} d\nu d\tau \right|^2 \right\} \\
& + \left| \int_{\tau} \bar{h}_{\text{H}}(\tau, k'T) \right. \\
& \quad \left. \times A_{\gamma,g}^*(\tau + (k' - k)T, (n' - n)F) e^{-j2\pi n' F \tau} d\tau \right|^2 \\
& \stackrel{(c)}{=} \int_{\tau} \int_{\tau'} \int_{\nu} \tilde{S}_{\text{H}}(\tau, \tau', \nu) \\
& \quad \times A_{\gamma,g}^*(\tau + (k' - k)T, \nu + (n' - n)F) \\
& \quad \times A_{\gamma,g}(\tau' + (k' - k)T, \nu + (n' - n)F) \\
& \quad \times e^{j2\pi n' F(\tau' - \tau)} d\nu d\tau' d\tau \\
& + \left| \int_{\tau} \bar{h}_{\text{H}}(\tau, k'T) \right. \\
& \quad \left. \times A_{\gamma,g}^*(\tau + (k' - k)T, (n' - n)F) e^{-j2\pi n' F \tau} d\tau \right|^2, \tag{B.4}
\end{aligned}$$

where (a) follows from (B.1) and (9). For (B.2) and (B.4) alike, in (b) we assume that  $\bar{h}_{\text{H}}(\tau, t)$  is approximately constant over some period of time. We here consider that  $\bar{h}_{\text{H}}(\tau, t)$  does not fluctuate much over the duration that corresponds to the maximal time difference between two interfering OFDM symbols, that is,  $\bar{h}_{\text{H}}(\tau, kT) \approx \bar{h}_{\text{H}}(\tau, k'T)$ ,  $\forall (k, k') \in \{(k, k') | \mathbb{E}\{|\left[ \mathbf{H}^{(k,k')} \right]_{n,n'}|^2\} \neq 0\}$ . Once again, this assumption is not restricting since for most OFDM systems the duration  $(k' - k)T$  only represents a few tens or hundreds of milliseconds in worst-case scenarios. In the case where the scatterers are assumed to be uncorrelated, (B.4) simplifies to

$$\begin{aligned}
& \mathbb{E} \left\{ \left| \left[ \mathbf{H}^{(k,k')} \right]_{n,n'} \right|^2 \right\} \\
& = \int_{\tau} \int_{\nu} \tilde{S}_{\text{H}}(\tau, \nu) \\
& \quad \times \left| A_{\gamma,g}(\tau + (k' - k)T, \nu + (n' - n)F) \right|^2 d\nu d\tau
\end{aligned}$$

$$\begin{aligned}
& + \left| \int_{\tau} \bar{h}_{\text{H}}(\tau, k'T) \right. \\
& \quad \left. \times A_{\gamma,g}^*(\tau + (k' - k)T, (n' - n)F) e^{-j2\pi n' F \tau} d\tau \right|^2. \tag{B.5}
\end{aligned}$$

### C. Proof of Theorem 1

A lower bound on  $C$  can be obtained by evaluating the mutual information  $I(\mathbf{y}; \mathbf{x})$  for a specific input distribution. Specifically,  $\mathbf{x}$  is chosen such that  $\mathbf{x} \sim \mathcal{C}\mathcal{N}(0, (PT/N)\mathbf{I})$ . The proof of Theorem 1 next relies on the following information theoretic inequality [29, 33]:

$$I(\mathbf{y}; \mathbf{x}) \geq I(\mathbf{y}; \mathbf{x} | \mathbf{H}) - I(\mathbf{y}; \mathbf{H} | \mathbf{x}). \tag{C.1}$$

*C.1. Computation of  $I(\mathbf{y}; \mathbf{x} | H)$ .* The computation of  $I(\mathbf{y}; \mathbf{x} | \mathbf{H}) = h_E(\mathbf{y} | \mathbf{H}) - h_E(\mathbf{y} | \mathbf{x}, \mathbf{H})$  is straightforward since

(i) conditional on  $\mathbf{H}$ ,  $\mathbf{y}$  is distributed according to a complex Gaussian distribution with a covariance matrix equal to  $(PT/N)\mathbf{H}\mathbf{H}^\dagger + \mathbb{E}\{\mathbf{w}\mathbf{w}^\dagger\}$ ;

(ii) conditional on  $\mathbf{x}$  and  $\mathbf{H}$ ,  $\mathbf{y}$  is complex Gaussian with a covariance matrix equal to  $\mathbb{E}\{\mathbf{w}\mathbf{w}^\dagger\}$ .

The entries of the  $NK \times NK$  noise covariance matrix  $\mathbb{E}\{\mathbf{w}\mathbf{w}^\dagger\}$  are given by

$$\begin{aligned}
& \left[ \mathbb{E}\{\mathbf{w}\mathbf{w}^\dagger\}^{(k,k')} \right]_{n,n'} \triangleq \mathbb{E}\{w_{k,n} w_{k',n'}^*\} \\
& = \int_{\tau} R_w(\tau) e^{-j2\pi n F \tau} \\
& \quad \times A_{\gamma,y}^*(\tau + (k' - k)T, (n' - n)F) \\
& \quad \times e^{j2\pi k T F (n' - n)} d\tau \\
& \stackrel{(a)}{\approx} \int_{\tau} R_w(\tau) e^{-j2\pi n F \tau} \\
& \quad \times A_{\gamma,y}^*((k' - k)T, (n' - n)F) \\
& \quad \times e^{j2\pi k T F (n' - n)} d\tau \\
& \stackrel{(b)}{=} \int_{\tau} R_w(\tau) e^{-j2\pi n F \tau} d\tau \\
& \quad \times \delta(k - k') \delta(n - n') \\
& \stackrel{(c)}{=} W(nF) \times \delta(k - k') \delta(n - n'). \tag{C.2}
\end{aligned}$$

Here, (a) is based on Appendix A where it is shown that  $R_w(\tau)$  can be well approximated by a function that decays

very fast compared to common pulse durations (i.e.,  $R_w(\tau) = \beta e^{-5.10^3|\tau|} e^{-j2\pi f_c \tau}$ ). (b) follows from the orthogonality of the receive pulse and (c) from (8). Consequently,

$$\begin{aligned} I(\mathbf{y}; \mathbf{x} | \mathbf{H}) &= \mathbb{E}_{\mathbf{H}} \left\{ \log \det \left( \mathbf{I} + \frac{PT}{N} \mathbf{H} \mathbf{H}^\dagger \mathbb{E} \{ \mathbf{w} \mathbf{w}^\dagger \}^{-1} \right) \right\} \\ &= \mathbb{E}_{\mathbf{H}} \left\{ \log \det \left( \mathbf{I} + \frac{PT}{N} \mathbf{H} \mathbf{H}^\dagger \text{diag}(\mathbf{r}_w)^{-1} \right) \right\}, \end{aligned} \quad (\text{C.3})$$

where the entries of the  $NK \times 1$  vector  $\mathbf{r}_w$  are defined as

$$r_w(n+kK) \triangleq W(nF), \quad n \in [0, N-1], \quad k \in [0, K-1]. \quad (\text{C.4})$$

*C.2. Computation of  $I(\mathbf{y}; \mathbf{H} | \mathbf{x})$ .* The offdiagonal elements of  $\mathbf{H}$  being generally nonnull in highly dispersive environments, the derivation of  $I(\mathbf{y}; \mathbf{H} | \mathbf{x})$  is not that easy. Influenced by [21], we next seek an upper bound on the penalty term  $I(\mathbf{y}; \mathbf{H} \mathbf{x})$  by splitting  $\mathbf{y}$  into an interference-free part and an interference-only part, so that

$$\begin{aligned} \mathbf{y} &= \mathbf{H} \mathbf{x} + \mathbf{w} \\ &= \mathbf{h} \odot \mathbf{x} + \mathbf{Z} \mathbf{x} + \mathbf{w} \\ &= \underbrace{\mathbf{h} \odot \mathbf{x} + \mathbf{w}_1}_{\triangleq \mathbf{y}_1} + \underbrace{\mathbf{Z} \mathbf{x} + \mathbf{w}_2}_{\triangleq \mathbf{y}_2}, \end{aligned} \quad (\text{C.5})$$

where  $\mathbf{w}_1$  are two independent random vectors such that  $\mathbf{w}_1 \sim \mathcal{CN}(0, \alpha \times \text{diag}(\mathbf{r}_w))$  and  $\mathbf{w}_2 \sim \mathcal{CN}(0, (1-\alpha) \times \text{diag}(\mathbf{r}_w))$ , with  $0 < \alpha < 1$ .

Let us note that

$$\begin{aligned} I(\mathbf{y}; \mathbf{H} | \mathbf{x}) &\stackrel{(a)}{\leq} I(\mathbf{y}_1, \mathbf{y}_2; \mathbf{H} | \mathbf{x}) \\ &\stackrel{(b)}{\leq} I(\mathbf{y}_1, \mathbf{y}_2; \mathbf{h}, \mathbf{Z} | \mathbf{x}) \\ &\stackrel{(c)}{=} I(\mathbf{y}_1; \mathbf{h}, \mathbf{Z} | \mathbf{x}) + I(\mathbf{y}_2; \mathbf{h}, \mathbf{Z} | \mathbf{x}, \mathbf{y}_1) \\ &\stackrel{(d)}{=} I(\mathbf{y}_1; \mathbf{h} | \mathbf{x}) + I(\mathbf{y}_2; \mathbf{h}, \mathbf{Z} | \mathbf{x}, \mathbf{y}_1) \\ &\stackrel{(e)}{=} I(\mathbf{y}_1; \mathbf{h} | \mathbf{x}) + h_E(\mathbf{y}_2 | \mathbf{x}, \mathbf{y}_1) \\ &\quad - h_E(\mathbf{y}_2 | \mathbf{x}, \mathbf{y}_1, \mathbf{h}, \mathbf{Z}) \\ &\stackrel{(f)}{=} I(\mathbf{y}_1; \mathbf{h} | \mathbf{x}) + h_E(\mathbf{y}_2 | \mathbf{x}, \mathbf{y}_1) \\ &\quad - h_E(\mathbf{y}_2 | \mathbf{x}, \mathbf{Z}) \\ &\stackrel{(g)}{\leq} I(\mathbf{y}_1; \mathbf{h} | \mathbf{x}) + h_E(\mathbf{y}_2 | \mathbf{x}) \\ &\quad - h_E(\mathbf{y}_2 | \mathbf{x}, \mathbf{Z}) \\ &= I(\mathbf{y}_1; \mathbf{h} | \mathbf{x}) + I(\mathbf{y}_2; \mathbf{Z} | \mathbf{x}). \end{aligned} \quad (\text{C.6})$$

In (a) and (b), we used the data processing inequality, (c) follows from the chain rule, (d) holds because  $\mathbf{y}_1$  and  $\mathbf{Z}$  are conditionally independent given  $\mathbf{h}$ , in (e) we expressed

mutual information as a function of entropy, (f) holds because  $\mathbf{y}_2$  and  $\mathbf{y}_1$  are conditionally independent given  $\mathbf{x}$  and  $\mathbf{h}$ , and also because  $\mathbf{y}_2$  and  $\mathbf{h}$  are conditionally independent given  $\mathbf{x}$  and  $\mathbf{Z}$ . Finally, the fact that conditioning reduces entropy leads to (g).

Using that  $\mathbf{y}_1$  is Gaussian given  $\mathbf{h}$  and  $\mathbf{x}$ , and as a consequence of Jensen's inequality,  $I(\mathbf{y}_1; \mathbf{h} | \mathbf{x})$  can be upper-bounded as

$$\begin{aligned} I(\mathbf{y}_1; \mathbf{h} | \mathbf{x}) &= \mathbb{E}_{\mathbf{x}} \left\{ \log \det \left( \mathbf{I} + \frac{\text{diag}(\mathbf{x}) \text{diag}(\mathbf{x}^\dagger)}{\alpha} \mathbf{R}_h \text{diag}(\mathbf{r}_w)^{-1} \right) \right\} \\ &\leq \log \det \left( \mathbf{I} + \frac{PT}{N\alpha} \mathbf{R}_h \text{diag}(\mathbf{r}_w)^{-1} \right), \end{aligned} \quad (\text{C.7})$$

where  $\mathbf{R}_h$  denotes the covariance matrix of the direct channel vector  $\mathbf{h}$ . From (B.1), we can express the entries of  $\mathbf{R}_h$  as

$$\begin{aligned} [\mathbf{R}_h^{(k,k')}]_{n,n'} &= \int_{\tau} \int_{\tau'} \int_{\nu} \tilde{S}_{\text{hh}}(\tau, \tau', \nu) A_{\gamma_g}^*(\tau, \nu) \\ &\quad \times A_{\gamma_g}(\tau', \nu) e^{j2\pi\nu T(k-k')} \\ &\quad \times e^{j2\pi F(n'\tau' - n\tau)} d\nu d\tau' d\tau. \end{aligned} \quad (\text{C.8})$$

We next seek an upper bound on  $I(\mathbf{y}_2; \mathbf{Z} | \mathbf{x})$ . Let  $\mathbf{Q}(\mathbf{x}) = \mathbb{E}_{\mathbf{Z}} \{ (\mathbf{Z} \mathbf{x} - \mathbb{E}_{\mathbf{Z}} \{ \mathbf{Z} \mathbf{x} \}) (\mathbf{Z} \mathbf{x} - \mathbb{E}_{\mathbf{Z}} \{ \mathbf{Z} \mathbf{x} \})^\dagger \}$  be the conditional covariance matrix of the vector  $\mathbf{Z} \mathbf{x}$  given  $\mathbf{x}$ .  $\mathbf{Z} \mathbf{x}$  being Gaussian given  $\mathbf{x}$ , using Hadamard's and Jensen's inequalities,  $I(\mathbf{y}_2; \mathbf{Z} | \mathbf{x})$  is then upper-bounded as follows:

$$\begin{aligned} I(\mathbf{y}_2; \mathbf{Z} | \mathbf{x}) &= \mathbb{E}_{\mathbf{x}} \left\{ \log \det \left( \mathbf{I} + \frac{1}{1-\alpha} \mathbf{Q}(\mathbf{x}) \text{diag}(\mathbf{r}_w)^{-1} \right) \right\} \\ &\leq \sum_{k=0}^{K-1} \sum_{n=0}^{N-1} \mathbb{E}_{\mathbf{x}} \left\{ \log \left( 1 + \frac{1}{(1-\alpha)r_w(n+kK)} [\mathbf{Q}(\mathbf{x})^{(k,k)}]_{n,n} \right) \right\} \\ &\leq \sum_{k=0}^{K-1} \sum_{n=0}^{N-1} \log \left( 1 + \frac{1}{(1-\alpha)r_w(n+kK)} \mathbb{E}_{\mathbf{x}} \left\{ [\mathbf{Q}(\mathbf{x})^{(k,k)}]_{n,n} \right\} \right) \\ &= \sum_{k=0}^{K-1} \sum_{n=0}^{N-1} \log \left( 1 + \frac{PT}{N(1-\alpha)r_w(n+kK)} \tilde{\sigma}_{I_n}^2 \right), \end{aligned} \quad (\text{C.9})$$

where the last equality holds because the input symbols are i.i.d. with zero mean, so that

$$\begin{aligned} &\mathbb{E}_{\mathbf{x}} \left\{ [\mathbf{Q}(\mathbf{x})^{(k,k)}]_{n,n} \right\} \\ &= \frac{PT}{N} \left[ \mathbb{E} \left\{ (\mathbf{Z} - \mathbb{E} \{ \mathbf{Z} \}) (\mathbf{Z} - \mathbb{E} \{ \mathbf{Z} \})^\dagger \right\}^{(k,k)} \right]_{n,n} \\ &= \frac{PT}{N} \tilde{\sigma}_{I_n}^2, \end{aligned} \quad (\text{C.10})$$

with  $\tilde{\sigma}_{I_n}^2$  the interference power due to the random part of the channel as defined in (31). Equation (C.9) can be further

simplified by noticing that  $r_w(n+kK)$  and  $\tilde{\sigma}_{I_n}^2$  do not depend on  $k$ ; therefore,

$$I(\mathbf{y}_2; \mathbf{Z} | \mathbf{x}) \leq K \sum_{n=0}^{N-1} \log \left( 1 + \frac{PT}{N(1-\alpha)r_w(n)} \tilde{\sigma}_{I_n}^2 \right). \quad (\text{C.11})$$

From (C.1), (C.3), (C.7), and (C.11), and for all  $0 < \alpha < 1$ ,  $I(\mathbf{y}; \mathbf{x})$  can be lower-bounded as follows:

$$\begin{aligned} I(\mathbf{y}; \mathbf{x}) &\geq \mathbb{E}_{\mathbf{H}} \left\{ \log \det \left( \mathbf{I} + \frac{PT}{N} \mathbf{H} \mathbf{H}^\dagger \text{diag}(\mathbf{r}_w)^{-1} \right) \right\} \\ &\quad - \left[ \log \det \left( \mathbf{I} + \frac{PT}{N\alpha} \mathbf{R}_h \text{diag}(\mathbf{r}_w)^{-1} \right) \right. \\ &\quad \left. + K \sum_{n=0}^{N-1} \log \left( 1 + \frac{PT}{N(1-\alpha)r_w(n)} \tilde{\sigma}_{I_n}^2 \right) \right]. \end{aligned} \quad (\text{C.12})$$

The bound is then tightened by choosing  $\alpha$  that minimizes the penalty term, which concludes the proof.

## D. Proof of Corollary 2

*D.1. White Noise Assumption.* Under the white noise assumption, the noise PSD is flat over the entire bandwidth so that  $W(f) = W_0$ , where  $W_0$  is a constant. In that case, the entries of vector  $\mathbf{r}_w$  are all equal to  $W_0$ , and the SNR  $\rho$  satisfies  $\rho = P/(BW_0)$ . Given that  $B = NF$ , from Theorem 1 we have

$$\begin{aligned} C &\geq \lim_{K \rightarrow \infty} \frac{1}{KT} \mathbb{E}_{\mathbf{H}} \left\{ \log \det \left( \mathbf{I} + \rho TF \mathbf{H} \mathbf{H}^\dagger \right) \right\} \\ &\quad - \inf_{0 < \alpha < 1} \frac{1}{KT} \left[ \log \det \left( \mathbf{I} + \frac{\rho TF}{\alpha} \mathbf{R}_h \right) \right. \\ &\quad \left. + K \sum_{n=0}^{N-1} \log \left( 1 + \frac{\rho TF}{1-\alpha} \tilde{\sigma}_{I_n}^2 \right) \right]. \end{aligned} \quad (\text{D.1})$$

*D.2. Uncorrelated Scattering Assumption.* In the case where the scatterers can be assumed as uncorrelated, the lower bound on the information rate can be further simplified.

First, the channel scattering function is reduced from three to two dimensions so that  $\tilde{\sigma}_{I_n}^2$  does not depend on  $n$  anymore and is expressed as

$$\begin{aligned} \tilde{\sigma}_{I_n}^2 &= \sum_{\substack{k'=1-K \\ (k',n') \neq (0,0)}}^{K-1} \sum_{n'=1-N}^{N-1} \int_{\tau} \int_{\nu} \tilde{\mathfrak{S}}_{\mathbb{H}}(\tau, \nu) \\ &\quad \times \left| A_{\gamma, g}^*(\tau + k'T, \nu + n'F) \right|^2 d\nu d\tau \\ &\triangleq \tilde{\sigma}_I^2. \end{aligned} \quad (\text{D.2})$$

Second, the covariance matrix  $\mathbf{R}_h$  becoming block-Toeplitz, the extension of Szegő's theorem to two-level Toeplitz matrices can be applied, that is [34, Th. 3]:

$$\begin{aligned} \lim_{K \rightarrow \infty} \frac{1}{KT} \log \det \left( \mathbf{I} + \frac{\rho TF}{\alpha} \mathbf{R}_h \right) \\ = \frac{1}{T} \int_{-1/2}^{1/2} \log \det \left( \mathbf{I} + \frac{\rho TF}{\alpha} \tilde{\mathfrak{S}}(\theta) \right) d\theta, \end{aligned} \quad (\text{D.3})$$

where  $\tilde{\mathfrak{S}}(\theta)$  is the power spectral density of the zero-mean multivariate random process  $\{\mathbf{h}_k - \mathbb{E}\{\mathbf{h}_k\}\}$ , with  $\mathbf{h}_k \triangleq [h_{k,0} \ h_{k,1} \ \dots \ h_{k,N-1}]^T$ , that is,

$$\tilde{\mathfrak{S}}(\theta) \triangleq \sum_{k=-\infty}^{\infty} \mathbb{E} \left\{ (\mathbf{h}_k - \mathbb{E}\{\mathbf{h}_k\})(\mathbf{h}_k - \mathbb{E}\{\mathbf{h}_k\})^\dagger \right\} e^{-j2\pi k\theta}. \quad (\text{D.4})$$

By noticing that the entries on the main diagonal of  $\tilde{\mathfrak{S}}(\theta)$  are all equal and by applying Hadamard's inequality, we have

$$\begin{aligned} \frac{1}{T} \int_{-1/2}^{1/2} \log \det \left( \mathbf{I} + \frac{\rho TF}{\alpha} \tilde{\mathfrak{S}}(\theta) \right) d\theta \\ \leq \frac{N}{T} \int_{-1/2}^{1/2} \log \left( 1 + \frac{\rho TF}{\alpha} \tilde{s}(\theta) \right) d\theta, \end{aligned} \quad (\text{D.5})$$

where  $\tilde{s}(\theta)$  is the PSD of the zero-mean stationary channel process  $\{h_{k,n} - \mathbb{E}\{h_{k,n}\}\}_k$  and is expressed as

$$\tilde{s}(\theta) = \sum_{k=-\infty}^{\infty} \int_{\tau} \int_{\nu} \tilde{\mathfrak{S}}_{\mathbb{H}}(\tau, \nu) \left| A_{\gamma, g}(\tau, \nu) \right|^2 e^{j2\pi \nu k T} d\nu d\tau e^{-j2\pi k\theta}. \quad (\text{D.6})$$

Corollary 2 is then obtained by noticing that  $N/T = B/(TF)$ .

## Acknowledgments

The authors are grateful to the DGA-TN for providing part of the experimental data used in this paper. This work was supported in part by the ONR MURI Grant N00014-07-1-0738, the ONR Grant N00014-10-1-0576, and the Grant NSF 0831728.

## References

- [1] P. van Walree, "Channel sounding for acoustic communications: techniques and shallow-water examples," Research Report, Norwegian Defence Research Establishment (FFI), Kjeller, Norway, 2011.
- [2] F.-X. Socheleau, C. Laot, and J.-M. Passerieux, "Stochastic replay of non-WSSUS underwater acoustic communication channels recorded at sea," *IEEE Transactions on Signal Processing*, vol. 59, no. 10, pp. 4838–4849, 2011.
- [3] M. Stojanovic and J. Preisig, "Underwater acoustic communication channels: propagation models and statistical characterization," *IEEE Communications Magazine*, vol. 47, no. 1, pp. 84–89, 2009.
- [4] B. Tomasi, J. Preisig, G. B. Deane, and M. Zorzi, "A study on the wide-sense stationarity of the underwater acoustic channel for non-coherent communication systems," in *Proceedings of the 11th European Wireless Conference, Sustainable Wireless Technologies (European Wireless)*, pp. 1–6, April 2011.

- [5] D. B. Kilfoyle and A. B. Baggeroer, "State of the art in underwater acoustic telemetry," *IEEE Journal of Oceanic Engineering*, vol. 25, no. 1, pp. 4–27, 2000.
- [6] F. Frassati, C. Lafon, P. A. Laurent, and J. M. Passerieux, "Experimental assessment of OFDM and DSSS modulations for use in littoral waters underwater acoustic communications," in *Proceedings of IEEE Oceans'05 Europe Conference & Exhibition*, pp. 826–831, Brest, France, June 2005.
- [7] B. Li, S. Zhou, M. Stojanovic, L. L. Freitag, and P. Willett, "Multicarrier communication over underwater acoustic channels with nonuniform Doppler shifts," *IEEE Journal of Oceanic Engineering*, vol. 33, no. 2, pp. 198–209, 2008.
- [8] C. R. Berger, S. Zhou, J. C. Preisig, and P. Willett, "Sparse channel estimation for multicarrier underwater acoustic communication: from subspace methods to compressed sensing," *IEEE Transactions on Signal Processing*, vol. 58, no. 3, pp. 1708–1721, 2010.
- [9] G. Leus and P. A. Van Walree, "Multiband OFDM for covert acoustic communications," *IEEE Journal on Selected Areas in Communications*, vol. 26, no. 9, Article ID 4686805, pp. 1662–1673, 2008.
- [10] P. Jung and G. Wunder, "The WSSUS pulse design problem in multicarrier transmission," *IEEE Transactions on Communications*, vol. 55, no. 10, pp. 1918–1928, 2007.
- [11] G. Matz, D. Schafhuber, K. Gröchenig, M. Hartmann, and F. Hlawatsch, "Analysis, optimization, and implementation of low-interference wireless multicarrier systems," *IEEE Transactions on Wireless Communications*, vol. 6, no. 5, pp. 1921–1930, 2007.
- [12] A. Barbieri, G. Caire, and U. Mitra, "Transmit/receive filter optimization for doubly-selective underwater acoustic channels," in *Proceedings of the IEEE OCEANS' 2008*, pp. 1–6, September 2008.
- [13] W. Kozek and A. F. Molisch, "Nonorthogonal pulseshapes for multicarrier communications in doubly dispersive channels," *IEEE Journal on Selected Areas in Communications*, vol. 16, no. 8, pp. 1579–1589, 1998.
- [14] R. Haas and J. C. Belfiore, "A Time-Frequency Well-localized Pulse for Multiple Carrier Transmission," *Wireless Personal Communications*, vol. 5, no. 1, pp. 1–18, 1997.
- [15] K. Liu, T. Kadous, and A. M. Sayeed, "Orthogonal time-frequency signaling over doubly dispersive channels," *IEEE Transactions on Information Theory*, vol. 50, no. 11, pp. 2583–2603, 2004.
- [16] P. A. Bello, "Characterization of randomly time-variant linear channels," *IEEE Transactions on Communications Systems*, vol. 11, no. 4, pp. 360–393, 1963.
- [17] C. Polprasert, J. A. Ritcey, and M. Stojanovic, "Capacity of OFDM systems over fading underwater acoustic channels," *IEEE Journal of Oceanic Engineering*, vol. 36, no. 4, pp. 514–524, 2011.
- [18] M. C. Gursoy, H. V. Poor, and S. Verdú, "The noncoherent Rician fading channel part I: structure of the capacity-achieving input," *IEEE Transactions on Wireless Communications*, vol. 4, no. 5, pp. 2193–2206, 2005.
- [19] V. Sethuraman, L. Wang, B. Hajek, and A. Lapidath, "Low-SNR capacity of noncoherent fading channels," *IEEE Transactions on Information Theory*, vol. 55, no. 4, pp. 1555–1574, 2009.
- [20] G. Durisi, U. G. Schuster, H. Bölcskei, and S. Shamai, "Noncoherent capacity of underspread fading channels," *IEEE Transactions on Information Theory*, vol. 56, no. 1, Article ID 5361496, pp. 367–395, 2010.
- [21] G. Durisi, V. I. Morgenshtern, and H. Bölcskei, "Sensitivity of continuous-time noncoherent fading channel capacity," *IEEE Transactions on Information Theory*. In press.
- [22] P. Qarabaqi and M. Stojanovic, "Statistical modeling of a shallow water acoustic communication channel," in *Proceedings of the Underwater Acoustic Measurements: Technologies and Results Conference*, p. 13411350, Nafplion, Greece, June 2009.
- [23] F. D. Neeser and J. L. Massey, "Proper complex random processes with applications to information theory," *IEEE Transactions on Information Theory*, vol. 39, no. 4, pp. 1293–1303, 1993.
- [24] M. Stojanovic, "On the relationship between capacity and distance in an underwater acoustic communication channel," *ACM SIGMOBILE Mobile Computing and Communications Review (MC2R)*, vol. 11, no. 4, pp. 43–64, 2007.
- [25] O. Christensen, *An Introduction to Frames and Riesz Bases*, Birkhuser, Boston, Mass, USA, 2003.
- [26] F. Hlawatsch and G. Matz, *Wireless Communications Over Rapidly Time-Varying Channels*, Elsevier, New York, NY, USA, 2011.
- [27] S.-J. Hwang and P. Schniter, "Efficient multicarrier communication for highly spread underwater acoustic channels," *IEEE Journal on Selected Areas in Communications*, vol. 26, no. 9, Article ID 4686806, pp. 1674–1683, 2008.
- [28] D. Schafhuber, H. Bölcskei, and G. Matz, "System capacity of wideband OFDM communications over fading channels without channel knowledge," in *Proceedings of the IEEE International Symposium on Information Theory (ISIT '04)*, July 2004.
- [29] X. Deng and A. M. Haimovich, "Achievable rates over time-varying rayleigh fading channels," *IEEE Transactions on Communications*, vol. 55, no. 7, pp. 1397–1406, 2007.
- [30] W. Kozek, *Matched weyl-heisenberg expansions of nonstationary environments [Ph.D. thesis]*, Department of Electrical Engineering, Vienna University of Technology, Vienna, Austria, 1997.
- [31] J.-M. Passerieux, F.-X. Socheleau, and C. Laot, "On the capacity of the underwater acoustic communication channel under realistic assumptions," in *Proceedings of the IEEE European Wireless*, pp. 1–6, April 2011.
- [32] G. Campbell and R. Foster, *Fourier Integrals for Practical Applications*, D Van Nostrand Company Inc, New York, NY, USA, 1948.
- [33] V. Sethuraman and B. Hajek, "Capacity per unit energy of fading channels with a peak constraint," *IEEE Transactions on Information Theory*, vol. 51, no. 9, pp. 3102–3120, 2005.
- [34] H. Gazzah, P. A. Regalia, and J. P. Delmas, "Asymptotic eigenvalue distribution of block toeplitz matrices and application to blind SIMO channel identification," *IEEE Transactions on Information Theory*, vol. 47, no. 3, pp. 1243–1251, 2001.

## Research Article

# Compensation of Linear Multiscale Doppler for OFDM-Based Underwater Acoustic Communication Systems

**A. E. Abdelkareem, B. S. Sharif, C. C. Tsimenidis, and J. A. Neasham**

*School of Electrical and Electronic Engineering, Newcastle University, Newcastle upon Tyne NE1 7RU, UK*

Correspondence should be addressed to A. E. Abdelkareem, a.e.abdelkareem@ncl.ac.uk

Received 21 February 2012; Accepted 21 May 2012

Academic Editor: Yuriy Zakharov

Copyright © 2012 A. E. Abdelkareem et al. This is an open access article distributed under the Creative Commons Attribution License, which permits unrestricted use, distribution, and reproduction in any medium, provided the original work is properly cited.

In particular cases, such as acceleration, it is required to design a receiver structure that is capable of accomplishing time varying Doppler compensation. In this paper, two approaches are taken into consideration in order to estimate the symbol timing offset parameter. The first method employed to achieve an estimate of this particular parameter is based upon centroid localization and this prediction is reinforced by a second technique which utilises linear prediction, based on the assumption that the speed changes linearly during the OFDM symbol time. Subsequently, the two estimations of the symbol timing offset parameter are smoothed in order to obtain a fine tuned approximation of the Doppler scale. Additionally, the effects of weighting coefficients on smoothing the Doppler scale and on the performance of the receiver are also investigated. The proposed receiver is investigated, incorporating an improvement that includes fine tuning of the coarse timing synchronization in order to accommodate the time-varying Doppler. Based on this fine-tuned timing synchronization, an extension to the improved receiver is presented to assess the performance of two point correlations. The proposed algorithms' performances were investigated using real data obtained from an experiment that took place in the North Sea in 2009.

## 1. Introduction

Several time-domain receivers that adopt coherent modulation with an emphasis on channel equalization in order to increase communication reliability have been suggested. However, the time-varying doubly-spread characteristic of the underwater acoustic (UWA) channel requires a highly complex equalizer. Recently, an alternative low-complexity, high-speed multicarrier communication system, in the form of OFDM, has attracted considerable interest in the field of underwater acoustic communication (UWAC). This is mainly due to its simplicity of operation by means of the fast Fourier transform (FFT) for the purpose of modulation/demodulation. This system deals with the frequency selectivity of the channel by dividing the broadband data into parallel narrowband channels. Additionally, in a delay-dispersive environment, adopting a CP of a length greater than the maximum delay spread provides an excellent way to assure the orthogonality of the carriers. However, propagation is considered to be time selective due to the

Doppler shift in which one subcarrier may introduce ICI to the adjacent subcarriers [1]. The Doppler shift sensitivity is inversely proportional to the OFDM symbol duration; therefore, even slightly moving platforms can cause serious impairments as far as synchronization is concerned.

Previous studies in the field of UWAC have addressed several approaches for synchronization in the presence of Doppler distortion. For single carrier transmission, a block-based approach [2] has been used to estimate and compensate the Doppler shift. In this approach, two LFM's are used for a coarse estimation of the time scaling factor and then an equalizer is employed for residual Doppler-shift compensation. This method is particularly well suited for constant speed. An alternative approach utilizes an adaptive Doppler compensation technique, as suggested by [3], in order to accommodate autonomous vehicles (AV). This closed-loop Doppler correction method demands a high degree of complexity when it is applied to OFDM systems because there is a requirement for the demodulation of each interpolation factor.

As far as multicarrier transmission is concerned, the authors in [4] employed the principle in [2] and null subcarriers for the purpose of resampling factor estimation and residual Doppler compensation, respectively. Although these algorithms do attain precise estimation by adopting preamble and postamble, the bandwidth utilization factor is compromised. A point estimate of the Doppler shift is adopted in [5]; therefore, it is suitable for situations where the Doppler shift stays constant or varies slowly during the packet time. The concept in [6] was extended to work in UWAC by [7] with an iterative cyclic prefix correlation. To estimate the Doppler shift, the author employed the symmetry of the guard interval with its replica. This parameter is estimated iteratively, depending on the peak location and its phase with respect to the new sampling interval; therefore it is a computationally expensive search. In [8], the authors deal with the different Doppler distortion in the multiple-input multiple-output (MIMO) OFDM by adopting multiple resampling followed by FFT.

Although resampling the signal removes the Doppler shift, a major problem with its residual or carrier frequency offset (CFO) is the destruction of the orthogonality of the subcarriers due to the resulting ICI. A considerable amount of literature on combating ICI has been published. These studies [1, 9–11] have presented conclusions that mitigating ICI will result in successful communication.

All the aforementioned papers assume that the Doppler shift is constant during the symbol period and all paths have equal Doppler shift; therefore, resampling the signal with a unique time scaling factor is valid and a symbol by symbol approach works effectively. A recent study by [12] has highlighted the need to estimate the optimal time scaling factor in a multipath channel of different Doppler shift in each path. However, in our proposed method, it is assumed that the channel variation is mainly caused by the motion of both transmitter and receiver, leading to a significant time-varying Doppler shift. Consequently, this will create acceleration that may exceed  $1 \text{ m/s}^2$  due to speed alterations; therefore, ignoring this effect yields a significant ICI. In this paper, the acceleration is considered and the Doppler shift is assumed to be changing linearly during the symbol time, but the same for all paths. This variation is dealt with by measuring the time expansion/compression frequently within a fraction of a sample period and then compensating the Doppler by means of an efficient 4th order Lagrange interpolation.

In this paper, an algorithm which combines the centroid-based localization and linear equation in estimating the time-varying Doppler shift is proposed. Furthermore, this paper introduces two improvements in order to increase the confidence of the Doppler shift estimation and consequently a low bit error rate (BER) is obtained. These improvements include:

- (1) fine tune the coarse timing estimation; then,
- (2) combining two correlation lags and fine tuning using the weighting coefficients [13]. The first lag is estimated based on the centroid localization [14], and the second lag is estimated based on the correlation of the cyclic prefix (CP) with its replica.

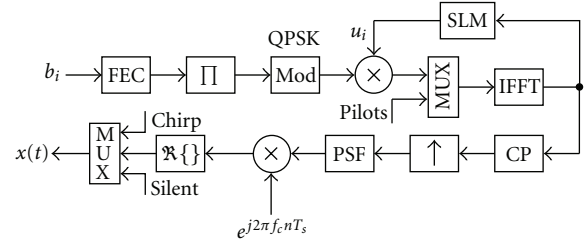


FIGURE 1: Proposed transmitter structure, where the operator  $\Re$  represents the real part of the signal.

Additionally, for the case of low acceleration, these improvements result in a precise estimation of the Doppler shift and no CFO estimation is required.

The rest of this paper is organized as follows. In Section 2, the OFDM system model is introduced. The signal processing in the proposed receiver is presented in Section 3. In Section 4, Doppler extraction and channel estimation are demonstrated. In Section 5, the performance of the proposed algorithms are presented by means of experimental results. Finally, Section 6 draws the conclusions.

## 2. System and Channel Model

The proposed system contains the transmitter depicted in Figure 1. At each instant  $i$ , the encoder receives a vector of information bits  $b_i$  of length  $K_d$  at its input to produce a binary code of length  $K_c = K_d/R_c$  encoded bits, where  $R_c \in (0, 1]$  is the coding rate of the nonsystematic convolutional (NSC) code. The coded bits are permuted by a random interleaver, then converted, in groups of  $m$  successive bits, into alphabet symbols of constellation size  $M = 2^m$ . This mapping operation generates a sequence of  $N_d = K_c/m$ :  $\mathbf{s} = \{s_0, \dots, s_{N_d-1}\}$ , where  $s_i \in \mathbb{C}$  and  $\mathbb{C}$  denotes the set of complex symbols. Subsequently, in the OFDM symbol to be constructed, pilot symbols of phase shift keying (PSK) with unit amplitude are embedded with the data symbols in a comb method, where all pilots and data are transmitted simultaneously on all symbols. These pilot symbols are used for the purpose of estimating channel response at the receiver. A peak-to-average power reduction (PAPR) is introduced using the selective mapping (SLM) technique [15]. To implement this technique, a sequence of phases  $\mathbf{U}$  is added in the transmitted signal to be multiplied by the input data sequences, and the symbol sequence of minimum PAPR is selected for transmission. The resulting OFDM symbol, containing  $N_p$  pilots and  $N_d$  data-bearing subcarriers, where  $N_d \cup N_p = N_c$ , is then modulated by an IFFT of size  $N_c$ , and the last samples are copied and prepended to the symbol to form the CP-OFDM frame. The guard interval of length  $N_g$  is chosen to be longer than the channel dispersion time in order to minimize the intersymbol interference (ISI). The resulting frame is pulse shaped, using a pulse shape filter (PSF), and then up converted using carrier modulation. Let  $T_d$  denote the OFDM symbol duration and  $T_g$  the guard interval. The total OFDM frame duration is  $T = T_d + T_g$ . Let  $f_n = f_c + n\delta f$ , being the carrier frequency corresponding to each of the subcarriers of the OFDM spectrum, where  $\delta f = 1/T_d$  is

the frequency separation between alternate subcarriers, and  $f_c$  is the carrier frequency, so the bandwidth is  $B = N_c \delta f$ . The time-domain representation of the  $i$ th OFDM symbol is given by

$$x_i(t) = \frac{1}{\sqrt{N_c}} \sum_{n \in \mathcal{L}} d_i(n) u_i^{\text{opt}}(n) e^{j2\pi(n/T_d)(t-T_g-iT)} p_{\text{rc}}(t-iT),$$

$$\text{for } iT \leq t < (i+1)T, \quad (1)$$

where  $d_i(n)$  is the symbol transmitted over the  $n$ th subcarrier,  $\mathbf{U}^{\text{opt}}$  is the optimum phase set  $[u_i(1), u_i(2), \dots, u_i(n)]$  for lower PAPR with  $u_i(n) = e^{j\varphi_n}$ ,  $\varphi_n \in [0, 2\pi]$ ,  $\mathcal{L}$  denotes the set of modulated subcarriers, and  $p_{\text{rc}}(t-iT)$  is the pulse shaping filter, which is realized as an up-sampled raised cosine FIR filter. An equivalent passband model of (1) is

$$x(t) = \Re \left\{ e^{j2\pi f_c t} \sum_{i=0}^{\infty} \frac{1}{\sqrt{N_c}} \right. \\ \left. \times \sum_{n \in \mathcal{L}} d_i(n) u_i^{\text{opt}}(n) e^{j2\pi(n/T_d)(t-T_g-iT)} p_{\text{rc}}(t-iT) \right\}$$

$$= \Re \left\{ \sum_{i=0}^{\infty} \frac{1}{\sqrt{N_c}} \right. \\ \left. \times \sum_{n \in \mathcal{L}} d_i(n) u_i^{\text{opt}}(n) e^{j2\pi f_n(t-T_g-iT)} p_{\text{rc}}(t-iT) \right\}. \quad (2)$$

It is assumed that the signal is transmitted over a multipath fading channel as follows:

$$h(\tau, t) = \sum_{l=0}^{L-1} h_l(t) \delta[\tau - \tau_l(t)], \quad (3)$$

where  $\{h_l(t)\}$  are the path amplitudes,  $\{\tau_l(t)\}$  are the time-varying path delays, and  $L$  is the total number of paths. As in [16], we assume the path delay  $\tau_l$  and the gains  $h_l$  are constant over the frame duration  $T$ . For perfect OFDM synchronization, and providing that the maximum delay spread is within the guard interval, the received passband signal can be written as

$$\tilde{r}(t) = \Re \left\{ \frac{1}{\sqrt{N_c}} \sum_{n \in \mathcal{L}} d_i(n) u_i^{\text{opt}}(n) e^{j2\pi f_n t} \right. \\ \left. \times \sum_{l=0}^{L-1} h_l p_{\text{rc}}(t - \tau_l) e^{-j2\pi f_n \tau_l} \right\} + \tilde{w}_i(t), \quad (4)$$

where  $w_i(t)$  is a white Gaussian noise with variance  $\sigma^2$ .

When the Doppler shift is present, a transmitted signal is received as

$$r(t) = x \left[ \left( 1 \pm \frac{v}{c} \right) t - \tau_l \right], \quad (5)$$

where  $v$  denotes the induced speed due to the mobility of the transmitter and/or receiver, and  $c$  is the acoustic propagation speed of 1500 m/s. The (+) sign indicates an expansion of the signal since the distance is increased and vice versa. It is assumed that all paths have a similar  $\Delta$ ; therefore, the received signal in (4) can be rewritten as

$$\tilde{r}(t) = \Re \left\{ \frac{1}{\sqrt{N_c}} \sum_{n \in \mathcal{L}} d_i(n) u_i^{\text{opt}}(n) e^{j2\pi f_n (1+\Delta)t} \right. \\ \left. \cdot \sum_{l=0}^{L-1} h_l p_{\text{rc}}((1+\Delta)t - \tau_l) e^{-j2\pi f_n \tau_l} \right\} + \tilde{w}_i(t). \quad (6)$$

Based on the assumption that the speed of the motion changes linearly during the  $i$ th OFDM symbol interval  $t \in [iT, T(i+1))$ , the Doppler shift is varied with time. Therefore the constant  $\Delta = v/c$  does not hold to accommodate this variation and it should be replaced by  $\Delta(t)$ . Thus, the time varying Doppler shift can be modelled as

$$\Delta(t) = \frac{v(t)}{c}, \quad (7)$$

where  $v(t)$  represents the speed variation during the symbol time. Therefore, the received passband signal in (6) can be rewritten as

$$\tilde{r}(t) = \Re \left\{ \frac{1}{\sqrt{N_c}} \sum_{n \in \mathcal{L}} d_i(n) u_i^{\text{opt}}(n) e^{j2\pi f_n (1+\Delta(t))t} \right. \\ \left. \cdot \sum_{l=0}^{L-1} h_l p_{\text{rc}}[(1+\Delta(t))t - \tau_l] e^{-j2\pi f_n \tau_l} \right\} + \tilde{w}_i(t), \quad (8)$$

and its corresponding complex baseband signal model can be written as

$$r(t) = \sum_{i=0}^{\infty} \sum_{n \in \mathcal{L}} H_i(n) d_i(n) u_i^{\text{opt}}(n) e^{j2\pi n \delta f t} e^{j2\pi \Delta(t) f_n t} + w_i(t), \quad (9)$$

where  $H_i(n)$  is the channel transfer function of the  $i$ th symbol at  $n$ th subcarrier with a time varying Doppler-shift that can be written as

$$H_i(n) = \sum_{l=0}^{L-1} h_l e^{-j2\pi f_n \tau_l} p_{\text{rc}}[1 + \Delta(t)t - \tau_l]. \quad (10)$$

As referred to in [17], it is obvious in (9) that the effect of the Doppler shift on the received signal is twofold. Firstly, it scales the received OFDM frame duration  $T$  by a factor of  $1 + \Delta(t)$ , yielding sampling frequency errors that result in a symbol timing error [18]. Secondly, there is a time-varying CFO.

**2.1. Sampling Frequency Errors.** In discrete time, the sampled transmitted signal  $x[kT_s]$  in (5) is equivalent to a scaling of the sampling period (interpolation or decimation).

$$\tilde{r}[kT_s] = x[k(1 \mp \Delta(t))T_s - \tau_l], \quad (11)$$

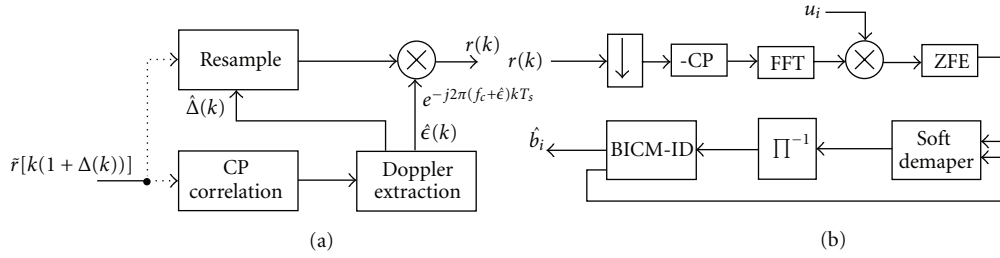


FIGURE 2: Proposed receiver structure.

where  $k$  is an integer, and  $T_s$  and  $\tilde{r}(kT_s)$  are the sampling period and Doppler shifted received sampled signals respectively.

The bidirectional effect of the Doppler shift causes symbol timing errors, which are increased or decreased proportionally to  $\Delta(t)$ . To align the symbol within its period, samples should be removed if  $(\Delta > 0)$  or added if  $(\Delta < 0)$  at regular intervals [19].

Let  $\pm\phi$  be the deviation of samples of the received sequence for each OFDM symbol due to the speed change; the sampling period results in expansion or compression of the samples' length, hence the Doppler-shifted received frame's length is modelled by

$$L'_f = (L_f \mp \phi), \quad (12)$$

where  $L_f = (N_c/B \cdot T_s)$  represents the transmitted passband samples' length. It is apparent that  $L_f$  is only affected by  $T_s$  and any expansion/compression in the timescale will result in  $\phi$ . Therefore, (12) is implicitly equivalent to (11). To remove both CFO and symbol shift, an inverse time scaling of the received (compressed/expanded) signal should be achieved, providing that the amount of Doppler shift  $\Delta(t)$  is known. This is equivalent to changing the sampling rate of the passband signal by  $1 + \Delta(t)$  in discrete-time processing. From (12), it can be inferred that increasing or decreasing the length of samples is equivalent to adjusting the sampling frequency  $f_s$  by the same Doppler shift  $1 + \Delta(t)$ ; thus, (11) is rewritten as

$$\tilde{r}[k] = x \left[ \frac{k(1 \mp \Delta(t))}{f'_s} - \tau_l \right], \quad (13)$$

where  $f'_s = f_s(1 \mp \Delta(t))$ . By substituting  $f'_s$  in (13),  $\tilde{r}[k] = x[k]$ , the signal received is then in conformity with the transmitted signal.

**2.2. Carrier Frequency Offset Errors.** The factor  $e^{j2\pi\Delta(t)f_n t}$  in the received signal in (9) represents a time varying CFO, where  $\Delta(t)f_n = \Delta(t)f_c + \Delta(t)n\delta f$ . The CFO ( $\epsilon$ ) is due to the residual Doppler shift. It is destructive because it deviates the subcarrier spacing  $\delta f$  and introduces ICI, which must be removed prior to the FFT to design an optimum receiver [18]. The resampling process removes the Doppler shift and converts the wideband system into narrowband. However, the residual Doppler shift produced by the fractional part of the time expansion/compression degrades the receiver.

### 3. Signal Processing in the Proposed Receiver

To utilize the available bandwidth efficiently, the algorithm employs a low-complexity blind technique to estimate the Doppler shift based on estimating the coarse timing metric for each OFDM symbol by exploiting the inherent periodicity of the CP. Centroid-based localization has been used to refine the maximum amplitude of the timing metric, that is, the timing offset, as explained in [14]. Using this coarse timing metric, the Doppler shift and its residual are frequently estimated by deriving a tracking step in the Doppler extraction unit (DEU). This unit comprises linear expectation of the timing offset, fine tuning of the estimated parameters, tracking the Doppler shift, and CFO estimation. In this technique, the fractional deviation of the subcarrier spacing, which is the source of ICI, is estimated by exploiting the fractional part of the normalized sampling frequency offset, whereas the integer part of this offset is used to estimate the integer Doppler shift.

**3.1. Coarse Timing Metric Estimation.** The receiver structure of the proposed system is depicted in Figure 2. The received signal  $\tilde{r}(t)$  in (8) is fed through the transducer, preamplifier, and analogue-to-digital converter, and then filtered in the frequency band  $[f_c - B/2, f_c + B/2]$ . The resultant Doppler shifted passband signal  $\tilde{r}[k(1 + \Delta(k))]$  is correlated with the Doppler tolerant training (chirp) to detect the start of the packet  $\zeta$  that contains several OFDM symbols. Based on the existing guard interval, the drift in the received Doppler-shifted signal  $\tilde{r}[k(1 + \Delta(k))]$  is measured by correlating the guard samples ( $N_g \cdot N_s$ ) with an anticipated observation window in order to estimate the coarse timing metric for each OFDM symbol within the packet, as in [14]. In the case of time-varying Doppler shift, that is, multi time scaling factor, the resulting timing metric is affected by the velocity perturbation. Consequently, there is a demand on estimating this timing metric of the same OFDM symbol, but using an alternative approach to increase the accuracy of the Doppler shift estimation. Therefore, in Figure 2(a), linear prediction is adopted to extract the Doppler shift for the purpose of reinforcing the symbol timing offset parameter that was estimated using CP correlation.

**3.2. Time-Varying Doppler Shift Estimation.** Thus far, the timing metric has only been considered for the case of a common Doppler shift during the OFDM symbol time. A worst case scenario may occur when there is a velocity that

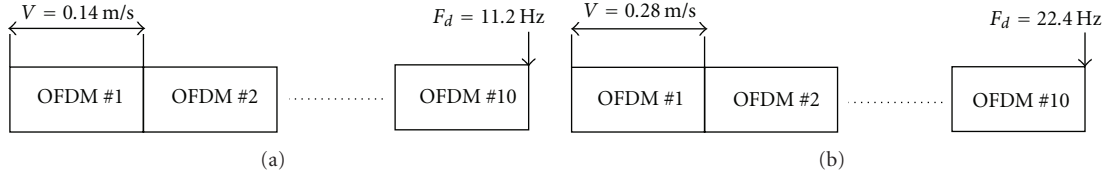


FIGURE 3: Acceleration effect over Doppler frequency change during each symbol time at  $f_c = 12$  kHz. (a)  $\text{Acc} = 0.5 \text{ m/s}^2$ , (b)  $\text{Acc} = 1 \text{ m/s}^2$ .

accelerates or decelerates within the symbol period. This situation can be explained in Figure 3. This figure shows that the start of the OFDM symbol undergoes a different speed relative to the speed at the end of the symbol due to the acceleration, in which the speed is changing linearly with time. As a result, a linear multi Doppler shift during the OFDM symbol period is produced. In addition, the acceleration is a useful indication of how fast the change is, where in Figure 3(a) the Doppler frequency shift is 1.12 Hz at OFDM symbol 1 and it increases to 11.2 at OFDM symbol 10. The same case is demonstrated in Figure 3(b), where the acceleration is  $1 \text{ m/s}^2$  and the Doppler frequency at OFDM symbol 10 is 22.4 Hz, in terms of time-selectivity measurement which is given as

$$T_d F_d > 1. \quad (14)$$

This rapid change within the symbol duration gives an indicator of the amount of distortion caused by the channel on the signal.

Alternatively, frequent estimation of the Doppler shift within the OFDM symbol or reducing the frame length are viable solutions. However, in OFDM signal design, there is a tradeoff between the number of subcarriers, Doppler estimation resolution, and sensitivity to the CFO. Hence, frequent estimation of the interpolation factor is more feasible than shortening the OFDM symbol length.

When the channel has a velocity that accelerates or decelerates in both directions (up or down) within the symbol period, the following example is considered. If  $T_d$  is 256 ms and the maximum acceleration  $1 \text{ m/s}^2$  starting from initial speed  $v_0$ , then the symbol needs approximately  $4T_d$  to attain the maximum speed  $v_0 + 1 \text{ m/s}$ . From this assumption, it can be inferred that the maximum speed change in each OFDM symbol is approximately  $0.25 \text{ m/s}$ .

For a system of 12 kHz carrier frequency, 48 kHz sampling frequency, and a symbol time of 0.256 seconds, such speed variation causes a Doppler frequency shift  $F_d$  to increase by 2 Hz within each symbol up to 20 Hz by symbol number 10. In such circumstances, estimating a common timing metric may not hold to attain acceptable performance. Alternatively, a better solution and more accurate Doppler compensation can be realized by adopting a frequent estimation of the Doppler shift within the OFDM symbol.

#### 4. Doppler Extraction and Channel Estimation

The Doppler extraction unit in Figure 2(a) comprises linear prediction of the symbol timing offset, fine symbol timing

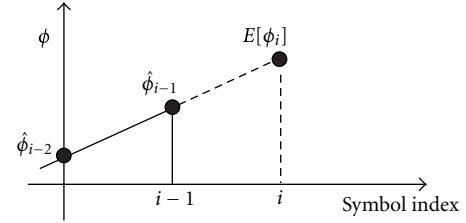


FIGURE 4: Estimation of timing offset during the packet time.

offset, tracking the Doppler shift and CFO or residual Doppler shift estimation.

**4.1. Linear Prediction of the Symbol Timing Offset.** As the transmission structure contains multiple OFDM frames within a packet, the synchronization between these frames is paramount to reduce both the ISI and ICI on the receiver side. In the proposed technique, an improvement is obtained by involving the estimated timing offset at time  $i - 1$  in predicting the timing offset at time  $i$ . To accomplish this, it is assumed that due to the first order Doppler shift, the OFDM frame could be expanded towards the leading edge or compressed towards the trailing edge in the range  $[T(1 + \Delta(t)) + \tau_{\max}, T(1 - \Delta(t)) + \tau_{\max}]$ , respectively. Therefore, the linear part of the speed variation can be formulated by the following first order equation:

$$y = mx_i + b, \quad (15)$$

where  $m = (\hat{\phi}_i - \hat{\phi}_{i-1}) / (x_i - x_{i-1})$  denotes the slope, and  $x_i$  is the OFDM symbol at index  $i$ , as shown in Figure 4. Accordingly, the gradient will vary gradually in accordance with the speed change and, subsequently, the output value  $y_i$  is obtained. The slope here is determined based on the previous two OFDM symbols estimated in (17) and subsequently used to predict the timing offset  $\phi$  for the next OFDM symbol. Therefore, the first order predicted timing offset of the current OFDM symbol can be formulated as

$$E[\phi_i] = 2\hat{\phi}_{i-1} - \hat{\phi}_{i-2}. \quad (16)$$

**4.2. Fine Symbol Timing Offset and Synchronization.** Thus far, two estimations of the same parameter  $\hat{\phi}$  have been obtained. It should be stressed that attaining accurate timing offset estimation may be difficult in the presence of noise and/or ISI, especially with a short observation window. Therefore, for the purpose of increasing the reliability of

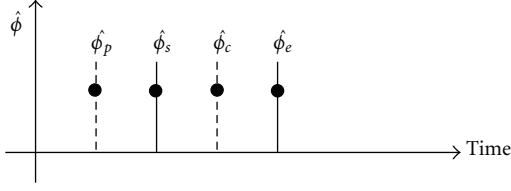


FIGURE 5: Tracking the Doppler within the OFDM symbol.

estimation, smoothing the timing offset is adopted. This yields the following fine tuned estimated timing offset:

$$\hat{\phi}_i = \hat{\phi}_i W_1 + E[\phi_i] W_2, \quad (17)$$

where the coefficients  $W_1$  and  $W_2$  are empirically obtained and satisfy the condition of  $0 < W_1 + W_2 \leq 1$ . These coefficients are designed to attain a tradeoff between estimation accuracy and tracking capabilities. It is crucial to mention that these coefficients have an effect on adapting the slope variation, where  $W_1 = 1, W_2 = 0$  indicates fast slope variation and the linear expectation does not hold. At the same time,  $W_1 = 0, W_2 = 1$  accommodate a constant gradient between symbols. The estimated fine timing offset  $\hat{\phi}$  in (17) still represents the average. Assuming the change in the time scale is linear within the OFDM symbol, the change in the speed is considered unidirectional. This will enable tracking of the Doppler shift caused by speed variation within the OFDM symbol time. Performing such tracking demands knowledge of the timing offset at both edges of the symbol in order to determine the tracking step. By involving previous estimation of fine symbol timing offset  $\hat{\phi}_p$  and current fine symbol timing offset  $\hat{\phi}_c$ , the offset at the leading edge can be formulated as

$$\hat{\phi}_s = \frac{\phi_p + \phi_c}{2}. \quad (18)$$

At the same time, the sampling frequency offset at the trailing edge  $\hat{\phi}_e$  is determined as

$$\hat{\phi}_e = 2\hat{\phi}_c - \hat{\phi}_s, \quad (19)$$

where  $\hat{\phi}_p$  and  $\hat{\phi}_c$  represent the average fine timing offset estimate from (17). It should be stressed that the estimation accuracy of these two parameters plays an important role in increasing the ability to compensate for the Doppler shift and its residual effects in the subsequent stages.

**4.3. Tracking the Doppler Shift.** If the relative velocity between the transmitter and receiver during the packet time is constant, that is, for zero acceleration, then the Doppler shift estimate computed can be used to compensate for the entire OFDM symbol. In time varying Doppler shift, however, a unique interpolation factor for the whole symbol does not hold due to the resulting nonnegligible sampling frequency errors which must be tracked. Therefore, the sampling frequency offset affects channel estimation, which is computed over pilot subcarriers, due to the different delays

of the positions of these pilots. By searching for the delay in the 1st significant arrival of the estimated CIR [20], an approach to tracking the fractional sampling clock frequency offset due to a symbol timing error is possible. However, in the case of time-varying Doppler shift, it is necessary to estimate the sampling frequency offset frequently.

An alternative realistic Doppler shift estimator, which can be realized by adopting frequent estimation of this parameter during the symbol time in the time domain, is proposed here. In order to track the Doppler shift, it is necessary to derive a tracking step that corresponds to the sampling frequency offset change over  $\hat{\phi}_s < \hat{\phi}_s + T_s < \hat{\phi}_e$ . In such a case, the tracking step is given as

$$\phi_{\text{step}} = \frac{\hat{\phi}_e - \hat{\phi}_s}{L_f}, \quad (20)$$

where  $L_f$  represents the up-sampled subcarriers. As shown in Figure 5, each OFDM symbol is identified by the two parameters of sampling frequency offset  $\hat{\phi}_s$  and  $\hat{\phi}_e$ , based on the assumption that the speed changes linearly. Accordingly, the estimated timing offset at the leading edge is updated at each sample time  $k$ , based on the step in (20). At the same time, the integer Doppler shift can be computed as

$$\hat{\Delta}(k) = \frac{L_f - \hat{\Psi}(k)_{(\text{quant})}}{L_f}, \quad (21)$$

where  $\Psi$  is the sampling frequency offset initialized with  $\hat{\phi}_s$ , and then updated at each sample as

$$\Psi(k) = \Psi(k-1) + \hat{\phi}_{\text{step}}, \quad (22)$$

and  $\hat{\Psi}_{(\text{quant})} = \lceil \hat{\Psi} \rceil$  is rounded towards the nearest integer, respectively. This integer resampling factor is delivered to the sample-by-sample Lagrange quadratic interpolation unit, as shown in Figure 2(b), and the fractional part is dealt with as a carrier frequency offset. It should be stressed that the resolution of the interpolation factor in (21) is entirely dependent on the transmitted frame length.

**4.4. Residual Doppler Shift Estimation.** Efficient Doppler shift compensation relies on how accurately the resampling factor estimation reduces the residual Doppler. This residual Doppler has a direct impact on the performance of the receiver. Taking this effect into account involves finding the amount of the fractional part of the estimated samples that shifts the subcarrier spacing fractionally. This deviation can be modelled as  $(\hat{\Psi}(k) - \hat{\Psi}_{(\text{quant})})$ , and therefore

$$\hat{\epsilon}(k) = \left[ \hat{\Psi}(k) - \hat{\Psi}_{(\text{quant})} \right] \delta f \frac{f_c}{f_s}, \quad (23)$$

is the residual frequency estimate. The residual Doppler shift is not constant at each sample within the OFDM symbol, and thus it is dealt with by determining the standard deviation across the fractional part of the estimated Doppler shift. Once the Doppler shift and its residual have been estimated

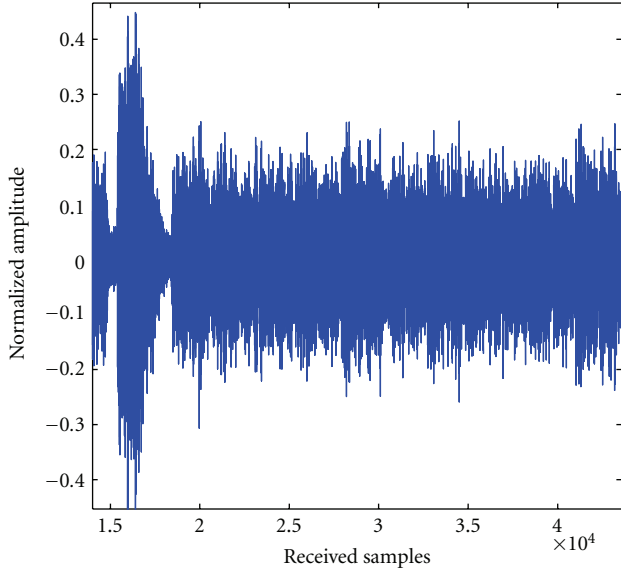


FIGURE 6: Received signal.

and compensated, the output signal  $r(k)$  is delivered to the outer receiver in Figure 2(b). This signal is firstly down sampled and then its cyclic prefix is discarded. The PAPR phases  $\mathbf{u}_i$  are removed prior to FFT demodulation. The zero forcing equalizer (ZFE) and least square (LS) method for channel estimation purposes are adopted by utilizing pilots which are embedded in a comb method. After removing the channel effect, the subsequent stage is BICM-ID.

**4.5. Pilot-Based Channel Estimation.** In the channel estimation of the OFDM symbol, a comb-type arrangement of the training sequence (pilot) is adopted. In this scheme, specific tone indices are allocated on all transmitted OFDM symbols and the rest for data transmission. Unlike a block-based training sequence, the comb type is quite convenient for fast fading channels. Additionally, with the comb type, all pilots and data are transmitted simultaneously on all symbols.

It is worth pointing out that in order to increase the accuracy of the channel estimation, the residual Doppler shift should be eliminated [21]. This is due to an induced ICI which destroys the orthogonality among subcarrier frequency components and ultimately the diagonal of the channel matrix. In OFDM systems, the advantage of increasing the symbol duration in reducing the ISI effect can conflict with increasing the ICI impact, as a consequence of subcarrier spacing reduction. Therefore, after resampling and CFO compensation, all subcarriers are orthogonal (i.e., ICI free).

The channel estimation was implemented using the following least square (LS) method [22]:

$$\begin{aligned} X(n) &= X(mL + l) \\ &= \begin{cases} X_p(m), & l = 0 \\ X_d(m), & l = 1, \dots, L - 1, \end{cases} \end{aligned} \quad (24)$$

where  $L = N_c/N_p$  and  $X_p(n)$  is the  $n$ th pilot subcarrier value. Let  $H_p(n)$  be the frequency response of the channel for  $n = 0, \dots, N_p - 1$  at pilot subcarriers. Let  $Y_p(n)$  be the received pilot symbols after the FFT operation, the estimate of the channel at pilot subcarriers  $\hat{H}_p(n)$  is given as

$$\hat{H}_p(n) = D[X_p(n)]^{-1} Y_p(n), \quad n = 0, \dots, N_p - 1, \quad (25)$$

where  $D[X_p(n)]$  is a diagonal matrix constructed using the known transmitted pilot symbols.

For subcarriers  $n = 0, 1, 2, \dots, N_c - 1$ , LS channel estimation  $\hat{\mathbf{H}}_{LS}$  is written as

$$\hat{\mathbf{H}}_{LS}[n] = \frac{\mathbf{Y}[\mathbf{n}]}{\mathbf{X}[\mathbf{n}]}. \quad (26)$$

The mean square error of the LS channel estimation is considered high when compared with the minimum mean-square error (MMSE) estimate [23]. However, LS is attractive in implementing real-time systems due to its simplicity. In order to increase the reliability of the channel estimation, an interpolation in frequency domain between each pilot and data subcarriers is adopted. It is well known that the LS is the first step of the channel frequency response estimation for the known pilots and should be followed by interpolation to obtain a nonpilot subcarriers frequency response.

## 5. Experimental Results

During the summer of 2009, an experiment was conducted in the North Sea to evaluate the system performance. In the trial setting, the transmitter and receiver were set at 10 and 5 m from the sea surface, respectively. The set-up ranges between the transmitter and the receiver were 200 m, 500 m, and 1000 m. The transmitter power was set to 180 dB re  $1 \mu\text{Pa}@1 \text{ m}$  which is the equivalent of approximately 10 W. In the trial, transmission was organized in packets of equal duration, each containing one 50 ms LFM followed by a 12.5 ms silent period and then 10 CP-OFDM frames. A total of 8920 information bits were transmitted in each setting. A total of 20 packets of 2.795 s were sent. The carrier frequency was set to 12 kHz, whereas the sampling frequency was  $4f_c$ . 1024 subcarriers were employed and the system bandwidth was 4 kHz, which led to a subcarrier spacing of 3.90625 Hz. The guard interval was set at  $T_g = 16 \text{ ms}$ . Figures 6 and 7 show the channel measurements over a range of 1000 m. These figures show a received frame structure and the normalized CIR of a packet that exhibits maximum delay spread of the order of 6 ms, respectively. This multipath delay is equivalent to an ISI of 24 symbols for a system bandwidth of 4 kHz, and this delay spread is inversely proportional to the range. In addition to the silent period shown in Figure 6, the CP guard time also contributes towards reducing the ISI effect.

**5.1. Proposed Receiver Performance.** To evaluate the performance of the proposed system, the experimental results for both block-based and proposed techniques are depicted in Figure 8(a). The performances of both receivers are presented

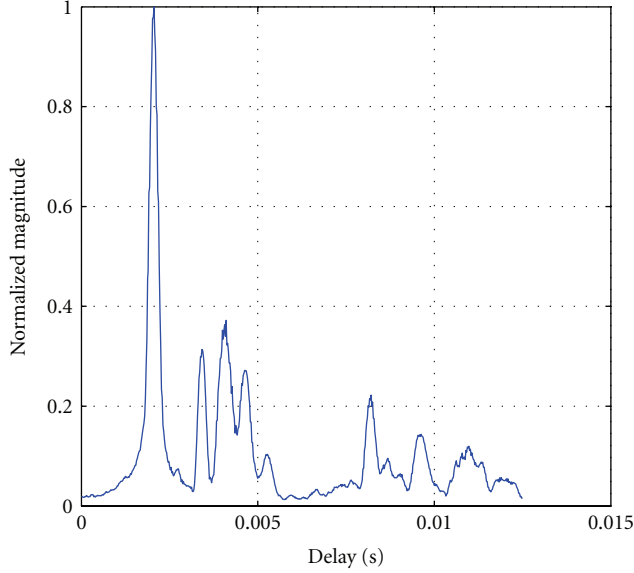


FIGURE 7: Sample of normalized channel impulse responses for 1000 m channel range.

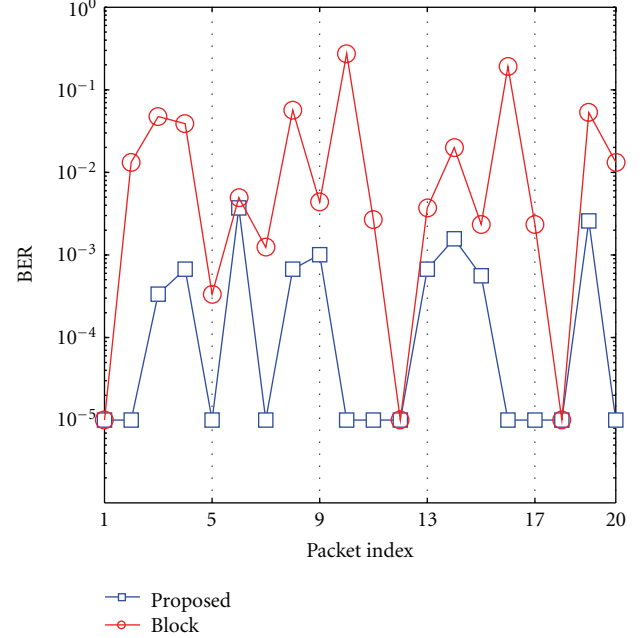
TABLE 1: Average BER comparison of the experimental results at different settings of weighting coefficients between the proposed and block-based Doppler shift techniques for  $N_c = 1024$ .

Method	Error statistics	
	Errors	BER
Block	6503	0.0365
Proposed-set 1	772	0.004
Proposed-set 2	105	0.0006

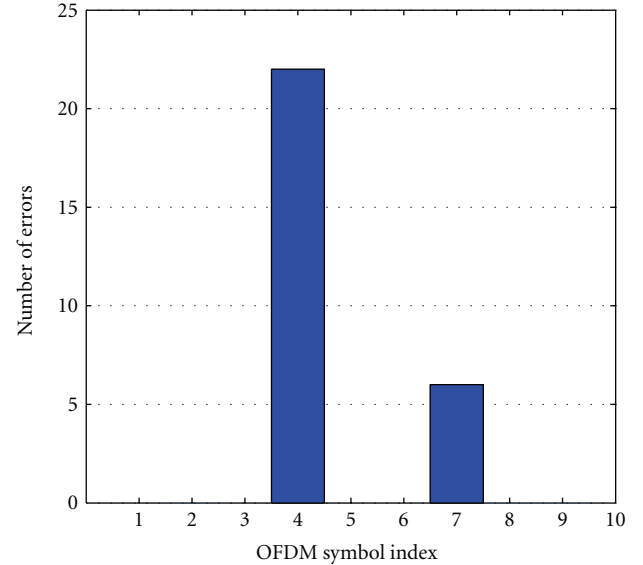
TABLE 2: Performance of the experimental results between the improved and block-based Doppler shift techniques for  $N_c = 1024$ .

Packet index	1	2	3	4	5	6	7	8	9	10
Block	0	119	423	347	3	44	11	505	39	2443
Proposed	0	0	3	6	0	33	0	6	9	0
Improved	0	0	0	0	0	3	0	0	0	5
Packet index	11	12	13	14	15	16	17	18	19	20
Block	24	0	33	178	21	1702	21	0	471	119
Proposed	0	0	6	14	5	0	0	0	23	0
Improved	0	0	0	0	9	0	0	0	0	0

in terms of bit error rate (BER). In the block-based method, single resampling is performed for the received signal. It can be seen that for all packets the proposed technique outperforms the block-based method. This is further clarified in Table 2 which shows that the proposed technique achieves acceptable performance in reducing errors in all packets compared with the block technique. Error statistics for both schemes are presented in Table 1. It can be seen that compensating the time-varying Doppler scale and its residual leads to a reduction in the BER from 0.0365 to 0.0006, which is equivalent to 98.4%. However, Figure 8 shows high decoding error in packet 6.



(a) BER for each packet over 1000 m range, where the label  $10^{-5}$  represents zero error



(b) Error statistics for packet 6; 2 out of 10 have decoding errors

FIGURE 8: Performance of the proposed system at 1024 subcarriers.

In Figure 8, the bit errors are high only in two blocks within packet 6, as shown in Figure 8(b). This is due to the noise effect which affects the Doppler scale estimation when estimating the timing offset. Evidence for this is shown in Figures 9(b) and 9(d), where in packet 6 there is a mismatch in estimating the speed at the end of symbol 3 and at the start of symbol 4. Therefore, a decoding error results in symbol 4. Furthermore, it can be seen from Figure 9(a) that there is a relatively high deceleration of  $\sim 0.9 \text{ m/s}^2$  during the symbol time, which adds an error in approximating the correlation-based Doppler scale estimation. This result shows that there

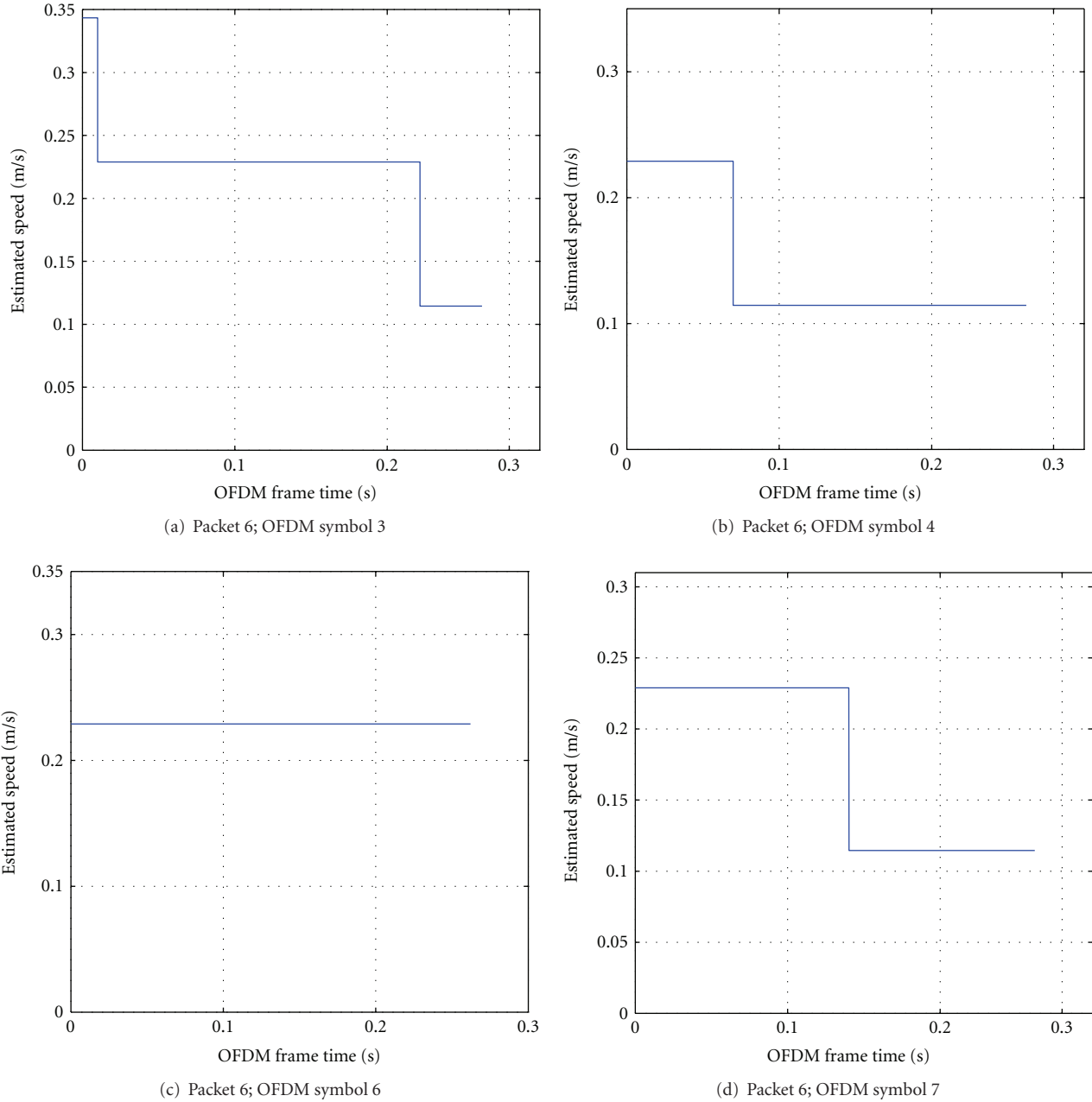


FIGURE 9: Estimated speed variation during OFDM symbol.

is a limitation on the acceleration that can be adopted in this algorithm.

Figure 9 demonstrates that the adopted system is capable of precisely tracking the speed variation in each symbol. Particularly, in Figure 9(a), the speed in symbol 3 of packet 6 has been changed three times during 0.256 s, whereas in Figure 9(c) the speed is constant. However, changing the direction of velocity within the packet period, along with higher acceleration, can produce higher intercarrier interference levels in the system. The source of this noise is the mismatch introduced by the transition from acceleration to deceleration, or vice versa. The proposed system detects this critical point through the CP correlation-based Doppler scale

estimation, and the linear expectation has no effect on this scenario. However, linear expectation reduces the channel and/or noise effect on the CP correlation. Consequently, accurate Doppler scale estimation is obtained.

Figure 10 shows the performance of bit-interleaved coded modulation with iterative decoding (BICM-ID) and ZFE in the experiment. In terms of Figure 10(a), the figure shows that the ZFE delivers reliable information to the decoder. The reliability depends on how accurate the Doppler shift compensation is. It was mentioned earlier that the channel estimation is affected by the presence of residual Doppler shift which can cause ICI, and, as a result, the orthogonality is destroyed. Consequently, the iterative decoding stage can

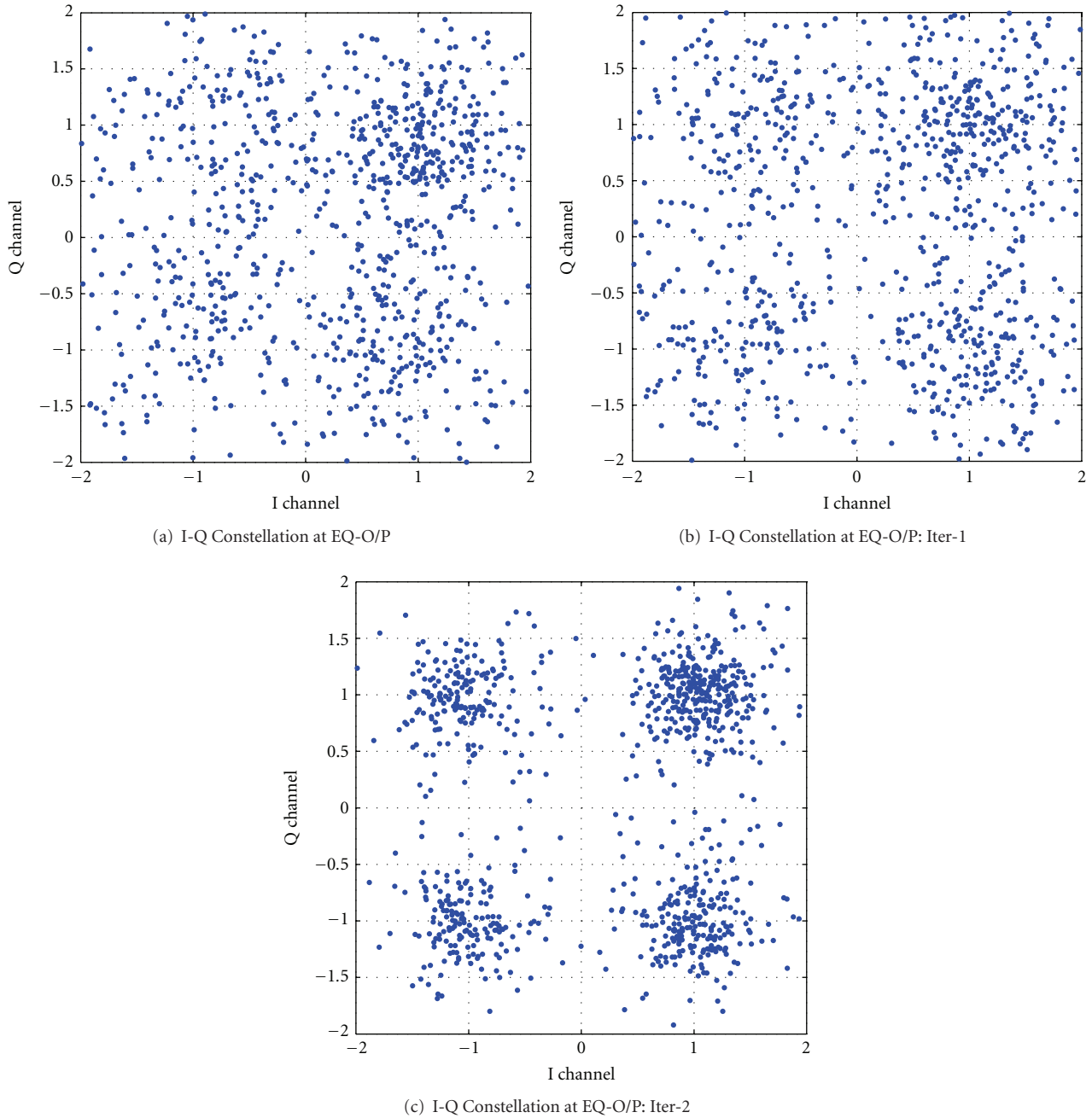


FIGURE 10: Constellation output from equalizer and iterative receiver.

generate unreliable LLRs [24]. Thus, it can be seen that there is an improvement in the second iteration in Figure 10(c) compared with the first iteration in Figure 10(b). At this stage, further iterations are pointless and no more gain is expected.

**5.2. Effect of Weighting Coefficients.** As mentioned in [13], the weighting coefficients play an important role in the accuracy of the Doppler scale estimation. For this reason, special settings of these parameters are required in order to achieve acceptable performance. It can be shown that there is a tradeoff between the value of the weighting coefficients

and the receiver performance. To be more specific, by appointing the symbol timing offset, estimated by linear expectation, a lower weighting coefficient than correlation-based symbol timing offset estimation means there is a constant acceleration or deceleration between symbols, and vice versa. As shown in (17) and (20), the Doppler scale is approximated based on estimating the fine symbol timing offset and its tracking step is derived based on the sampling frequency offset at the start and end of the OFDM symbol. This means that the weighting coefficients have a direct effect on the estimation of the time varying Doppler scale  $\Delta(t)$ .

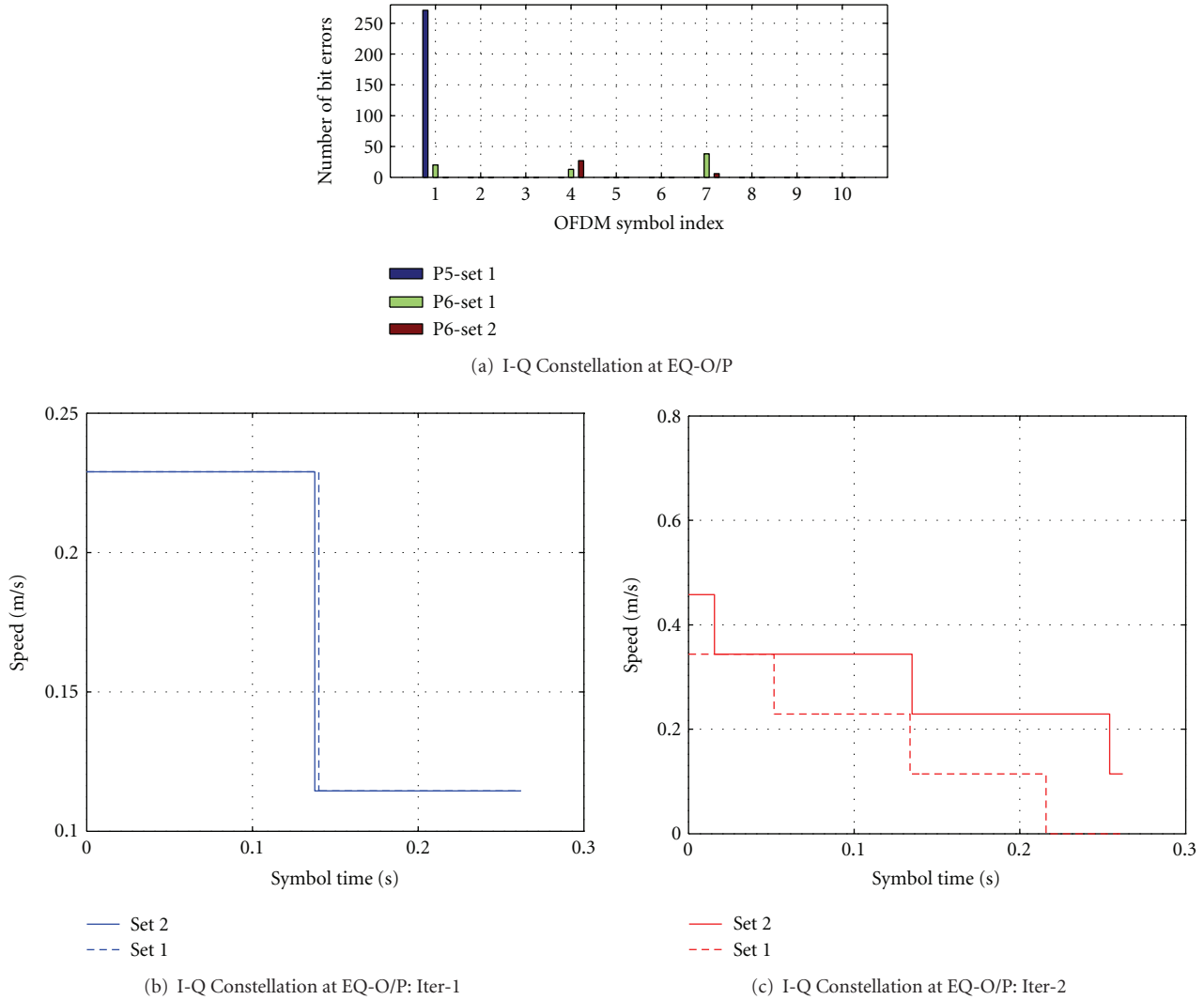


FIGURE 11: Effect of weighting coefficients on estimation.

Figure 11 shows two settings of these parameters and their effect on the performance of the receiver. In set 1, where  $W_1 = 0.5$  and  $W_2 = 0.5$ , it can be seen that the receiver performance is poor. In Figure 11(a), it is obvious that packets 5 and 6 in set 1 exhibit a high BER of 271/8920 and 71/8920, respectively. The reason for this degradation is that increasing the weight of the linear expectation in a channel leads to significant acceleration that can cause maladjustment of the interpolation factor and make the tracking of the Doppler scale change coarsely. This is shown in Figure 11(c). Although both sets have the same slope, there is a mismatch between them at the start and end of speed estimation. In set 2, on the other hand,  $W_1 = 0.85$  and  $W_2 = 0.15$ , there is a great improvement in the performance as shown in Figure 11(a), with 0 errors in packet 5 and 33 bits in packet 6. Table 1 shows the performance of the receiver for the subcarriers 1024 over a range of 1000 m using two different settings of the weighting coefficients. In set 2, it can be observed that the error decreases by about 86.4% compared with set 1.

**5.3. Performance Evaluation with Improved Coarse Timing Estimation.** As mentioned earlier, the impairments in the channel estimation due to synchronization failure will result in unreliable LLRs as a consequence of the Doppler effect. In contrast, estimating and compensating the Doppler scale precisely causes the received OFDM symbol to coincide with its transmitted period, thus improving the channel estimation and delivering reliable symbols to the decoder. Therefore, the target is to improve the Doppler scale estimation and ultimately reduce the burden on the channel estimation.

In order to extract the Doppler scale successfully, it is important to increase the reliability of estimating the symbol timing.

Considering the effect of acceleration on the chirp correlation is small, in the case of multiple OFDM symbols within a packet, the symbol timing error in each OFDM block is accumulated with acceleration error during the packet time. Hence, adopting a single estimation of  $\zeta$  for the whole packet is no longer accurate. Therefore, in order to mitigate the acceleration effect on the symbol timing error,  $\zeta$  needs

to be fine tuned. Performing the fine tuning necessitates updating the position of  $\zeta$  after each symbol time. Let  $m, i$  denote the range of the timing offset around the leading and the trailing edge during the OFDM symbol, respectively. It follows that a two-dimensional timing function is written as

$$\Lambda(m, i) \triangleq \left| \sum_{n=0}^{N_g-1} r(\zeta + m + n)r(\zeta + n + N + i) \right| \quad (27)$$

$$m \in \left\{ -\frac{W}{2}, \dots, \frac{W}{2} \right\}; i \in \left\{ -\frac{Y'}{2}, \dots, \frac{Y'}{2} \right\}.$$

Then,  $\hat{\theta}_{m,i}$  can be estimated from obtaining the maximum peak of the multiplication, and it can be written as

$$\hat{\theta}_{m,i} = \arg \max_{m,i} \Lambda(m, i) \quad (28)$$

$$m \in \left\{ -\frac{W}{2}, \dots, \frac{W}{2} \right\}; i \in \left\{ -\frac{Y'}{2}, \dots, \frac{Y'}{2} \right\},$$

and the fine tuned  $\zeta'$  is obtained. The implementation of this fine tuning algorithm of the coarse packet synchronization can be summarized as follows:

- (1) compute the coarse packet synchronization point  $\zeta$  which represents the time position of the maximum peak of the chirp correlation,
- (2) compute the timing function  $\Lambda(m, i)$  for  $m \in [-W/2, W/2], i \in [-Y'/2, Y'/2]$ ,
- (3) choose the maximum of the maximum of  $\Lambda(m, i)$  as the estimated packet timing offset,
- (4) update  $\zeta$  to be fine tuned which is given as

$$\zeta' = \zeta + \hat{\theta}. \quad (29)$$

It should be noted that a two-dimensional search (i.e.,  $m$  and  $i$ ) is included in the proposed timing function  $\Lambda(m, i)$ . This is the main difference from the single synchronization point estimation in [14], where only coarse estimation of the packet synchronization point is adopted. The first search parameter is  $m$ , corresponding to the first search region in the range around the coarse synchronization point  $\zeta$ . Meanwhile, the second search parameter is  $i$ , corresponding to the range in the region around the tail of the OFDM symbol which yields the expected Doppler shift. Once the fine-tuned  $\zeta'$  is obtained, the subsequent stage is the estimation of the first order moment  $\hat{\phi}$ . In existing techniques, [6] and [14], due to the acceleration and the inherent ISI, there is a fluctuation in the maximum of the timing function, and the channel conditions have a direct effect on this maximum. Therefore, centroid-based localization is adopted to estimate  $\hat{\phi}$ , because it reduces the position uncertainty caused by the fading channel, and the search range is built on the fine-tuned  $\zeta'$ , which can be written as

$$r_D \in \left[ \zeta' + N_g + N - \left( \frac{Y}{2} \right) + i, \zeta' + N - \left( \frac{Y}{2} \right) + i \right], \quad (30)$$

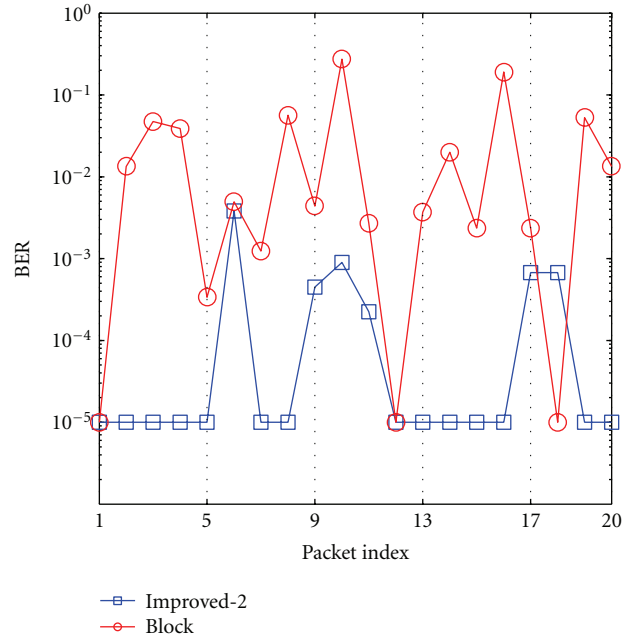


FIGURE 12: Performance of the proposed system with improved coarse timing estimation.

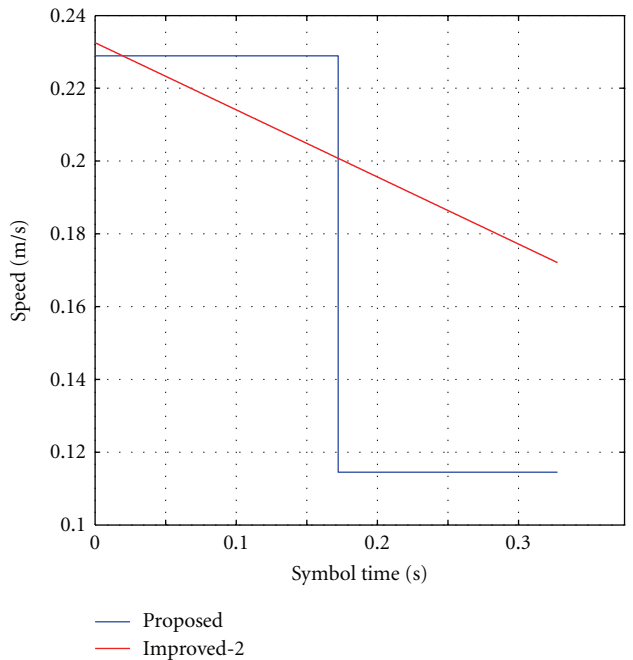
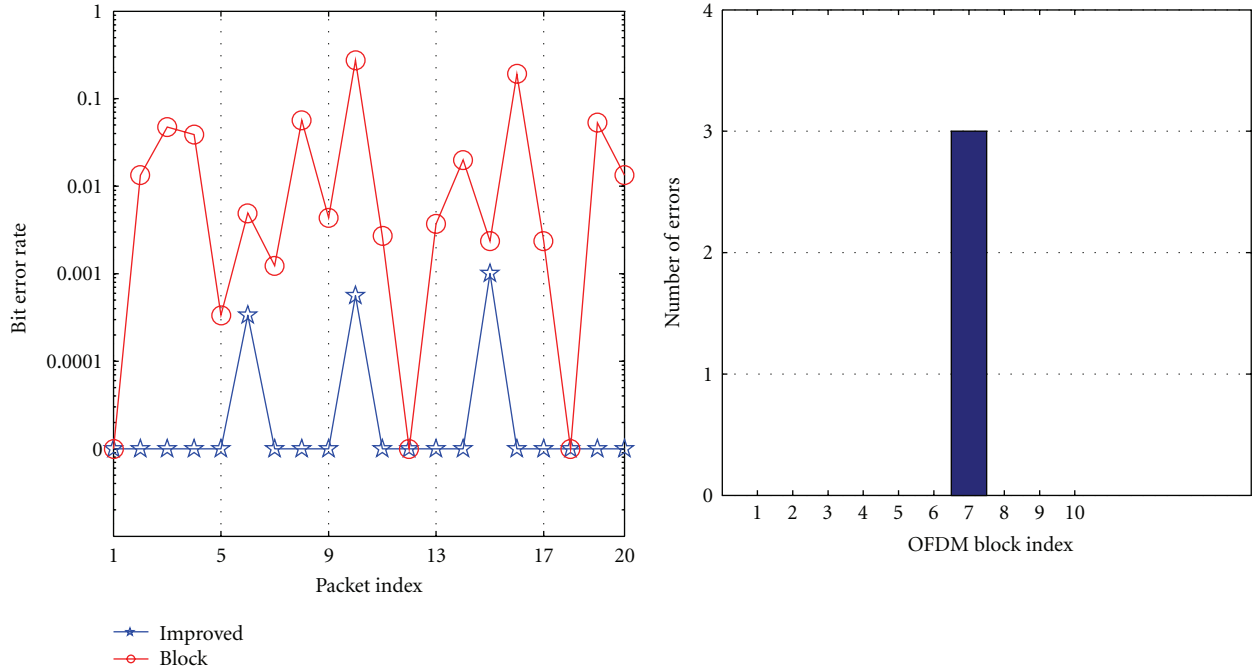


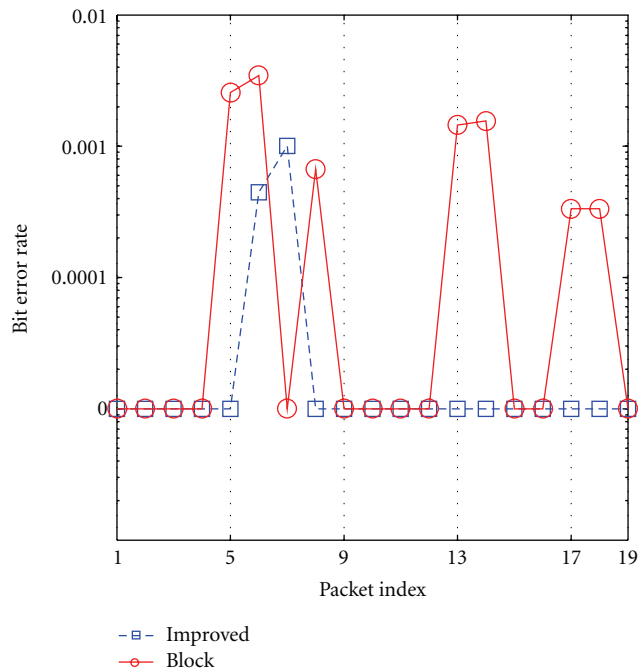
FIGURE 13: Improved time-varying speed estimation during OFDM symbol 7 of packet 6.

and the centroid-based first order moment  $\hat{\phi}_l$  is given as in [14]. Figure 12 shows that fine tuning this parameter results in reducing the BER. It can be inferred from this figure that adjusting the misalignments of the symbol timing due to the time-varying Doppler scale results in an improvement in the reliability of the resampling factor estimation, which in turn reduces the noise that accompanies accumulated errors from symbol to symbol within each packet and ultimately a reduction in BER is obtained.



(a) BER for each packet over 1000 m range

(b) Packet 6; symbol 7 error statistics



(c) BER for each packet over 1000 m range at 512 subcarriers

FIGURE 14: Performance of the improved proposed system.

5.4. Performance Evaluation Based on Two-Point Correlation. Fine tuning of the coarse symbol timing facilitates an alternative approach to estimating the first order moment of the correlation lag. The suggested approach here aims to increase the confidence of estimation by considering the first order moment that results from two correlation lags. The first correlation lag is estimated by means of centroid-based

localization, in accordance with the anticipated window mentioned earlier. This type of correlation gives an accurate indication of the fractional part of the time-scale expansion/compression. However, the centroid-based localization is severely affected due to the velocity perturbation. This perturbation degrades the estimation performance of the timing function and ultimately  $\hat{\phi}_i$ . Therefore, an alternative

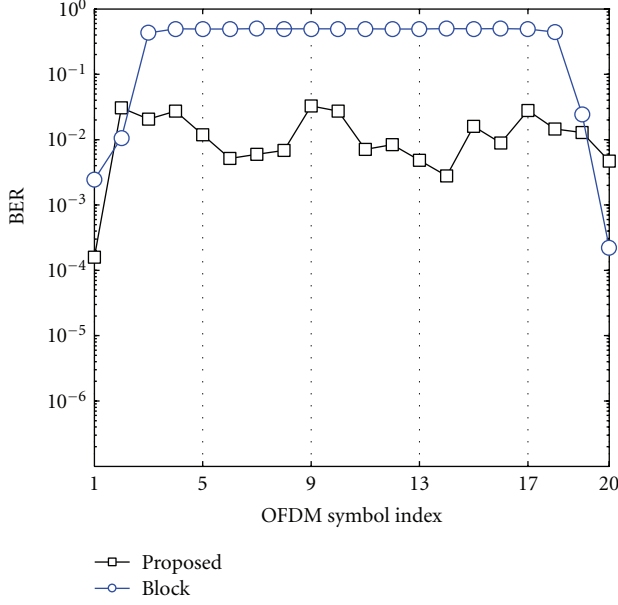


FIGURE 15: Performance comparison of block-based and proposed techniques.

approach has been adopted by involving another estimation point based upon full cross correlation of the CP with its replica. The addition of this correlation is based on the idea of increasing the certainty of the first order moment estimation. This correlation is based on the assumption that the OFDM timing is approximately aligned due to the fine tuning of the packet synchronization  $\zeta'$ . By definition, the cross correlation between a pair of energy signals,  $x[n]$  and  $y[n]$ , is given by [25];

$$r_{xy} = \sum_{n=-\infty}^{\infty} x[n]y[n-\chi], \quad \chi = 0, \pm 1, \pm 2, \dots, \quad (31)$$

where the parameter  $\chi$  is called lag and it indicates the time shift between the pair. Based on this theory, the time shift in samples for either expansion or compression can be measured with respect to a reference sequence length of the guard interval  $N_g$ . In the case of the existence of Doppler shift, the received samples are shifted to the right in expansion or left for compression with respect to the reference. To be more specific, once the start of the packet  $\zeta$  is identified, it can be deemed that the symbol timing identification is reliable, and the correlation between the received CP and its replica is computed to measure the time shift in the samples as follows:

$$\Lambda_c \triangleq \left| \sum_{n=0}^{N_g-1} r(\zeta' + n)r(\zeta' + n + N - \chi) \right|, \quad (32)$$

$$\chi = 0, \pm 1, \pm 2, \dots$$

Considering that the reference sequence of the transmitted CP is  $N_{cp}N_s$ , the first order moment of the Doppler shift  $\phi_x$  can be approximated as

$$\hat{\phi}_x = \arg \max \Lambda_c - N_{cp}N_s, \quad \chi = 0, \pm 1, \pm 2, \dots \quad (33)$$

Adopting such a scenario requires extraction of a fine tuned correlation lag. This necessitates involvement of two parameters of weighting coefficients to perform such a smoothing approach, as mentioned earlier. The coefficients  $W_1$  and  $W_2$  are empirically obtained from the experiment to accommodate the measured channel condition. Therefore,  $\phi'$ , which represents the fine tuned first order moment of the correlation lag, is given as

$$\phi' = \hat{\phi}_x W_1 + \hat{\phi}_l W_2. \quad (34)$$

This fine tuned parameter is then delivered to the Doppler extraction in Figure 2(b) in order to estimate the Doppler shift. Accordingly, the estimated Doppler shift, which comprises both an integer and fractional part, is considered and utilized for compensation. Therefore, the estimated resampling factor requires no extraction of the fractional part to estimate the residual Doppler shift, as shown in Figure 2(b); hence, the CFO is approximated as

$$\hat{\epsilon} \simeq 0.5 f_c \delta f / f_s \simeq \frac{\delta f}{8}, \quad (35)$$

where  $f_s = 4f_c$ . For subcarrier spacing of 3.90625, as in the case of 1024 subcarriers,  $\hat{\epsilon}$  is 0.4883 Hz. These two-point estimations of  $\hat{\phi}_l$  and  $\hat{\phi}_x$ , in conjunction with  $\phi'$ , contribute towards improving the Doppler shift estimation and thus eliminate the need to determine the CFO. Figure 13 demonstrates the implications of improving the Doppler shift estimation. It is obvious in this figure that there are two estimations that show the deceleration in velocities over the symbol time. With respect to the improved system, the gradient is estimated smoothly. This confirms that an accurate estimation of the drift in samples results in an accurate estimation and tracking of the time-varying Doppler shift. On the other hand, this figure illustrates that perturbations in estimating the variation of speed within the OFDM symbol can lead to inaccurate resampling factor estimation. In particular, it can be inferred from this figure that there is a time-varying Doppler shift during the symbol time which decelerates in the order of 0.25 m/s<sup>2</sup>. This deceleration is estimated by smoothing  $\zeta$  estimation. However, in the proposed system, the deceleration is approximated to 0.48 m/s<sup>2</sup> over the same symbol. For the sake of clarity, the “proposed system” refers to the system before the improvements and the “improved system” refers to the proposed system after improving  $\zeta$  estimation. Table 2 illustrates the performance comparison between block-based Doppler compensation, time varying Doppler shift compensation, and its improvements. The achieved BER decreases significantly in the proposed system compared with the block-based approach. Likewise, there are additional improvements in the BERs of 83.8% compared with the proposed technique. This is shown in Figure 14(a), where the BER of packet 6 is reduced compared with Figure 8(a). Additionally, the error statistics of packet 6, shown in Figure 8(b) and Figure 14(b), confirm that estimating multilags contributes to an increase in the accuracy of the speed estimation.

As demonstrated in Figure 14(c) and Table 3, the experimental results show that the investigation was also

TABLE 3: Performance of the experimental results between the improved and block-based Doppler shift techniques for  $N_c = 512$ .

Packet index	1	2	3	4	5	6	7	8	9	10	11	12	13	14	15	16	17	18	19
Block	0	0	0	0	23	31	0	6	0	0	0	0	13	14	0	0	3	3	0
Improved	0	0	0	0	0	4	9	0	0	0	0	0	0	0	0	0	0	0	0

TABLE 4: OFDM symbol structure and the corresponding data rates.

$N_c$	$N_d$	$N_p$	$N_b$	Data rates (kb/s)
512	448	64	20	3.0833
1024	896	128	10	3.2794

TABLE 5: Complexity estimate.

Operator	Method	
	2D search + centroid	Correlation
+, -	$9Y' \times W + 8Y$	$N_g(\log_2 N_g + 1)$
$\times$	$N_g \times Y6' \times W + Y \times N_g$	$3N_g \log_2 N_g$

successful with 512 subcarriers, as it was able to improve performance by about 86%. This was an expected result, because reducing the symbol length entails increasing the subcarrier spacing and reducing the sensitivity to the Doppler shift. Additionally, reducing the symbol length enables more frequent tracking of the Doppler shift. However, severe consequences accompany this reduction in the symbol time, since it mitigates immunity against ISI, in addition to reducing the available bandwidth. This performance reveals that improving the synchronization and adopting smoothing produces low BER. Furthermore, compensating residual Doppler shift or CFO preserves the orthogonality of the subcarriers and ultimately contributes towards mitigating decoding errors. However, it is worthwhile mentioning that this approximation of the CFO cannot be extrapolated to all cases, as in the case of higher acceleration where a special signal processing method, such as an adaptive weighting coefficients selection and/or iterative-based estimation of the Doppler shift, should be adopted due to the effect of the time varying Doppler shift and the inherent ISI on the correlation peak. Another problem with this approach is that it fails to compensate for an abrupt change in the direction of velocity, as it needs at least two symbols to self-adapt to this sudden variation which causes a decoding error.

In terms of the achieved data rate, Table 4 presents two types of OFDM subcarrier allocation that account for the transmission overhead due to pilots, channel coding, and guard period.

Figure 15 shows, in terms of BERs, the performance comparison between the block-based approach and the proposed technique. For the block-based approach, two scenarios of the transmitted packet structure are investigated. The first structure includes 20 ms chirp, followed by a silent period then 10 CP-OFDM symbols. The second structure comprises only a single CP-OFDM frame. The former structure is investigated in the experiment; therefore the second structure is considered here for the purpose of the simulation. It can be seen that the performance of the

block approach is poor in the case of multi-scale Doppler within the OFDM symbol. When the speed is low, as shown in the OFDM symbols indices 1 and 20, the block algorithm performance is approximately identical to that of the proposed scheme. However, as the speed increases, the BER also increases in the block-based approach, whereas the proposed algorithm demonstrates less performance error despite an escalation in speed. The degradation in the BERs in the proposed algorithm is due to the effect of the acceleration on the CP correlation.

Additionally, the complexity of the improved algorithm is summarized in Table 5. The complexity estimate includes a two-dimensional (2D) search algorithm mentioned in (32), centroid algorithm in [14], and cross correlation of the received CP samples. In this table, it is shown that the complexity is a linear function of the CP length and the parameters  $Y$ ,  $Y'$ , and  $W$ . It is worth to mention that the correlation complexity estimate is estimated via FFT-based correlation. It can be noticed that no division operation is required. Therefore, in terms of hardware implementation, this Doppler estimate is considered simple.

## 6. Conclusions

The performance of multi-scale Doppler shift compensation for an OFDM-based UWA communication system has been investigated. The algorithm accommodates for channels with linear acceleration during a packet of multiple OFDM frames. Unlike existing Doppler compensation methods, the proposed scheme is more pragmatic, as it considers the notion that the speed is changing linearly during the OFDM symbol time. Additionally, under the assumption of linear speed during the packet time, it has been shown that using the linear equation approach to predict the first order Doppler shift as a reinforcement parameter leads to acceptable performance over other techniques. Furthermore, it has been shown that employing weighted coefficients improves the performance as it fine tunes the estimated parameters. However, an approach to fine tuning these parameters adaptively and in accordance with the acceleration is required.

## References

- [1] A. F. Molisch, *Wireless Communications*, John Wiley, New York, NY, USA, 2005.
- [2] B. S. Sharif, J. Neasham, O. R. Hinton, and A. E. Adams, "Computationally efficient doppler compensation system for underwater acoustic communications," *IEEE Journal of Oceanic Engineering*, vol. 25, no. 1, pp. 52–61, 2000.
- [3] B. S. Sharif, J. Neasham, O. R. Hinton, A. E. Adams, and J. Davies, "Adaptive doppler compensation for coherent acoustic

- communication,” *IEE Proceedings*, vol. 147, no. 5, pp. 239–246, 2000.
- [4] B. Li, S. Zhou, M. Stojanovic, L. L. Freitag, and P. Willett, “Multicarrier communication over underwater acoustic channels with nonuniform doppler shifts,” *IEEE Journal of Oceanic Engineering*, vol. 33, no. 2, pp. 198–209, 2008.
- [5] S. F. Mason, C. R. Berger, S. Zhou, and P. Willett, “Detection, synchronization, and doppler scale estimation with multicarrier waveforms in underwater acoustic communication,” *IEEE Journal on Selected Areas in Communications*, vol. 26, no. 9, pp. 1638–1649, 2008.
- [6] J. J. van de Beek, M. Sandell, and P. O. Börjesson, “ML estimation of time and frequency offset in OFDM systems,” *IEEE Transactions on Signal Processing*, vol. 45, no. 7, pp. 1800–1805, 1997.
- [7] B. C. Kim and I. T. Lu, “Parameter study of OFDM underwater communications system,” in *Proceedings of the IEEE Oceans*, vol. 2, pp. 1251–1255, Providence, RI, USA, September 2000.
- [8] K. Tu, T. M. Duman, J. G. Proakis, and M. Stojanovic, “Cooperative MIMO-OFDM communications: receiver design for doppler-distorted underwater acoustic channels,” in *Proceedings of the 44th Asilomar Conference on Signals, Systems and Computers*, pp. 1335–1339, November 2010.
- [9] J. Armstrong, “Analysis of new and existing methods of reducing intercarrier interference due to carrier frequency offset in OFDM,” *IEEE Transactions on Communications*, vol. 47, no. 3, pp. 365–369, 1999.
- [10] A. F. Molisch, M. Toeltsch, and S. Vermani, “Iterative methods for cancellation of intercarrier interference in OFDM systems,” *IEEE Transactions on Vehicular Technology*, vol. 56, no. 4, pp. 2158–2167, 2007.
- [11] K. Tu, D. Fertoni, T. M. Duman, M. Stojanovic, J. G. Proakis, and P. Hursky, “Mitigation of intercarrier interference for OFDM over time-varying underwater acoustic channels,” *IEEE Journal of Oceanic Engineering*, vol. 36, no. 2, pp. 156–171, 2011.
- [12] S. Yerramalli and U. Mitra, “Optimal resampling of OFDM signals for multiscale-multilag underwater acoustic channels,” *IEEE Journal of Oceanic Engineering*, vol. 36, no. 1, pp. 126–138, 2011.
- [13] A. E. Abdelkareem, B. S. Sharif, C. C. Tsimenidis, and J. A. Neasham, “Adaptive doppler-shift compensation for OFDM underwater acoustic communications system,” in *Proceedings of the Underwater Acoustic Measurements: Technologies and Results (UAM ’11)*, Kos, Greece, June 2011.
- [14] A. E. Abdelkareem, B. S. Sharif, C. C. Tsimenidis, J. A. Neasham, and O. Hinton, “Low-complexity doppler compensation for OFDM-based underwater acoustic communication systems,” in *Proceedings of the IEEE Oceans*, pp. 1–6, Santander, Spain, June 2011.
- [15] R. W. Bäuml, R. F. H. Fischer, and J. B. Huber, “Reducing the peak-to-average power ratio of multicarrier modulation by selected mapping,” *Electronics Letters*, vol. 32, no. 22, pp. 2056–2057, 1996.
- [16] M. Stojanovic, “Low-complexity OFDM detector for underwater channels,” in *Proceedings of the MTS/IEEE Ocean Conference*, pp. 18–21, Boston, Mass, USA, September 2006.
- [17] B. Li, S. Zhou, M. Stojanovic, L. Freitag, and P. Willett, “Non-uniform doppler compensation for zero-padded OFDM over fast-varying underwater acoustic channels,” in *Proceedings of the IEEE Oceans*, pp. 1–6, Aberdeen, UK, June 2007.
- [18] M. Speth, S. A. Fechtel, G. Fock, and H. Meyr, “Optimum receiver design for wireless broad-band systems using OFDM-part II,” *IEEE Transactions on Communications*, vol. 49, no. 4, pp. 571–578, 2001.
- [19] T. Pollet, P. Spruyt, and M. Moeneclaey, “The BER performance of OFDM systems using non-synchronized sampling,” in *Proceedings of the Global Telecommunications(GLOBECOM ’94)*, vol. 1, pp. 253–257, November 1994.
- [20] B. Yang, K. B. Letaief, R. S. Cheng, and Z. Cao, “Timing recovery for OFDM transmission,” *IEEE Journal on Selected Areas in Communications*, vol. 49, pp. 467–479, 2000.
- [21] M. K. Ozdemir, Logus Broadband, wireless solutions Incorporation, and H. Arslan, “Channel estimation for wireless OFDM systems,” *IEEE Communications Surveys and Tutorials*, vol. 9, no. 2, pp. 18–48, 2007.
- [22] S. Coleri, M. Ergen, A. Puri, and A. Bahai, “Channel estimation techniques based on pilot arrangement in OFDM systems,” *IEEE Transactions on Broadcasting*, vol. 48, no. 3, pp. 223–229, 2002.
- [23] M. H. Hsieh and C. H. Wei, “Channel estimation for OFDM systems based on comb-type pilot arrangement in frequency selective fading channels,” *IEEE Transactions on Consumer Electronics*, vol. 44, no. 1, pp. 217–225, 1998.
- [24] C. P. Shah, C. C. Tsimenidis, B. S. Sharif, and J. A. Neasham, “Low-complexity iterative receiver structure for time-varying frequency-selective shallow underwater acoustic channels using BICM-ID: design and experimental results,” *IEEE Journal of Oceanic Engineering*, vol. 36, no. 3, pp. 406–421, 2011.
- [25] K. S. Mitra, *Digital Signal Processing A Computer Based Approach*, McGraw-Hill, New York, NY, USA, 2006.

## Research Article

# Underwater Localization and Tracking of Physical Systems

Patrick Carroll,<sup>1</sup> Shengli Zhou,<sup>1</sup> Hao Zhou,<sup>1</sup> Xiaoka Xu,<sup>1</sup> Jun-Hong Cui,<sup>2</sup> and Peter Willett<sup>1</sup>

<sup>1</sup>Department of Electrical and Computer Engineering, University of Connecticut, Storrs, CT 06269, USA

<sup>2</sup>Department of Computer Science and Engineering, University of Connecticut, Storrs, CT 06269, USA

Correspondence should be addressed to Patrick Carroll, pec05001@engr.uconn.edu

Received 15 December 2011; Accepted 16 May 2012

Academic Editor: Charalampos C. Tsimenidis

Copyright © 2012 Patrick Carroll et al. This is an open access article distributed under the Creative Commons Attribution License, which permits unrestricted use, distribution, and reproduction in any medium, provided the original work is properly cited.

We investigate the problem of localizing an underwater sensor node based on message broadcasting from multiple surface nodes. With the time-of-arrival measurements from a DSP-based multicarrier modem, each sensor node localizes itself based on the travel time differences among multiple senders to the receiver. Using one-way message passing, such a solution can scale to accommodate a large number of nodes in a network. We consider the issue from not only the physical layer, but also at the node processing layer by incorporating a tracking solution. We present simulation results, testing results in a swimming pool featuring both stationary and moving receivers, and results from a lake test with a mobile receiver.

## 1. Introduction

Underwater localization is a topic of great interest and study, with increasingly hungry applications driving the need for better and better solutions [1, 2]. Several current systems feature augmented inertial navigation methods, which use filtering and tracking methods to provide corrections and improvements upon traditional onboard navigational equipments [3, 4]. Aside from these methods, there are several localization techniques based on acoustic signaling. The first is the long base line (LBL) system, where transponders are installed at the sea floor, and an underwater vehicle interrogates the transponders for round-trip delay estimation followed by triangulation [5]. LBL has good localization accuracy, but it requires long-time calibration. The second is the short base line (SBL) system, where a mothership moves above the underwater vehicle. The ship locates the vehicle using high-frequency directional emitters. The third approach is based on floating buoys [6, 7]. This system acts like a long base line system except that the reference points are surface buoys. There are commercial products—the GPS intelligent buoys (GIB)—that route signals from an underwater node to surface buoys [7], and using radio links, the surface buoys forward all information to a mothership, wherein the localization is performed. The floating buoys are easier to deploy and calibrate than LBL systems.

Several systems have been proposed which consider a network of underwater nodes instead of a single underwater vehicle or small group of nodes. These approaches typically use an anchor-client-based approach, where nodes systematically position themselves and disseminate this information with other nearby nodes in an effort to systematically localize the entire network [8–19]. However, few of these methods have been fully implemented in physical networking systems.

In this paper, we propose a new localization approach based on message broadcasts from multiple surface nodes, coupled with tracking algorithms and implemented on a physical system to provide a complete analysis. With the time-of-arrival measurements, the receiver computes its own localization based on the differences of the travel time among multiple senders to the receiver. We present one solution based on exhaustive search and the other based on the least-squares formulation [20]. By implementing the localization algorithms in the OFDM modem prototypes developed in [21], we have carried out tests in swimming pool and lake environments. With these point measurements, tracking analysis was also carried out on the collected data to further refine the position estimate.

Thus, we consider the problem not only at the modem physical layer with regards to timing and detection, but further analyze it in a single-point estimate, and ultimately combine the point estimates for a tracking implementation.

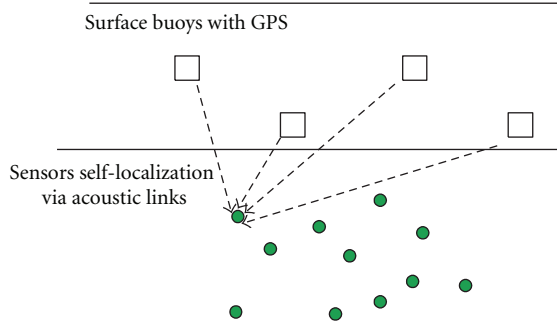


FIGURE 1: An underwater sensor network with multiple surface buoys.

In particular, we consider two tracking scenarios: a largely static scenario in which the nodes are assumed to be tethered or freely floating with no self-propulsion and a mobile scenario in which the object being tracked is assumed to make deliberate maneuvers and have some control of its motion, such as an autonomous underwater vehicle (AUV).

The advantage of the proposed localization method is that the broadcast messages can serve an arbitrary number of underwater nodes once they are in range, in contrast to many existing solutions which can only serve a small number of users.

The rest of the paper is organized as follows. We present the system overview in Section 2. Section 3 discusses the timing concerns of the physical layer. In Section 4, we consider the self-localization of a node for a single-point estimate. In Section 5, we present the series of tracking algorithms that are implemented. Sections 6, 7, and 8 contain simulation results and testing results from a swimming pool and lake, respectively. Conclusions are in Section 9.

## 2. System Overview

Figure 1 depicts the considered system setup, with several surface nodes and multiple underwater nodes. The surface nodes are equipped with satellite-based GPS receivers. Relying on the internal pulse provided by the GPS device that is accurate to within 1 microsecond GPS time, the surface nodes are assumed to be well synchronized. At predetermined intervals, the surface nodes sequentially broadcast their current location and time.

The underwater nodes within the broadcast range will detect a series of transmissions and decode those messages. By comparing the reception time with the transmission time encoded in the message, each underwater node can obtain estimates of the time of arrivals (or time of flights) of messages from different surface nodes, based on which it tries to compute its own position. Note that the broadcast from the surface to underwater nodes is a one-way transmission, that localization quality is independent of the number of underwater nodes in the network, and that there is no additional interference involved among different underwater nodes.

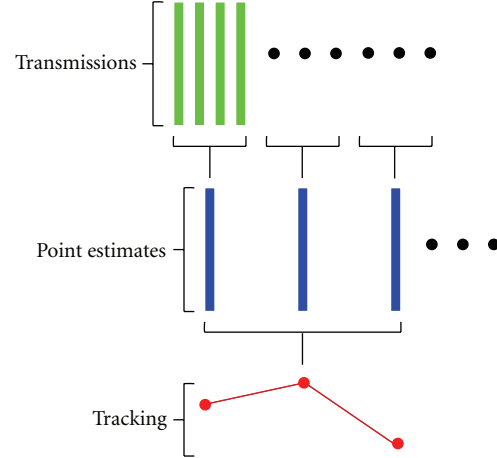


FIGURE 2: One round of surface buoy broadcasting leads to one point estimate, while tracking algorithms improve the localization accuracy when multiple-point estimates are available.

The overall scheme of localization refinement is presented in Figure 2. For one round of transmissions, the receiver obtains the travel times from all the surface buoys, based on which a point estimate is available. Once several of these broadcast periods have occurred, individual point estimates may be combined via tracking algorithms to form a more accurate understanding of the current node position. The algorithms at different stages are described in the following sections.

## 3. One-Way Travel Time Estimation

Let us focus on one receiver at position  $(x_r, y_r, z_r)$ . Suppose that there are  $N$  surface nodes, at positions  $(x_n, y_n, z_n)$ ,  $n = 1, \dots, N$ . Let  $d_n$  denote the distance between the receiver node and the  $n$ th surface node

$$d_n = \sqrt{(x_r - x_n)^2 + (y_r - y_n)^2 + (z_r - z_n)^2}. \quad (1)$$

Without loss of generality, we set the first surface node at the origin, that is,  $x_1 = y_1 = z_1 = 0$ , such that

$$d_1^2 = x_r^2 + y_r^2 + z_r^2. \quad (2)$$

The actual time of arrival is  $t_n = d_n/c$ , where  $c$  is the sound propagation speed.

The transmission time is encoded at each broadcast message. The receiver needs to estimate the arrival time of each message to provide an estimate on the time of arrival  $t_n$ . In this paper, we use real-time DSP-based OFDM modem prototypes [21], as shown in Figure 3. First, the communication channel is monitored to detect signal arrivals, based on a background noise level monitoring performed by the modem at initialization. When a signal is detected, the correlation of the signal with a sliding window of itself is compared to determine when the level of peak correlation in the preamble of the message occurs, indicated by a plateau in the correlation. Once this plateau is selected, the time of arrival is coarsely estimated as having been approximately

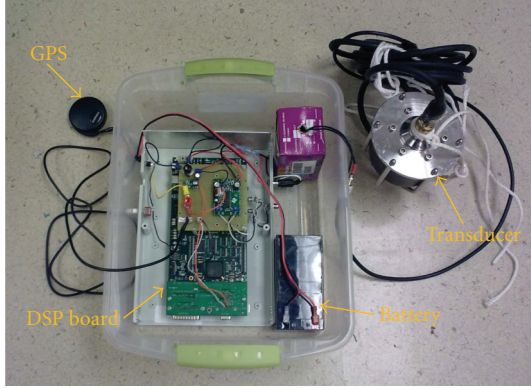


FIGURE 3: The OFDM modem prototype with an attached GPS unit.

halfway during this plateau period [22]. Once coarse channel estimation has occurred, the preamble, which is entirely known to the receiver, is used to estimate the instantaneous underwater channel conditions, and from there, a more refined estimation of the time of arrival is performed via the modified page test as in [23].

Let  $\hat{t}_n$  denote the estimate of  $t_n$  from the OFDM modem. It can be expressed as the sum of the real transmission propagation, the delay in signal processing at both transmitter and receiver  $b_n$ , and the estimation noise  $w_n$ :

$$\hat{t}_n = t_n + b_n + w_n. \quad (3)$$

Multiple tests of the OFDM modem reveal that the noise  $w_n$  has standard deviation on the order of 5–10 ms. (The bandwidth used by the OFDM modem is 6 kHz, leading to a baseband sampling interval of 1/6 ms.) On the other hand, the processing delay (bias)  $b_n$  has large magnitude, which might be on the order of 500 ms. However, tests have also shown that  $b_n$  is nearly identical across modems with similar hardware and operating software with the assumed GPS synchronization. Thus, we will treat  $b_n$  as a constant  $b_n = b$  and present the localization algorithms based on

$$\hat{t}_n = t_n + b + w_n, \quad n = 1, \dots, N. \quad (4)$$

#### 4. Localization

In each round of broadcasting from all surface nodes, a node collects  $N$  travel time measurements and can form a single-point estimate of its current position. This is accomplished by way of localization algorithms based on the intersection of spherical surfaces.

Since the bias  $b$  is unknown and usually large, time-of-arrival- (TOA-) based methods are not suitable. Instead, we use the time-difference-of-arrival (TDOA) method to cancel the common bias term  $b$  by forming

$$\Delta \hat{t}_{n1} = \hat{t}_n - \hat{t}_1, \quad n = 2, \dots, N. \quad (5)$$

The distance difference  $d_{n1} = d_n - d_1$  is then estimated by

$$\hat{d}_{n1} = c \Delta \hat{t}_{n1}. \quad (6)$$

The TDOA method also corrects for clock skew alongside this bias term, due to the nature of the shared GPS clock. Each receiving node will have its own internal clock, which at some update period  $k$  will have drifted by an unknown, nonlinear skew factor  $\phi(k)$ . Each of the surface transmitters, however, will have the same clock skew, and due to the periodic corrections by the GPS clock, this value can be assumed approximately 0 for any period  $k$ . Thus, each transmission time can be represented as

$$\hat{t}_n = t_n + b + \phi(k) + w_n, \quad n = 1, \dots, N, \quad (7)$$

and again, by taking the difference of the time-of-arrival estimates, this common clock skew is eliminated from the timing estimate.

Next, we present the localization methods based on the exhaustive search and least-squares formulations.

**4.1. Exhaustive Search.** The individual time estimates  $\hat{t}_n$  generally have correlated noise in the underwater channel. For simplicity, we assume instead that they are independent and identically distributed (i.i.d.) and pursue a maximum likelihood function

$$\min_{x_r, y_r, z_r} f(x_r, y_r, z_r) = \sum_{n=2}^N [c \Delta \hat{t}_{n1} - (d_n - d_1)]^2. \quad (8)$$

The solution to (8) is found by exhaustive search.

In subtracting a common random variable,  $\hat{t}_1$ , from all subsequent TOA estimates, we are correlating each measurement by a factor of approximately 1/2. As such, assuming again i.i.d. measurements, a differencing measurement bias modification can be made as follows:

$$\min_{x_r, y_r, z_r} f(x_r, y_r, z_r) = (\hat{c} \mathbf{t}_\Delta - \mathbf{d}_\Delta)^T \Sigma^{-1} (\hat{c} \mathbf{t}_\Delta - \mathbf{d}_\Delta)^T, \quad (9)$$

where

$$\hat{\mathbf{t}}_\Delta = \begin{bmatrix} \Delta \hat{t}_{21} \\ \Delta \hat{t}_{31} \\ \vdots \\ \Delta \hat{t}_{n1} \end{bmatrix}, \quad \mathbf{d}_\Delta = \begin{bmatrix} d_2 - d_1 \\ d_3 - d_1 \\ \vdots \\ d_n - d_1 \end{bmatrix}, \quad (10)$$

and  $\Sigma$  is an  $(N-1) \times (N-1)$  normalized covariance matrix

$$\Sigma = \begin{bmatrix} 1 & \frac{1}{2} & \frac{1}{2} & \cdots & \frac{1}{2} \\ \frac{1}{2} & 1 & \frac{1}{2} & \cdots & \frac{1}{2} \\ \vdots & \vdots & \vdots & \cdots & \vdots \\ \frac{1}{2} & \frac{1}{2} & \frac{1}{2} & \cdots & 1 \end{bmatrix}. \quad (11)$$

**4.2. Least-Squares Solution.** We use the least-squares solution from [20]. Since  $d_n = d_{n1} + d_1$ , we have

$$(d_{n1} + d_1)^2 = x_n^2 + y_n^2 + z_n^2 - 2x_n x_r - 2y_n y_r - 2z_n z_r + d_1^2, \quad (12)$$

which can be simplified as

$$x_n x_r + y_n y_r + z_n z_r = \frac{1}{2} ([x_n^2 + y_n^2 + z_n^2 - d_{n1}^2]) - d_{n1} d_1. \quad (13)$$

Define the following matrix and vectors:

$$\mathbf{H} = \begin{bmatrix} x_2 & y_2 & z_2 \\ x_3 & y_3 & z_3 \\ \vdots & \vdots & \vdots \\ x_N & y_N & z_N \end{bmatrix}, \quad \mathbf{v} = \begin{pmatrix} -\hat{d}_{21} \\ -\hat{d}_{31} \\ \vdots \\ -\hat{d}_{N1} \end{pmatrix}, \quad (14)$$

$$\mathbf{u} = \frac{1}{2} \begin{bmatrix} x_2^2 + y_2^2 + z_2^2 - \hat{d}_{21}^2 \\ x_3^2 + y_3^2 + z_3^2 - \hat{d}_{31}^2 \\ \vdots \\ x_N^2 + y_N^2 + z_N^2 - \hat{d}_{N1}^2 \end{bmatrix}, \quad \mathbf{a} = \begin{bmatrix} x_r \\ y_r \\ z_r \end{bmatrix}.$$

The least-squares solution can be obtained as

$$\hat{\mathbf{a}} = d_1 \mathbf{H}^\dagger \mathbf{v} + \mathbf{H}^\dagger \mathbf{u}, \quad (15)$$

where  $^\dagger$  stands for pseudoinverse. Substituting the entries of into (2) yields a quadratic equation for  $d_1$  [20]. Solving for  $d_1$  and substituting the positive root back into (15) provides the final solution for the receiver position  $\mathbf{a}$ . We compare this LS solution with our exhaustive search in Figure 4, where timing error was assumed Gaussian distributed with zero mean and a varied standard deviation.

## 5. Tracking Algorithms

To further reduce the localization error from a single-point measurement, tracking algorithms can be implemented to combine the knowledge of multiple measurements into a more accurate position estimate.

In deciding which tracking approach would be best, we first consider the scenarios in which the node is being localized. There are two distinct modes in which underwater nodes typically move: either passively, with the water currents as a free-floating node, or actively as an underwater vehicle such as an AUV. Both are characterized primarily by long periods of relatively straight motion at a fairly constant speed. Typically, AUV motion differs in that at certain random intervals, it will change direction according to operator or preprogrammed instruction. Most search patterns for AUVs are defined by spiral paths, or by rectangular search grids. In either case, the vehicle is likely to alter its direction by way of a continuous turn; that is, to make a turn at a fixed angular velocity until the desired heading is achieved (or in the case of a spiral, until the search area is exhausted).

**5.1. Kalman Filter.** For simple motion models, characterized by long periods of motion free from maneuvers, a Kalman filter is the best linear state estimator for a Gaussian initial state assumption [24].

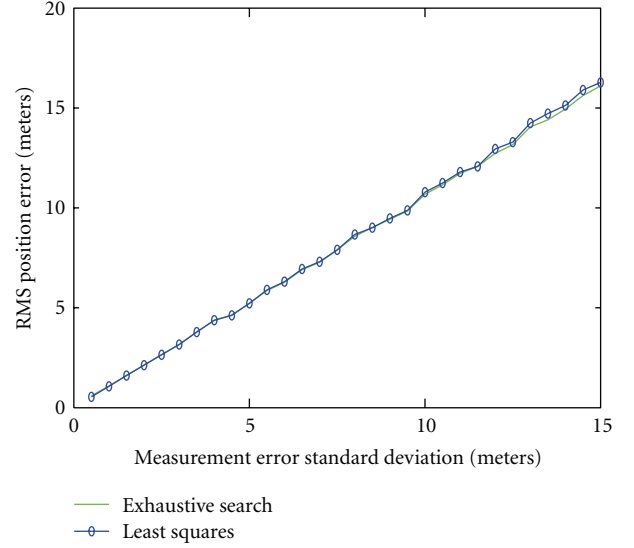


FIGURE 4: Root-mean-squared (RMS) localization error as a function of the standard deviation of the distance measurements. (Two curves overlap and are not easily distinguishable).

In the KF, we choose to model the movement of the node as set of discrete white noise acceleration (“kinematic”) models [24], with a separate model for each possible direction, that is,  $x$ ,  $y$ , and  $z$ . As such, the state equation for the Kalman filter at time index  $k + 1$  based on information from time step  $k$  becomes

$$L(k+1) = \mathbf{F}(k)L(k) + v(k), \quad (16)$$

with measurement

$$z(k+1) = \mathbf{H}(k+1)L(k+1) + w(k+1), \quad (17)$$

where

$$\mathbf{F}(k) = \begin{bmatrix} 1 & \tau & 0 & 0 & 0 & 0 \\ 0 & 1 & 0 & 0 & 0 & 0 \\ 0 & 0 & 1 & \tau & 0 & 0 \\ 0 & 0 & 0 & 1 & 0 & 0 \\ 0 & 0 & 0 & 0 & 1 & \tau \\ 0 & 0 & 0 & 0 & 0 & 1 \end{bmatrix}, \quad (18)$$

$$\mathbf{H}(k+1) = \begin{bmatrix} 1 & 0 & 0 & 0 & 0 & 0 \\ 0 & 0 & 1 & 0 & 0 & 0 \\ 0 & 0 & 0 & 0 & 1 & 0 \end{bmatrix}, \quad (19)$$

$v(k)$  is process noise,  $w(k)$  is measurement noise, and  $\tau$  is the sampling interval of the discrete model in seconds.

The state covariance is modeled as

$$\mathbf{P}(k+1 | k) = \mathbf{F}(k)\mathbf{P}(k | k)\mathbf{F}(k)^T + \mathbf{Q}(k). \quad (20)$$

The corresponding process noise has a covariance given as

$$\mathbf{Q} = \begin{bmatrix} \frac{1}{4}\tau^4 & \frac{1}{2}\tau^3 & 0 & 0 & 0 & 0 \\ \frac{1}{2}\tau^3 & \tau^2 & 0 & 0 & 0 & 0 \\ 0 & 0 & \frac{1}{4}\tau^4 & \frac{1}{2}\tau^3 & 0 & 0 \\ 0 & 0 & \frac{1}{2}\tau^3 & \tau^2 & 0 & 0 \\ 0 & 0 & 0 & 0 & \frac{1}{4}\tau^4 & \frac{1}{2}\tau^3 \\ 0 & 0 & 0 & 0 & \frac{1}{2}\tau^3 & \tau^2 \end{bmatrix} \sigma_v^2. \quad (21)$$

Here,  $\sigma_v$  is a design parameter that is chosen to match the most likely level of process noise to be experienced by the object in question, which is to say it controls how much the model anticipates the object to maneuver. Given that the object in question is likely to be either stationary or altering its velocity at a slow, steady rate, a process noise level of  $\sigma_v = 0.5 \text{ m/s}^2$  was selected to best emulate this behavior. The filter was initialized with two-point differencing [24].

**5.2. Probabilistic Data Association Filter.** During analysis of the performance of the KF, it became apparent that within a tracking window, there were point estimates which would appear as outliers by a considerable margin. On closer inspection, it was found that these were likely the result of one or more transmissions during which the direct-path signal propagation had been blocked, and a bounce was instead detected and treated as the direct path. Due to the assumption implicit to the KF approach that all of our messages are the direct-path propagation, this resulted in a drastic alteration of the point estimate, to the point where it could be classified as a false measurement. In that context, the probabilistic data association filter (PDAF) offers an improved performance over the standard KF, by allowing outlier estimates such as these to be ignored as false-alarm or clutter detections [25]. The PDAF is very similar to the KF in terms of state equations, presented here for measurement  $k + 1$ :

$$L(k + 1) = \mathbf{F}(k)L(k) + \nu(k), \quad (22)$$

with measurement

$$z(k + 1) = \mathbf{H}(k + 1)L(k + 1) + w(k + 1), \quad (23)$$

where  $\mathbf{F}(k)$  and  $\mathbf{H}(k + 1)$  are given in (18) and (19), respectively.

The state covariance is modeled similarly as

$$\mathbf{P}(k + 1 | k) = \mathbf{F}(k)\mathbf{P}(k | k)\mathbf{F}(k)^T + \mathbf{Q}(k). \quad (24)$$

The difference is on how to compute  $\mathbf{P}(k | k)$ . First, let  $P_D$  denote the probability of detection, which is a design parameter. Operating under the assumption that the measurement is always gated, define

$$b = 2 \left( \frac{1 - P_D}{P_D} \right). \quad (25)$$

Define the following variables and matrices:

$$\begin{aligned} \nu(k) &= z(k) - \mathbf{H}(k)L(k), \\ e(k) &= e^{-(1/2)\nu(k)^T \mathbf{S}(k)^{-1} \nu(k)}, \\ \mathbf{S}(k) &= \mathbf{H}(k)\mathbf{P}(k | k - 1)\mathbf{H}(k)^T + \mathbf{R}, \\ \mathbf{W}(k) &= \mathbf{P}(k | k - 1)\mathbf{H}(k)^T \mathbf{S}(k)^{-1}, \end{aligned} \quad (26)$$

where  $\mathbf{R}$  is the observation noise covariance. The probability of no correct measurement available is

$$\beta_0(k) = \frac{b}{b + e(k)}. \quad (27)$$

The probability of a correct measurement is

$$\beta_1(k) = \frac{e(k)}{b + e(k)}. \quad (28)$$

Further defining

$$\begin{aligned} \mathbf{P}^c(k | k) &= \mathbf{P}(k | k - 1) - \mathbf{W}(k)\mathbf{S}(k)\mathbf{W}(k)^T, \\ \tilde{\mathbf{P}}(k) &= \mathbf{W}(k) \left( \beta_1(k)\nu(k)\nu(k)^T - \nu(k)\nu(k)^T \right) \mathbf{W}(k)^T, \end{aligned} \quad (29)$$

the covariance matrix update is as follows:

$$\mathbf{P}(k | k) = \beta_0(k)\mathbf{P}(k | k - 1) + \beta_1(k)\mathbf{P}^c(k | k) + \tilde{\mathbf{P}}(k). \quad (30)$$

We are assuming that the measurement is always gated, and that there is only a single target and a single measurement at each time step. Accordingly, the  $P_D$  is then the probability that the current measurement is a valid estimate of the node being tracked. Based on experimental data, the number of “false detection” measurements was around 5% of the total samples, and so a value of 0.95 was selected for  $P_D$ .

**5.3. Interacting Multiple Model (IMM) Filter.** For the more complex motion of an active underwater node, an interacting multiple model filter (IMM) was implemented, as the expected maneuvering index of underwater vehicles can easily exceed the threshold for which a single linear filter is likely to have any benefit. To this end, the IMM was a simple two-model filter, with a single, linear, low process noise ( $\sigma_v = 0.05 \text{ m/s}^2$ ) KF to account for the straight motion travel, and an extended Kalman filter (EKF), configured in a coordinated-turn mode [26]. This validity of the coordinated turn assumption is dependent on the scenario in question,

though given the previously described search patterns, it should be sufficiently accurate [27].

The linear KF uses similar system equations as given previously, augmented with an additional column and row of zeros in order to accommodate the use of the EKF's additional state in the IMM. The EKF in this problem uses one of two sets of state equations: the first set is an approximation used when the predicted coordinated turn rate is near 0 ( $\hat{\Omega}(k) \approx 0$ ), and the second set is used when the predicted coordinated turn rate is greater than some detection threshold ( $|\hat{\Omega}(k)| > 0$ ) [24].

The first set of EKF state equation modifications ( $\hat{\Omega}(k) \approx 0$ ) is as follows:

$$L(k+1) = \mathbf{F}_L(k)L(k) + v(k), \quad (31)$$

where

$$\mathbf{F}_L(k) = \begin{bmatrix} 1 & \tau & 0 & 0 & 0 & 0 & -\frac{1}{2}\tau^2\hat{\eta}(k) \\ 0 & 1 & 0 & 0 & 0 & 0 & -\tau\hat{\eta}(k) \\ 0 & 0 & 1 & \tau & 0 & 0 & \frac{1}{2}\tau^2\hat{\xi}(k) \\ 0 & 0 & 0 & 1 & 0 & 0 & \tau\hat{\xi}(k) \\ 0 & 0 & 0 & 0 & 1 & \tau & 0 \\ 0 & 0 & 0 & 0 & 0 & 1 & 0 \\ 0 & 0 & 0 & 0 & 0 & 0 & 1 \end{bmatrix}, \quad (32)$$

where  $\eta$  and  $\xi$  represent the  $x$  and  $y$  directions, respectively, and we denote  $\hat{\eta}$  as the velocity component in the  $\eta$  direction. When  $|\hat{\Omega}(k)| > 0$ ,

$$\mathbf{F}_L(k) = \begin{bmatrix} 1 & \frac{\sin \hat{\Omega}(k)\tau}{\hat{\Omega}(k)} & 0 & -\frac{1-\cos \hat{\Omega}(k)\tau}{\hat{\Omega}(k)} & 0 & 0 & f_{\Omega,1(k)} \\ 0 & \cos \hat{\Omega}(k)\tau & 0 & -\sin \hat{\Omega}(k)\tau & 0 & 0 & f_{\Omega,2(k)} \\ 0 & \frac{1-\cos \hat{\Omega}(k)\tau}{\hat{\Omega}(k)} & 1 & \frac{\sin \hat{\Omega}(k)\tau}{\hat{\Omega}(k)} & 0 & 0 & f_{\Omega,3(k)} \\ 0 & \sin \hat{\Omega}(k)\tau & 0 & \cos \hat{\Omega}(k)\tau & 0 & 0 & f_{\Omega,4(k)} \\ 0 & 0 & 0 & 0 & 1 & \tau & 0 \\ 0 & 0 & 0 & 0 & 0 & 1 & 0 \\ 0 & 0 & 0 & 0 & 0 & 0 & 1 \end{bmatrix} \quad (33)$$

where the partial derivatives  $f_{\Omega,1(k)}, \dots, f_{\Omega,4(k)}$  are found as:

$$\begin{aligned} f_{\Omega,1(k)} &= \frac{(\cos \hat{\Omega}(k)\tau)\tau\hat{\xi}(k)}{\hat{\Omega}(k)} - \frac{(\sin \hat{\Omega}(k)\tau)\hat{\xi}(k)}{\hat{\Omega}(k)^2} \\ &\quad - \frac{(\sin \hat{\Omega}(k)\tau)\tau\hat{\eta}(k)}{\hat{\Omega}(k)} - \frac{(-1 + \cos \hat{\Omega}(k)\tau)\hat{\eta}(k)}{\hat{\Omega}(k)^2}, \\ f_{\Omega,2(k)} &= -(\sin \hat{\Omega}(k)\tau)\tau\hat{\xi}(k) - (\cos \hat{\Omega}(k)\tau)\tau\hat{\eta}(k), \\ f_{\Omega,3(k)} &= \frac{(\sin \hat{\Omega}(k)\tau)\tau\hat{\xi}(k)}{\hat{\Omega}(k)} - \frac{(1 - \cos \hat{\Omega}(k)\tau)\hat{\xi}(k)}{\hat{\Omega}(k)^2} \\ &\quad + \frac{(\cos \hat{\Omega}(k)\tau)\tau\hat{\eta}(k)}{\hat{\Omega}(k)} - \frac{(\sin \hat{\Omega}(k)\tau)\hat{\eta}(k)}{\hat{\Omega}(k)^2}, \\ f_{\Omega,4(k)} &= (\cos \hat{\Omega}(k)\tau)\tau\hat{\xi}(k) - (\sin \hat{\Omega}(k)\tau)\tau\hat{\eta}(k). \end{aligned} \quad (34)$$

In both cases, the process noise covariance is determined in the following state equations:

$$\mathbf{P}(k+1 | k) = \mathbf{F}_L(k)\mathbf{P}(k | k)\mathbf{F}_L(k)' + \Gamma_{\text{EKF}}\mathbf{Q}(k)\Gamma_{\text{EKF}}', \quad (35)$$

where

$$\Gamma_{\text{EKF}} = \begin{bmatrix} \frac{1}{2}\tau^2 & 0 & 0 & 0 \\ \tau & 0 & 0 & 0 \\ 0 & \frac{1}{2}\tau^2 & 0 & 0 \\ 0 & \tau & 0 & 0 \\ 0 & 0 & \frac{1}{2}\tau^2 & 0 \\ 0 & 0 & \tau & 0 \\ 0 & 0 & 0 & \tau \end{bmatrix}. \quad (36)$$

From our assumptions of AUV motion, the value of  $\mathbf{Q}(k)$  was selected as:

$$\mathbf{Q}(k) = \begin{bmatrix} r_s & 0 & 0 & 0 \\ 0 & r_s & 0 & 0 \\ 0 & 0 & r_s & 0 \\ 0 & 0 & 0 & r_d \end{bmatrix}, \quad (37)$$

where  $r_s = (1.25 \text{ m/s}^2)^2$  and  $r_d = (0.3\pi/180 \text{ rad})^2$ .

The IMM-CT is outlined in Figure 5. It combines a set of filters (in this case a KF and EKF) and mixes the weighted previous state estimates to determine the current hypothesis of each of the filters. The linear KF is designed as described previously, whereas the nonlinear EKF has a different set of model selection parameters which define how it interprets large differences in the measurements. In particular, its covariance matrix describes how much variation is expected during a coordinated maneuver in terms of the angular velocity, represented as two directional speed components and a rate of angular change component.

**5.4. Computational Complexity.** For a Kalman filter, the computational complexity is approximately of  $O(n^3)$ , where

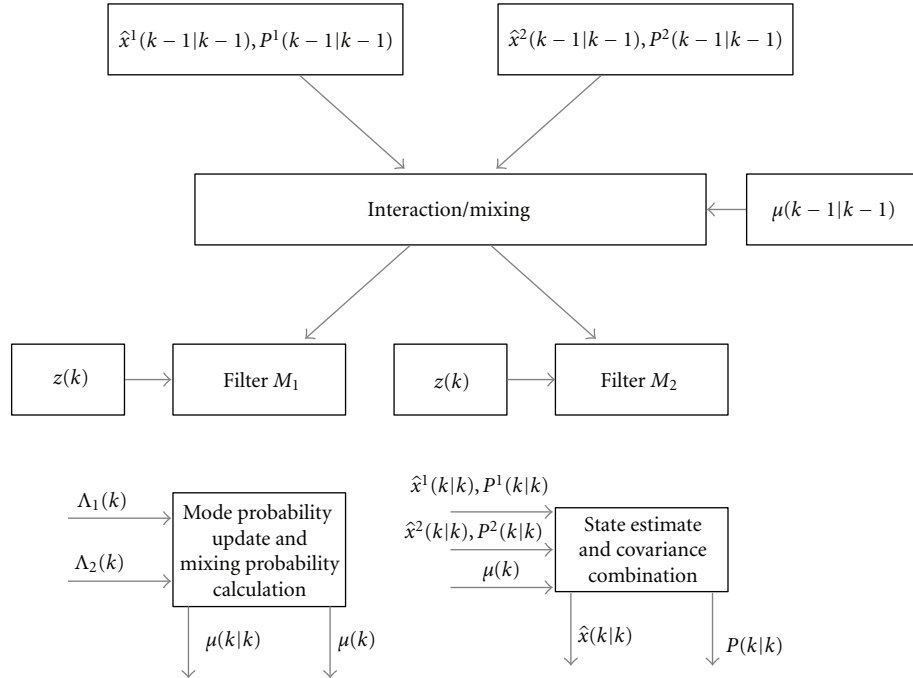


FIGURE 5: Outline of an interacting multiple-model filter.

$n = \max(n_x, n_z)$ ,  $n_x$  is the number of state variables, and  $n_z$  is the number of measurements [24]. It follows that the PDAF, having a similar number of calculations, is also nearly approximated by  $O(n^3)$ . The IMM-CT, which is dominated by the computation of multiple filters in parallel, is approximately  $O(pn^3)$ , where  $p$  is the number of filters used in the IMM which are not being processed in a parallel fashion.

## 6. Simulation Results

We first carry out simulations using a simple noise model to generate the TOA measurements and evaluate the localization accuracy. For simplicity,  $z$  is assumed to be known, and we only solve for  $x$  and  $y$  coordinates. Four transmitters are placed on a square grid with coordinates  $(0, 0)$ ,  $(100, 0)$ ,  $(0, 100)$ , and  $(100, 100)$ . One receiver is placed at the  $(0, 50)$  point and moves at a constant rate of 0.125 m/s parallel to the  $x$ -axis.

The TOAs are generated according to (3) where  $b$  is a fixed large bias, and  $w_n$  is i.i.d. zero-mean white Gaussian noise with standard deviation of 7.5 m. Position updates were taken every 16 seconds.

The localization position error is shown in Figure 6 as a function of total number of measurements acquired. We see that the Kalman filter clearly outperforms the point estimation based on exhaustive search (the LS solution has similar performance as the exhaustive search). We have also tested with a varied clock bias (not depicted), which had no effect upon the position error, as expected.

In addition to the Kalman filter, simulations for the proposed IMM-CT were also run, using the relatively

challenging scenario presented in Figure 7, with the corresponding RMS position error given by Figure 8. The dashed lines depicted in the figure indicate the beginning or end of one of the maneuvers from Figure 7. As can be seen in Figure 8, the point estimates are drastically improved by all three of the trackers, with the KF and PDAF slightly outperforming the IMM-CT on the straight-path portion after exiting a maneuver. There was no noticeable difference in the performance of the KF and PDAF, which is to be expected, as the scenario did not feature any indirect path propagations.

## 7. Pool Tests

We carried out tests in a standard competitive athletic swimming pool at The University of Connecticut, Storrs, whose dimensions are perfectly known. These tests did not use the GPS capabilities of the nodes, due to the limitation of the GPS receivers indoors. The nodes were fixed to the corner locations of the pool, such that their locations are measured accurately. The receiver was positioned approximately in the center of the pool, as outlined in Figure 9. All the transducers are placed about 1 m below the surface. The pool has a depth about 2 m. Stationary test was conducted during March 2010, while the mobile test was conducted during December 2010.

*7.1. Test Case 1 (Stationary Test, March 2010).* During the test, not all the messages from the transmitters were decoded correctly. For this reason, we use the data set with at least three measurements within one cycle of broadcasting from

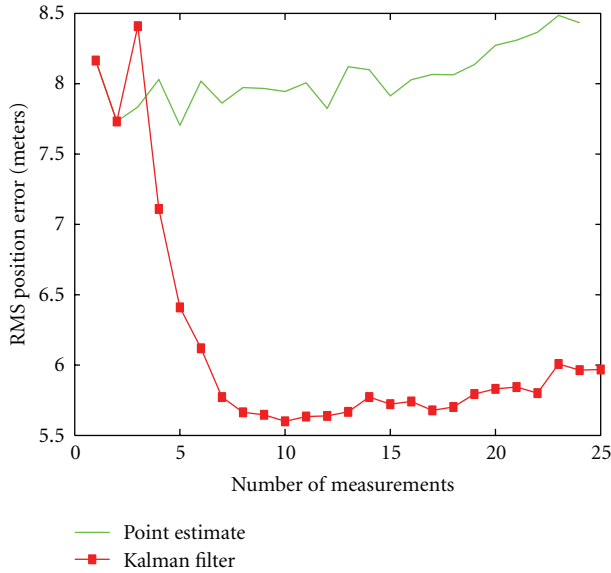


FIGURE 6: Root-mean-squared (RMS) localization error as a function of the number of measurements acquired as the receiver moved in a straight line.

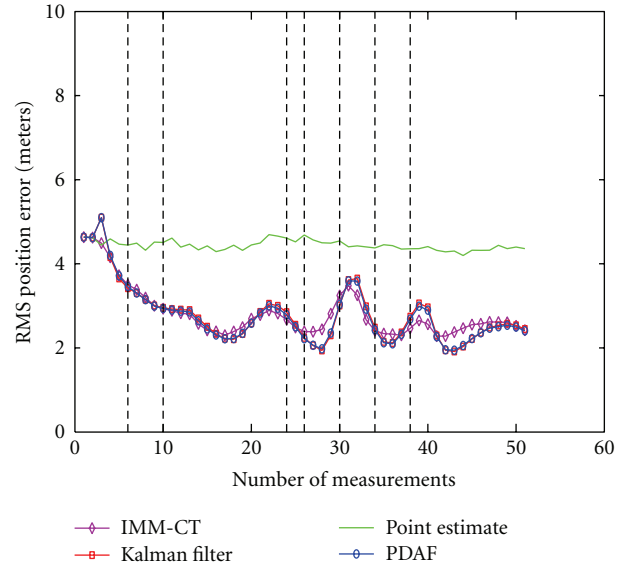


FIGURE 8: Root-mean-squared (RMS) localization error as a function of the number of measurements acquired as the receiver moved in the scenario.

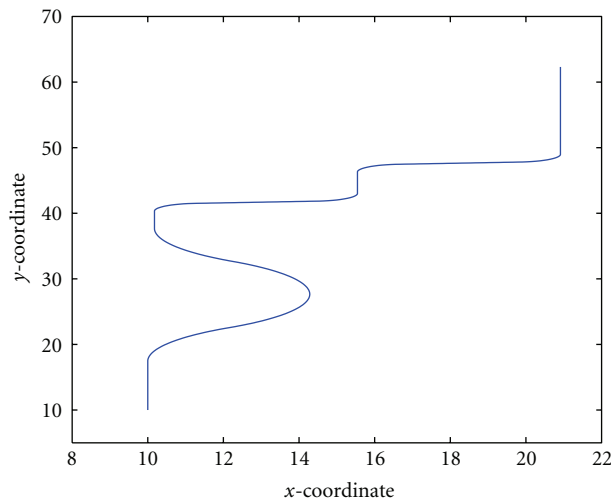


FIGURE 7: Simulation path for the IMM-CT, with distances in meters.

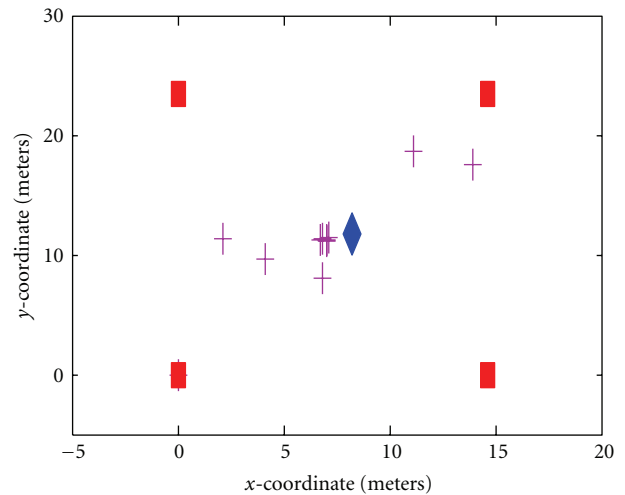


FIGURE 9: Node deployment during March 2010 pool test. The transmitters are denoted by squares, and the receiver is denoted by the diamond. The scattered plus signs are the estimates by the exhaustive search method.

the four surface nodes. The favorable geometry and the known value of  $z$  allow an estimate based on only three surface nodes. The location estimates by the exhaustive search method are shown in Figure 9, and those by the LS method are shown in Figure 10. We see that the LS estimates from these data sets are biased.

Although advanced algorithms could be applied to fuse the data from multiple data sets, here we simply average the location estimates from multiple data sets. As more data sets are available, the localization accuracy improves, as shown in Figure 11. A localization error of about 5 m is achieved with about 10 data sets.

7.2. *Test Case 2 (Mobile Test, December 2010)*. For the moving test in the pool, a simple straight-line maneuver was carried out. All of the previous conditions apply from the stationary pool test, including the use of only three nodes for localizing purposes. The scatter plot and approximate trajectory of the mobile node along with the four stationary transmitter locations are depicted in Figure 12. There was a significant upgrade in the hardware and software used for the second test, which resulted in a large reduction in the overall error, as can be seen in Figure 13. The high initial error of the Kalman filter can be attributed to the very low process noise of the filter, combined with a very bad initialization

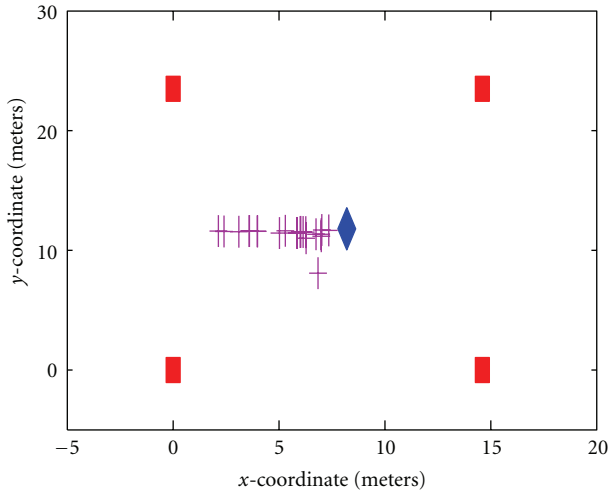


FIGURE 10: Node deployment during March 2010 pool test. The transmitters are denoted by squares, and the receiver is denoted by the diamond. The scattered plus signs are the estimates by the least-squares method.

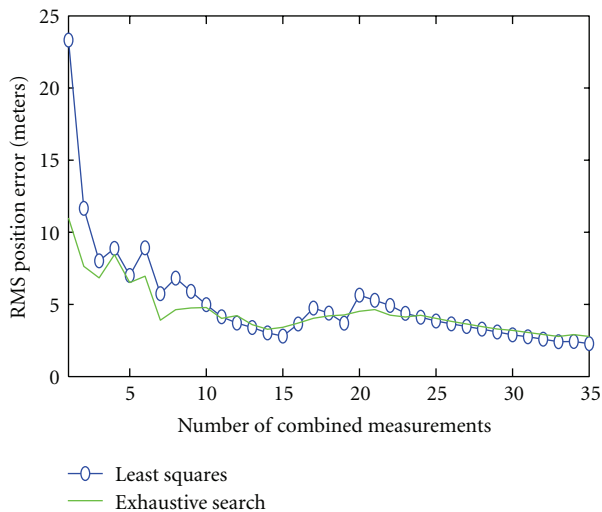


FIGURE 11: Localization error during March 2010 pool test.

which lead the filter to believe the node was traveling almost horizontally. Additionally, the measurements overall had a very low level of error, and the tracking system therefore could offer little improvement.

### 8. Field Test in a Local Lake

The lake testing was performed in Mansfield Hollow lake, located in Mansfield, CT during August 2011. The average depth of the area in which the testing occurred is approximately 2.5 m, with minor variations of approximately 0.5 m. During the test, wind speed was minimal, typically less than 5 mph. The nodes were positioned in a roughly square formation, with an average separation of 110 m, as depicted in Figure 14. The receiver was attached to a boat which would

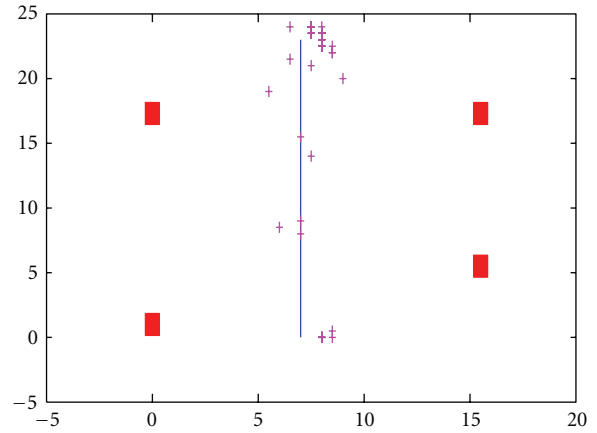


FIGURE 12: Localization error in the swimming pool.

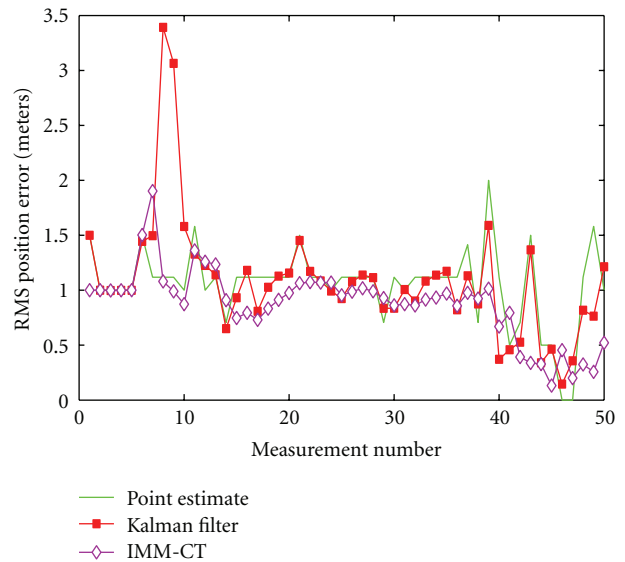


FIGURE 13: Localization error in the swimming pool.

freely float inside of this node formation for the duration of the testing.

For this test, the ground truth was determined via an onboard GPS device which would record the position of the receiver whenever a message was received. The data for a single run is presented, during which the boat moved at approximately 1 knot while moving along a slightly curved trajectory (approximately  $10^\circ$ ). Note, however, that at a certain point during the test, the ground-truth GPS stopped updating its position, while the boat continued to move. In order to correct for this, the remaining ground truth was extrapolated from the initial GPS measurements. This introduces a nonnegligible amount of uncertainty, but still enables conclusions to be drawn regarding the behavior of the tracking algorithms. The approximate trajectory and measurements of the boat along with relative node positions are depicted in Figure 15.



FIGURE 14: Approximate node deployment of August 2011 test via Google Maps.

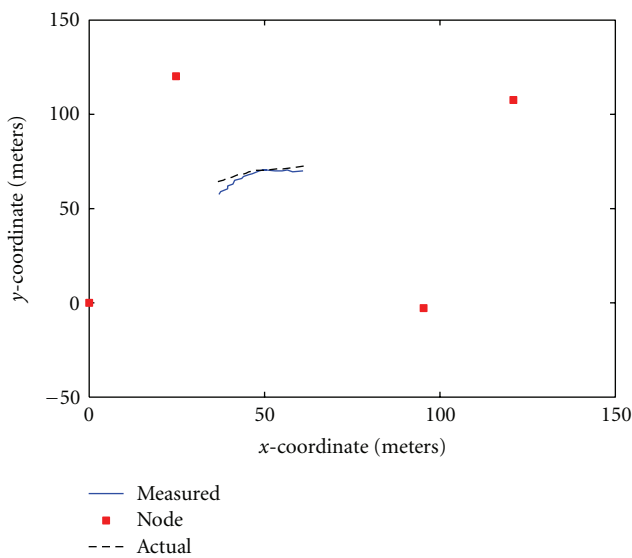


FIGURE 15: Plot of measurements and ground truth of lake test.

As can be seen in Figure 16, the tracking algorithms smooth the error out over the course of the maneuver and eventually reduce the overall error by a slight amount. Over the whole period, approximated error never exceeded a combined 5 m. While the raw measurements do exceed the trackers at one particular stretch, this is a combination of a rather small process noise coupled with a set of increasingly accurate measurements and is considered an acceptable trade-off due to the nature of node motion.

On inspection, the PDAF does not perform much better than the Kalman filter in most cases. There was one measurement where it clearly offered an improvement, but overall they did not differentiate much in performance. In almost all cases, the IMM-CT was superior to both filters.

## 9. Conclusion

In this paper, we presented an underwater localization solution based on one-way message broadcasting from multiple surface nodes. In addition to simulation results, we provided

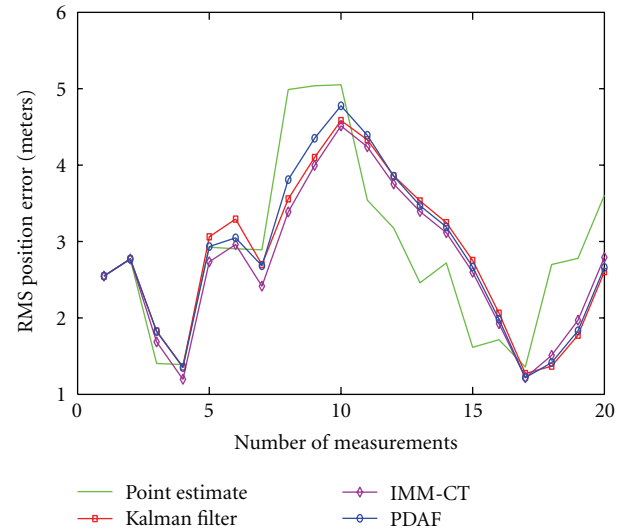


FIGURE 16: Localization error during second lake test.

testing results in a swimming pool and in a local lake. Future work would involve large-scale field tests featuring multiple nodes, as well as sea deployments over larger distances. Those will be pursued when there are suitable opportunities.

## Acknowledgments

This work was supported by the ONR Grant N00014-09-1-0704 (PECASE) and the NSF Grant CNS-0821597 (MRI). P. Carroll is supported by a GANNN Fellowship from the Department of Education.

## References

- [1] V. Chandrasekhar, W. K. G. Seah, Y. S. Choo, and H. V. Ee, "Localization in underwater sensor networks—survey and challenges," in *Proceedings of the ACM International Conference on Mobile Computing and Networking (MobiCom '06)*, pp. 33–40, New York, NY, USA, September 2006.
- [2] H. Tan, R. Diamant, W. Seah, and M. Waldmeyer, "A survey of techniques and challenges in underwater localization," *Ocean Engineering*, vol. 38, no. 14-15, pp. 1663–1676, 2011.
- [3] C. M. Lee, P. M. Lee, S. W. Hong, S. M. Kim, and W. Seong, "Underwater navigation system based on inertial sensor and doppler velocity log using indirect feedback Kalman filter," *International Journal of Offshore and Polar Engineering*, vol. 15, no. 2, pp. 88–95, 2005.
- [4] R. Hartman, W. Hawkinson, and K. Sweeney, "Tactical Underwater Navigation System (TUNS)," in *Proceedings of the IEEE/ION Position, Location and Navigation Symposium, PLANS*, pp. 898–911, Fairfax, Va, USA, May 2008.
- [5] R. Stuart, "Acoustic digital spread spectrum: an enabling technology," *Sea Technology*, vol. 46, no. 10, pp. 15–20, 2005.
- [6] A. Caiti, A. Garulli, F. Livide, and D. Prattichizzo, "Localization of autonomous underwater vehicles by floating acoustic buoys: a set-membership approach," *IEEE Journal of Oceanic Engineering*, vol. 30, no. 1, pp. 140–152, 2005.
- [7] C. Bechaz and H. Thomas, "GIB system: the underwater GPS solution," in *Proceedings of the ECUA*, May 2001.

- [8] Z. Zhou, J. H. Cui, and S. Zhou, "Efficient localization for large-scale underwater sensor networks," *Ad Hoc Networks*, vol. 8, no. 3, pp. 267–279, 2010.
- [9] M. Erol-Kantarci, H. T. Mouftah, and S. Oktug, "Localization techniques for underwater acoustic sensor networks," *IEEE Communications Magazine*, vol. 48, no. 12, pp. 152–158, 2010.
- [10] D. Mirza and C. Schurgers, "Motion-aware self-localization for underwater networks," in *Proceedings of the ACM International Conference on Mobile Computing and Networking (MobiCom '08)*, pp. 51–58, San Francisco, Calif, USA, September 2008.
- [11] M. T. Isik and O. B. Akan, "A three dimensional localization algorithm for underwater acoustic sensor networks," *IEEE Transactions on Wireless Communications*, vol. 8, no. 9, pp. 4457–4463, 2009.
- [12] R. M. Eustice, L. L. Whitcomb, H. Singh, and M. Grund, "Experimental results in synchronous-clock one-way-travel-time acoustic navigation for autonomous underwater vehicles," in *Proceedings of the IEEE International Conference on Robotics and Automation (ICRA '07)*, pp. 4257–4264, April 2007.
- [13] S. E. Webster, R. M. Eustice, H. Singh, and L. L. Whitcomb, "Preliminary deep water results in single-beacon one-way-travel-time acoustic navigation for underwater vehicles," in *Proceedings of the IEEE/RSJ International Conference on Intelligent Robots and Systems (IROS '09)*, pp. 2053–2060, October 2009.
- [14] R. Diamant and L. Lampe, "Underwater localization with time-synchronization and propagation speed uncertainties," in *Proceedings of the 8th Workshop on Positioning Navigation and Communication (WPNC '11)*, April 2011.
- [15] X. Tan and J. Li, "Cooperative positioning in underwater sensor networks," *IEEE Transactions on Signal Processing*, vol. 58, no. 11, pp. 5860–5871, 2010.
- [16] W. Cheng, A. Y. Teymorian, L. Ma, X. Cheng, X. Lu, and Z. Lu, "Underwater localization in sparse 3D acoustic sensor networks," in *Proceedings of the 27th IEEE Communications Society Conference on Computer Communications (INFOCOM '08)*, pp. 798–806, April 2008.
- [17] X. Cheng, H. Shu, Q. Liang, and D. H. C. Du, "Silent positioning in underwater acoustic sensor networks," *IEEE Transactions on Vehicular Technology*, vol. 57, no. 3, pp. 1756–1766, 2008.
- [18] L. F. M. Vieira, U. Lee, and M. Gerla, "Phero-trail: a bio-inspired location service for mobile underwater sensor networks," *IEEE Journal on Selected Areas in Communications*, vol. 28, no. 4, pp. 553–563, 2010.
- [19] M. Erol-Kantarci, S. Oktug, L. Vieira, and M. Gerla, "Performance evaluation of distributed localization techniques for mobile underwater acoustic sensor networks," *Ad Hoc Networks*, vol. 9, no. 1, pp. 61–72, 2011.
- [20] G. Mellen, M. Pachter, and J. Raquet, "Closed-form solution for determining emitter location using time difference of arrival measurements," *IEEE Transactions on Aerospace and Electronic Systems*, vol. 39, no. 3, pp. 1056–1058, 2003.
- [21] H. Yan, L. Wan, S. Zhou et al., "DSP based receiver implementation for OFDM acoustic modems," *Elsevier Journal on Physical Communication*, vol. 5, no. 1, pp. 22–32, 2012.
- [22] S. F. Mason, C. R. Berger, S. Zhou, and P. Willett, "Detection, synchronization, and doppler scale estimation with multicarrier waveforms in underwater acoustic communication," *IEEE Journal on Selected Areas in Communications*, vol. 26, no. 9, pp. 1638–1649, 2008.
- [23] D. A. Abraham and P. K. Willett, "Active sonar detection in shallow water using the page test," *IEEE Journal of Oceanic Engineering*, vol. 27, no. 1, pp. 35–46, 2002.
- [24] Y. Bar-Shalom, X. R. Li, and T. Kirubarajan, *Estimation with Applications to Tracking and Navigation*, John Wiley & Sons, New York, NY, USA, 2001.
- [25] Y. Bar-Shalom, P. Willett, and X. Tian, *Tracking and Data Fusion: A Handbook of Algorithms*, YBS Publishing, 2011.
- [26] H. Wang, T. Kirubarajan, and Y. Bar-Shalom, "Precision large scale air traffic surveillance using IMM/assignment estimators," *IEEE Transactions on Aerospace and Electronic Systems*, vol. 35, no. 1, pp. 255–266, 1999.
- [27] B. Ferreira, A. Matos, and N. Cruz, "Estimation approach for AUV navigation using a single acoustic beacon," *Sea Technology*, vol. 51, no. 12, pp. 54–58, 2010.

## Research Article

# Performance Comparison of Doppler Scale Estimation Methods for Underwater Acoustic OFDM

Lei Wan,<sup>1</sup> Zhaohui Wang,<sup>1</sup> Shengli Zhou,<sup>1</sup> T. C. Yang,<sup>2</sup> and Zhijie Shi<sup>3</sup>

<sup>1</sup>Department of Electrical and Computer Engineering, University of Connecticut, 371 Fairfield Way U-2157, Storrs, CT 06269, USA

<sup>2</sup>National Sun Yat-Sen University, Kaohsiung, Taiwan

<sup>3</sup>Department of Computer Science and Engineering, University of Connecticut, 371 Fairfield Way U-2155, Storrs, CT 06269, USA

Correspondence should be addressed to Shengli Zhou, shengli@engr.uconn.edu

Received 13 January 2012; Accepted 5 April 2012

Academic Editor: Charalampos C. Tsimenidis

Copyright © 2012 Lei Wan et al. This is an open access article distributed under the Creative Commons Attribution License, which permits unrestricted use, distribution, and reproduction in any medium, provided the original work is properly cited.

Doppler scale estimation is one critical step needed by the resampling operation in acoustic communication receivers. In this paper, we compare different Doppler scale estimation methods using either cyclic-prefixed (CP) or zero-padded (ZP) orthogonal-frequency division-multiplexing (OFDM) waveforms. For a CP-OFDM preamble, a self-correlation method allows for blind Doppler scale estimation based on an embedded repetition structure while a cross-correlation method is available with the knowledge of the waveform. For each received ZP-OFDM block, the existence of null subcarriers allows for blind Doppler scale estimation. In addition, a pilot-aided method and a decision-aided method are applicable based on cross-correlation with templates constructed from symbols on pilot subcarriers only and from symbols on all subcarriers after data decoding, respectively. This paper carries out extensive comparisons among these methods using both simulated and real experimental data. Further, the applicabilities of these methods to distributed multiuser systems are investigated.

## 1. Introduction

Underwater acoustic communications and networking have been under extensive investigation in recent years [1, 2]. Considerable progress on the physical layer communication techniques has been made for both single-carrier and multi-carrier communications; see, for example, [3–19]. Relative to the radio channel which has relative short delay spread and slow time variation, underwater acoustic channels typically exhibit long delay spread and fast time variation. The latter brings significant Doppler effects to underwater acoustic communication systems, hence estimation of the Doppler scaling factor is one key receiver module [4, 20, 21].

Typically, Doppler scale estimation is accomplished by inserting waveforms known to the receiver during the data transmission. Two popular approaches are described in the following.

- (i) One approach is to use a pulse train which is formed by the repetition of a *Doppler-insensitive waveform* [22], such as linear-frequency-modulated

(LFM) waveform [23] and hyperbolic-frequency-modulated (HFM) waveform [24]. A transmission format with one preamble and one postamble around the data burst is usually adopted [4, 20, 25], as shown in Figure 1. At the receiver side, by detecting the times-of-arrival of the preamble and postamble, thus the interval change in-between, an average Doppler scale estimate over the whole data burst can be obtained. Thanks to the Doppler-insensitivity property of the waveforms, a single-branch-matched filtering operation is adequate even in the presence of Doppler distortion. However, this method is only suitable for offline processing due to the processing delay.

- (ii) The other approach is to use a *Doppler-sensitive waveform with a thumb-tack ambiguity function*. A Doppler-sensitive waveform is usually transmitted as a preamble prior to the data burst, as shown in Figure 1. At the receiver side, a bank of correlators correlates the received signal with preambles prescaled by different Doppler scaling factors, and the branch with the largest correlation peak provides

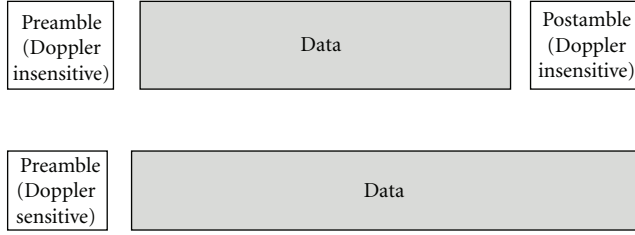


FIGURE 1: Top: Doppler scale estimation with Doppler-insensitive waveforms. Bottom: Doppler scale estimation with Doppler-sensitive waveforms.

the estimated Doppler scale [25]. Typical Doppler-sensitive waveforms include Costa waveforms [26], m-sequence [27], and poly-phase sequence [28].

In this paper, we focus on an underwater acoustic communication system using zero-padded orthogonal-frequency division-multiplexing modulation (ZP-OFDM), in which pilot subcarriers and null subcarriers are usually multiplexed with data subcarriers for channel estimation and residual Doppler shift mitigation, respectively [4]. A cyclic prefixed (CP) OFDM preamble is inserted prior to data transmission for detection, synchronization, and Doppler scale estimation [29]. This transmission format, as shown in Figure 2, has been implemented on DSP-based OFDM modem prototypes [30].

By exploiting the cyclic repetition structure of the CP-OFDM preamble, a blind estimation with a bank of self-correlators was proposed in [29]. However, it does not leverage the knowledge of the waveform itself which is known to the receiver. Taking this method as the first approach, one can easily construct the following Doppler scale estimators for the OFDM transmission in Figure 2.

- (i) *Cross-correlation with the CP-OFDM Preamble*: Given the Doppler sensitivity of the OFDM waveform, a bank of cross-correlators can use the prescaled versions of the CP-OFDM waveform as local replicas.
- (ii) *Pilot-Aided Method for Each ZP-OFDM Block*: By taking the waveform constituted by the pilot-subcarrier components as a replica of the transmitted signal, the Doppler estimation method using a bank of cross-correlators is directly applicable.
- (iii) *Null-Subcarrier Based Blind Estimation Method for Each ZP-OFDM Block*: As an extension of the blind carrier frequency offset (CFO) estimation method [31], the receiver rescales the received waveform with different tentative Doppler scaling factors and uses the energy on the null subcarriers to find the best fit.
- (iv) *Decision-Aided Method for Each ZP-OFDM Block*: Once a ZP-OFDM block is successfully decoded, the transmitted waveform corresponding to this block can be reconstructed at the receiver. Taking the reconstructed waveform as a local replica, the Doppler estimation method using a bank of correlators can be deployed to refine the Doppler scale estimation for

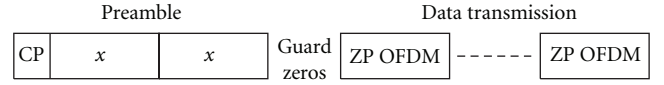


FIGURE 2: The data burst structure considered in this paper, which consists of a special CP-OFDM preamble and multiple ZP-OFDM blocks.

this block. The refined Doppler scale estimate can be passed to the next block.

The contributions of this paper are the following.

- (i) We carry out extensive performance comparisons among the aforementioned Doppler estimation methods. Specifically, we focus on the OFDM transmission format in Figure 2 in single-user transmissions. Both simulations and experimental results reveal that the correlation-based methods have a decent performance in the low SNR region, and the blind estimation methods can catch up or even outperform the correlation methods in the high SNR region. As a performance benchmark, the Cramer-Rao lower bound (CRLB) is also included for single-path channels.
- (ii) We extend our investigation to a multiuser OFDM setting, where different users could have different Doppler scaling factors [32]. Simulation results show that the correlation-based methods are robust to the multiuser interference, while the blind method suffers severe performance degradation.

The rest of this paper is as follows. Different Doppler scale estimation methods for CP-OFDM and ZP-OFDM waveforms are presented in Sections 2 and 3, respectively. Simulation results of these methods are provided in Section 4, and experimental results are provided in Section 5. Extension to the multiuser scenario is described in Section 6. Conclusions are contained in Section 7.

## 2. Doppler Scale Estimation with a CP-OFDM Preamble

Consider a CP-OFDM preamble structure in Figure 2, which consists of two identical OFDM symbols of length  $T_0$  and a cyclic prefix of length  $T_{cp}$  in front, with the embedded structure

$$x_{cp}(t) = x_{cp}(t + T_0), \quad -T_{cp} \leq t \leq T_0. \quad (1)$$

Let  $B$  denote the system bandwidth, and define  $K_0 := BT_0$  as the number of subcarriers. The baseband CP-OFDM signal is

$$x_{cp}(t) = \sum_{k=-K_0/2}^{K_0/2-1} d[k] e^{j2\pi(k/2T_0)t} q(t), \quad t \in [-T_{cp}, 2T_0], \quad (2)$$

where  $d[k]$  is the transmitted symbol on the  $k$ th subcarrier, and  $q(t)$  is a pulse shaping window,

$$q(t) = \begin{cases} 1, & t \in [-T_{\text{cp}}, 2T_0]. \\ 0, & \text{elsewhere.} \end{cases} \quad (3)$$

The passband signal can be obtained as  $\tilde{x}_{\text{cp}}(t) = 2 \operatorname{Re}\{x_{\text{cp}}(t)e^{j2\pi f_c t}\}$ , where  $f_c$  is the center frequency.

Consider a multipath channel which consists of  $N_{\text{pa}}$  paths

$$h(t; \tau) = \sum_{p=1}^{N_{\text{pa}}} A_p(t) \delta(t - \tau_p(t)), \quad (4)$$

where  $A_p(t)$  and  $\tau_p(t)$  denote the amplitude and delay of the  $p$ th path, respectively. Throughout this paper, we assume that the amplitude is constant within each OFDM block (about 200 ms for the system considered in this paper), that is,  $A_p(t) \approx A_p$ , which leads to

$$h(t; \tau) = \sum_{p=1}^{N_{\text{pa}}} A_p \delta(t - \tau_p(t)). \quad (5)$$

After transmitting the passband signal  $\tilde{x}_{\text{cp}}(t)$  through the multipath channel, the received passband signal  $\tilde{y}(t)$  is converted to baseband as  $y(t) = \text{LPF}(\tilde{y}(t)e^{-j2\pi f_c t})$ , where LPF denotes the low pass filtering operation.

**2.1. Self-Correlation.** If all the paths in the channel have the same Doppler scale factor

$$\tau_p(t) = \tau_p - at, \quad (6)$$

it is shown in [29] that the embedded structure in the received waveform becomes

$$y(t) = e^{-j2\pi(a/(1+a))f_c T_0} y\left(t + \frac{T_0}{1+a}\right), \quad (7)$$

$$-\frac{T_{\text{cp}} - \tau_{\text{max}}}{1+a} \leq t \leq \frac{T_0}{1+a},$$

which has a repetition period  $T_0/(1+a)$  regardless of the channel amplitudes.

By exploiting the structure in (7), the time-of-arrival and the Doppler scale of the CP-OFDM symbol in the received signal can be jointly estimated via

$$(\hat{a}, \hat{\tau}) = \arg \max_{a, \tau} \left| \int_0^{T_0/(1+a)} y(t + \tau) y^*\left(t + \tau + \frac{T_0}{1+a}\right) dt \right|, \quad (8)$$

which does not require the knowledge of the channel and the data symbols. This method can be implemented with a bank of self-correlators [29].

**2.2. Cross-Correlation.** Rather than exploiting the structure of the CP-OFDM preamble, the cross-correlation-based method can be used, since the transmitted preamble is known at the receiver. Taking the basic unit of duration  $T_0$

as the template, the joint time-of-arrival and Doppler rate estimation can be achieved via

$$(\hat{a}, \hat{\tau}) = \arg \max_{a, \tau} \left| \int_0^{T_0} y(t + \tau) x_{\text{cp}}^*((1+a)t) e^{-j2\pi a f_c t} dt \right|. \quad (9)$$

This can be implemented via a bank of cross-correlators, where the branch yielding the largest peak provides the needed Doppler scale estimate.

### 3. Doppler Scale Estimation with Each ZP-OFDM Block

As described in [4], a ZP-OFDM signal design multiplexing pilot and null subcarriers with data subcarriers can effectively deal with fast channel variations. Assume that the ZP-OFDM system has  $K$  subcarriers. Let  $T$  denote the symbol duration and  $T_g$  the guard interval. The total OFDM block duration is thus  $T_{\text{bl}} := T + T_g$ . Denote  $\mathcal{S}_D$ ,  $\mathcal{S}_P$ ,  $\mathcal{S}_N$  as the nonoverlapped sets formed by the data subcarriers, pilot subcarriers, and null subcarriers, respectively, which satisfy  $\mathcal{S}_D \cup \mathcal{S}_P \cup \mathcal{S}_N = \{-K/2, \dots, K/2 - 1\}$ . The baseband transmitted ZP-OFDM signal can be expressed by

$$x_{\text{zp}}(t) = \sum_{k \in \mathcal{S}_D \cup \mathcal{S}_P} d[k] e^{j2\pi(k/T)t} g(t), \quad t \in [0, T_{\text{bl}}], \quad (10)$$

where  $g(t)$  describes the zero-padding operation, that is,

$$g(t) = \begin{cases} 1, & t \in [0, T], \\ 0, & \text{elsewhere.} \end{cases} \quad (11)$$

After transmitting the ZP-OFDM symbol through a multipath channel defined in (5), we denote  $\tilde{y}(t)$  as the received passband signal, whose baseband version is  $y(t) = \text{LPF}(\tilde{y}(t)e^{-j2\pi f_c t})$ . The availability of null subcarriers, pilot subcarriers, and data subcarriers can be used for Doppler scale estimation.

**3.1. Null-Subcarrier-Based Blind Estimation.** In [29], the null subcarriers in ZP-OFDM system are exploited to perform carrier frequency offset (CFO) estimation. Here in this paper, the same principle is used to estimate Doppler scale factor.

Assume that coarse synchronization is available from the preamble. After truncating each ZP-OFDM block from the received signal, we resample one block with different tentative scaling factors. The total energy of frequency measurements at null subcarriers are used as a metric for the Doppler scale estimation

$$\hat{a} = \arg \min_a \sum_{k \in \mathcal{S}_N} \left| \int_0^{T+T_g} y\left(\frac{t}{1+a}\right) e^{-j2\pi a f_c t} e^{-j2\pi(k/T)t} dt \right|^2. \quad (12)$$

For each tentative  $a$ , a resampling operation is carried out followed by fast Fourier transform. A one-dimensional grid search leads to a Doppler scale estimate.

3.2. *Pilot-Aided Estimation.* As introduced above, a set of subcarriers  $\mathcal{S}_p$  is dedicated to transmit pilot symbols. Hence, the transmitted waveform  $x_{zp}(t)$  is partially known, containing

$$x_{\text{pilot}}(t) = \sum_{k \in \mathcal{S}_p} d[k] e^{j2\pi(k/T)t} g(t), \quad t \in [0, T]. \quad (13)$$

The joint time-of-arrival and Doppler scale estimation is achieved via

$$\begin{aligned} & (\hat{a}, \hat{\tau}) \\ &= \arg \max_{a, \tau} \left| \int_0^{T/(1+a)} y(t + \tau) x_{\text{pilot}}^*((1+a)t - \tau) e^{-j2\pi a f_c t} dt \right|, \end{aligned} \quad (14)$$

which can be implemented via a bank of cross-correlators.

3.3. *Decision-Aided Estimation.* For an OFDM transmission with multiple blocks, the Doppler estimated in one block can be used for the resampling operation of the next block assuming small Doppler variation across blocks. After the decoding operation the receiver can reconstruct the transmitted time-domain waveform, by replacing  $d[k]$  by its estimate  $\hat{d}[k]$ , for all  $k \in \mathcal{S}_D$  in. Denote the reconstructed waveform as  $\hat{x}_{zp}(t)$ .

Similar to the pilot-aided method, the decision-aided method performs the joint time-of-arrival and Doppler scale estimation via

$$\begin{aligned} & (\hat{a}, \hat{\tau}) \\ &= \arg \max_{a, \tau} \left| \int_0^{T/(1+a)} y(t + \tau) \hat{x}_{zp}^*((1+a)t - \tau) e^{-j2\pi a f_c t} dt \right|, \end{aligned} \quad (15)$$

which again is implemented via a bank of cross-correlators. The estimated  $\hat{a}$  can be used for the resampling operation of the next block.

*Remark 1.* Relative to the pilot-aided method, the decision-aided method leverages the estimated information symbols, thus is expected to achieve a better estimation performance. Assuming that all the information symbols have been successfully decoded, the decision-aided method has knowledge about both the data and pilot symbols. Let  $|\mathcal{S}_p|$  and  $|\mathcal{S}_D|$  denote the numbers of pilot and data symbols, respectively. Using the template  $\hat{x}_{zp}(t)$  constructed from  $(|\mathcal{S}_p| + |\mathcal{S}_D|)$  known symbols for cross correlation achieve a  $10 \log_{10}((|\mathcal{S}_p| + |\mathcal{S}_D|)/|\mathcal{S}_p|)$  dB power gain in terms of noise reduction, relative to that using the template  $x_{\text{pilot}}(t)$  constructed from  $|\mathcal{S}_p|$  known symbols.

## 4. Simulation Results

The OFDM parameters are summarized in Table 1. For CP-OFDM, the data symbols at all the 512 subcarriers are randomly drawn from a QPSK constellation. For ZP-OFDM, out of 1024 subcarriers, there are  $|\mathcal{S}_N| = 96$  null subcarriers with 24 on each edge of the signal band for band protection

TABLE 1: OFDM parameters in simulations.

System parameters	CP-OFDM	ZP-OFDM
Center frequency: $f_c$	13 kHz	13 kHz
Bandwidth: $B$	4.88 kHz	4.88 kHz
# of subcarriers:	$K_0 = 512$	$K = 1024$
Time duration:	$T_0 = 104.86$ ms	$T = 209.72$ ms
Guard interval:	$T_{\text{cp}} = 100$ ms	$T_g = 40.3$ ms

and 48 evenly distributed in the middle for the carrier frequency offset estimation;  $|\mathcal{S}_p| = 256$  are pilot subcarriers uniformly distributed among the 1024 subcarriers, and the remaining are  $|\mathcal{S}_D| = 672$  data subcarriers for delivering information symbols. The pilot symbols are drawn randomly from a QPSK constellation. The data symbols are encoded with a rate-1/2 nonbinary LDPC code [33] and modulated by a QPSK constellation.

Three UWA channel settings are tested.

(i) *Channel Setting 1:* A single-path channel:

$$h(t, \tau) = \delta(t - [\tau - at]). \quad (16)$$

(ii) *Channel Setting 2:* A multipath channel with  $N_{\text{pa}} = 15$  paths, where all paths have one common Doppler scaling factor:

$$h(t, \tau) = \sum_{p=1}^{N_{\text{pa}}} A_p \delta(t - [\tau_p - at]). \quad (17)$$

(iii) *Channel Setting 3:* A multipath channel with  $N_{\text{pa}} = 15$  paths, where each path has an individual Doppler scaling factor:

$$h(t, \tau) = \sum_{p=1}^{N_{\text{pa}}} A_p \delta(t - [\tau_p - a_p t]). \quad (18)$$

The interarrival time of paths follows an exponential distribution with a mean of 1 ms. The mean delay spread for the channels in and is thus 15 ms. The amplitudes of paths are Rayleigh distributed with the average power decreasing exponentially with the delay, where the difference between the beginning and the end of the guard time is 20 dB. For each path, the Doppler scale  $a_p$  is generated from a Doppler speed  $v_p$  (with unit m/s):

$$a_p = \frac{v_p}{c}, \quad (19)$$

where  $c = 1500$  m/s is the sound speed in water. In channel settings 1 and 2, the Doppler speed  $v$  is uniformly distributed within  $[-4.5, 4.5]$  m/s. In channel setting 3, the Doppler speeds  $\{v_p\}$  are randomly drawn from the interval  $[1.5 - 0.1, 1.5 + 0.1]$  m/s.

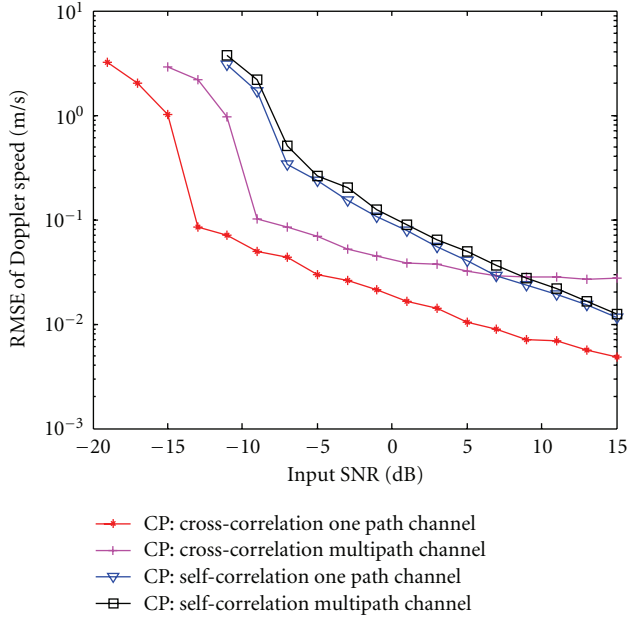


FIGURE 3: Performance of different estimators for the CP-OFDM preamble in single-path and multipath channels (channel settings 1 and 2).

In channel settings 1 and 2, the ground truths of  $\nu$  and  $a$  are known. We adopt the root-mean-squared-error (RMSE) of the estimated Doppler speed as the performance metric,

$$\text{RMSE} = \sqrt{E[|\hat{\nu} - \nu|^2]} = \sqrt{E[|(\hat{a} - a)c|^2]}, \quad (20)$$

which has the unit m/s. In channel setting 3, different paths have different Doppler scales, while the Doppler scale estimator only provides one estimate. RMSE is hence not well motivated. With the estimated Doppler scale to perform the resampling operation, we will use the block-error-rate (BLER) of the ZP-OFDM decoding as the performance metric.

**4.1. RMSE Performance with CP-OFDM.** For the single-path channel, Figure 3 shows the RMSE performance of two estimation methods at different SNR levels. One can see a considerable gap between the self-correlation method and the cross-correlation method, while in the medium to high SNR region, both methods can provide a reasonable performance to facilitate receiver decoding.

For the multipath channel with a single Doppler speed, Figure 3 shows the RMSE performance of two estimation methods. One can see that the cross-correlation method outperforms the self-correlation method considerably in the low SNR region. However, the former suffers an error floor in the high SNR region, while the later does not.

Relative to the RMSE performance in the single-path channel, a considerable performance degradation can be observed for the cross-correlation method in the multipath channel, whereas the performance of the self-correlation method is quite robust. The reason for the difference lies in

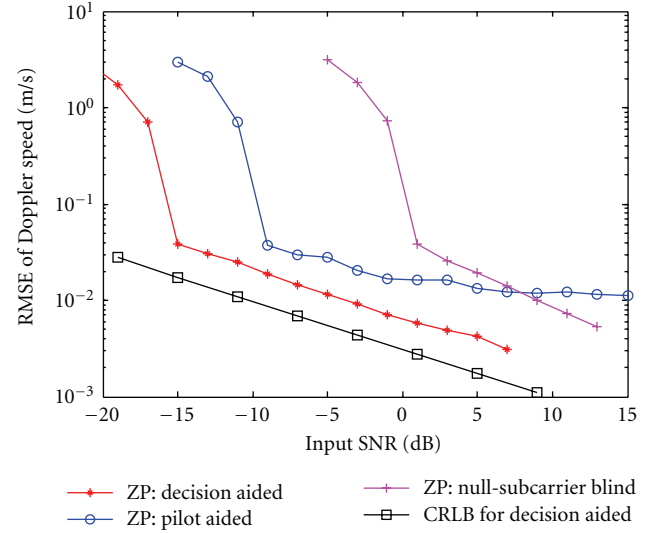


FIGURE 4: Performance of different estimators for ZP-OFDM in single-path channels (channel setting 1). The CRLB with all data known is included as a benchmark.

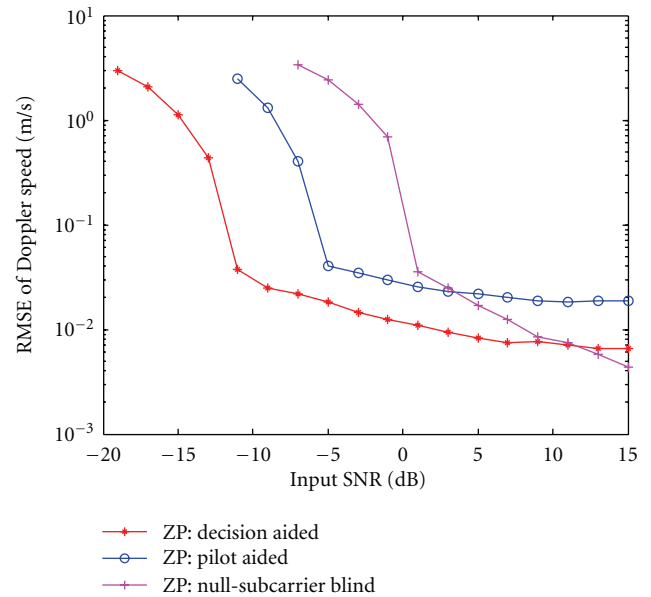


FIGURE 5: Performance of different estimators for ZP-OFDM in multipath channels with a common Doppler scale (channel setting 2).

the capability of the self-correlation method to collect the energy from all paths for Doppler scale estimation, while the cross-correlation method aims to get the Doppler scale estimate from only one path, the strongest path.

**4.2. RMSE Performance with ZP-OFDM.** Figure 4 shows the RMSE performance of three estimation methods for ZP-OFDM in single-path channels. In the low SNR region, one can see that the decision-aided method is the best, while the null-subcarrier-based blind method is the worst. As discussed in Remark 1, the decision-aided method achieves

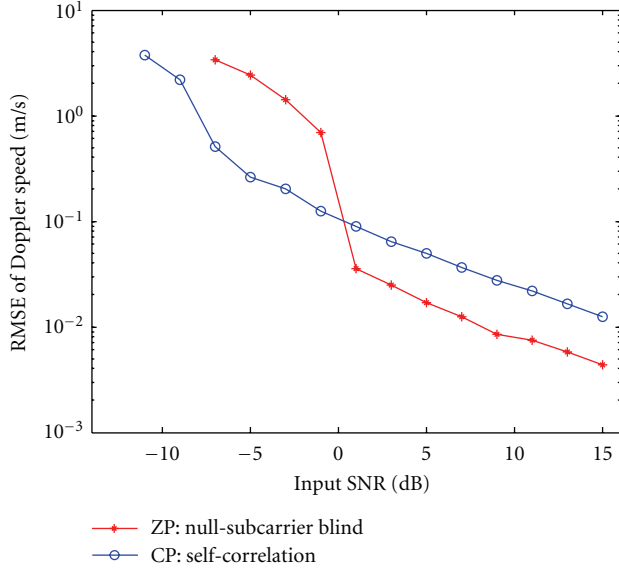


FIGURE 6: Null-subcarrier-based method in ZP-OFDM and CP-OFDM.

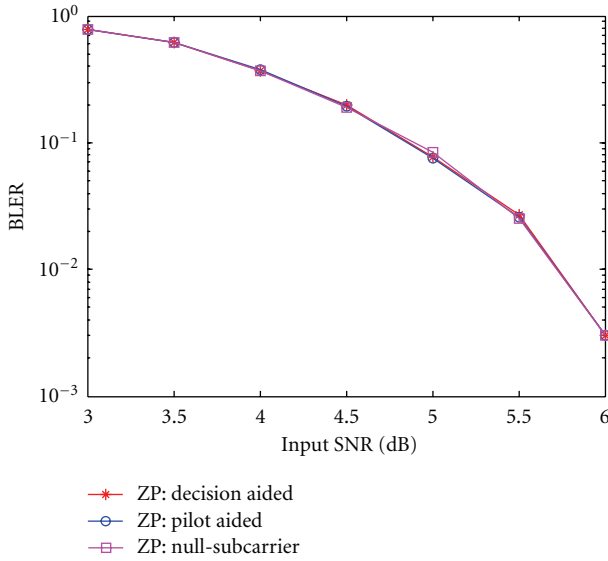


FIGURE 7: The BLER performance in multipath multi-Doppler channels (channel setting 3).

$10\log_{10}(|\mathcal{I}_D| + |\mathcal{I}_P|)/|\mathcal{I}_P| \approx 6$  dB power gain relative to the pilot-aided method. In the medium and high SNR region, the pilot-aided method suffers an error floor due to the interference from the data subcarriers, and the null-subcarrier-based blind method gets a good estimation performance. The Cramer-Rao lower bound (CRLB) with a known waveform is also included as the performance benchmark, whose derivation can be carried out similar to [34, 35].

Figure 5 shows the RMSE performance of three methods in multipath channels with a common Doppler speed. For each realization, the Doppler scale, the path amplitudes, and delays are randomly generated. The RMSE corresponding

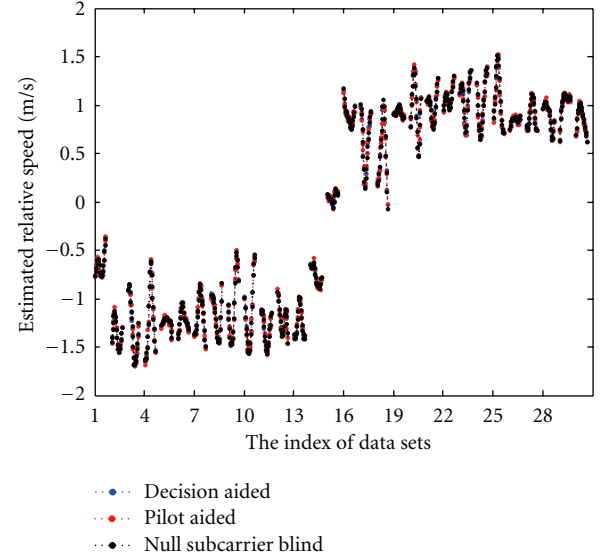


FIGURE 8: MACE10: Estimated Doppler speeds for 30 data bursts in MACE10, where each data burst has 20 OFDM blocks. The time interval between two consecutive data bursts is around 4 mins.

to each method is calculated by averaging the estimation error over multiple realizations. Again, one can see that in the low SNR region, the decision-aided method has the best performance, while the null-subcarrier-based blind method is the worst. Different from the performance in the single-path channel, the decision-aided method has an error floor in the high SNR region, since it only picks up the maximum correlation peak of one path. On the other hand, the null-subcarrier method has robust performance in the presence of multiple paths.

4.3. *Comparison of Blind Methods of CP- and ZP-OFDM.* The self-correlation method for the CP-OFDM preamble is closely related to the null-subcarrier-based blind method for ZP-OFDM. This can be easily verified by rewriting (2) as

$$x_{cp}(t) = \sum_{k=-K_0}^{K_0-1} d'[k] e^{j2\pi(k/(2T_0))t} q(t), \quad t \in [-T_{cp}, 2T_0], \quad (21)$$

where  $d'[k] = 0$  when  $k$  is odd and  $d'[k] = d[k/2]$  when  $k$  is even. The cyclic repetition pattern in is generated by placing zeros on all odd subcarriers in a long OFDM symbol of duration  $2T_0$ . Hence, the self-correlation implementation could be replaced by the null-subcarrier-based implementation for the CP-OFDM preamble.

Figure 6 shows the performance comparison between the blind method for ZP-OFDM and that for CP-OFDM in the multipath channel with one Doppler scale factor, respectively. At low SNR, typically when it's lower than 0 dB, the null-subcarrier-based method in CP-OFDM system has a better performance than that in the ZP-OFDM system, which is due to the fact that CP-OFDM system has 512 null subcarriers, more than 96 null subcarriers in the ZP-OFDM

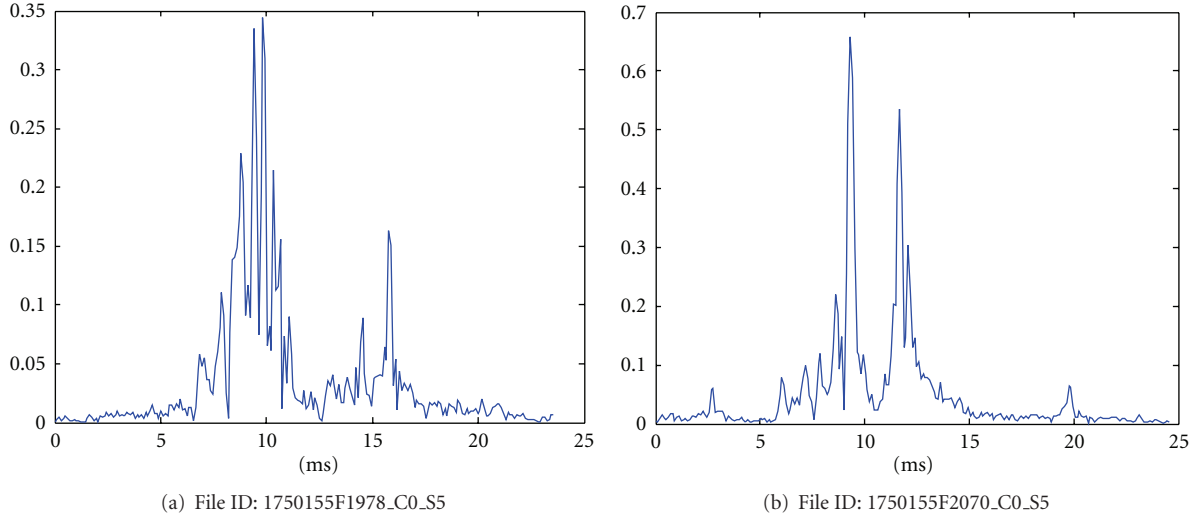


FIGURE 9: Estimated channel impulse responses for two different blocks at different bursts.

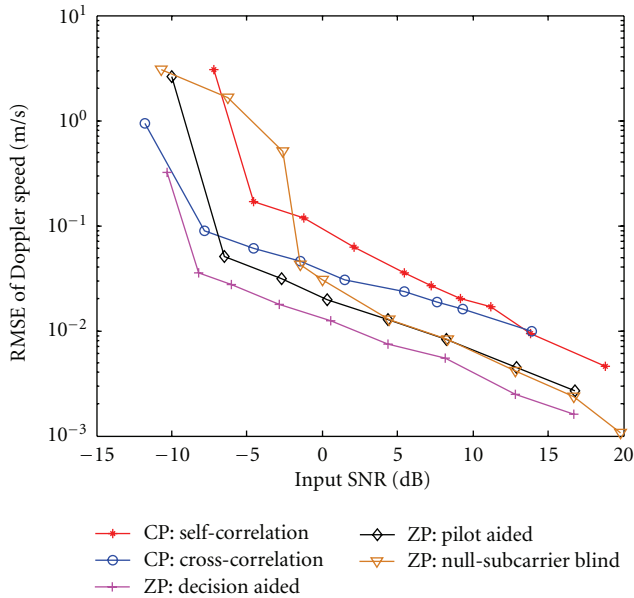


FIGURE 10: MACE10: Performance comparison of Doppler estimation approaches, file ID: 1750155F1954\_C0\_S5.

block. At high SNR, the null-subcarrier-based method in ZP-OFDM has better performance. The possible reason is that null subcarriers in ZP-OFDM are distributed with an irregular pattern, which could outperform the regular pattern in the CP-OFDM preamble.

**4.4. BLER Performance with ZP-OFDM.** With channels generated according to the channel setting 3, Figure 7 shows the simulated BLER performance, where the received OFDM blocks are resampled with the Doppler scale estimates from different estimators and processed using the receiver from [4] and the LDPC decoder from [33]. At each SNR point, at least 20 block errors are collected.

It is expected that the OFDM system can only work when the useful signal power is above that of the ambient noise. Regarding the simulation results in Figure 5, one can see that all the methods can reach a RMSE lower than 0.1 m/s. Hence, it is not surprising that these methods lead to quite similar BLER results as shown in Figure 7. This observation is consistent with the analysis in [29] that an estimation error of 0.1 m/s introduces a negligible error.

## 5. Experimental Results

This *mobile acoustic communication experiment* (MACE10) was carried out off the coast of Martha's Vineyard, Massachusetts, June, 2010. The water depth was about 80 meters. The receiving array was stationary, while the source was towed slowly away from the receiver and then towed back, at a speed around 1 m/s. The relative distance of the transmitter and the receiver changed from 500 m to 4.5 km. Out of the two tows in this experiment, we only consider the data collected in the first tow. There are 31 transmissions in total, with a CP-OFDM preamble and 20 ZP-OFDM blocks in each transmission. We exclude one transmission file recorded during the turn of the source, where the SNR of the received signal is quite low.

The CP-OFDM and ZP-OFDM parameters and signal structures are identical to that in the simulation, as listed in Table 1.

Figure 8 shows the estimated Doppler speeds for ZP-OFDM blocks from different methods. Clearly, the Doppler speed fluctuates from block to block. Figure 9 shows the estimated channel impulse responses for two ZP-OFDM blocks from two data sets, where the time interval between these two data bursts is more than 1 hour. The channels have a delay spread about 20 ms but with different delay profiles.

Based on the recorded files, we carried out two tests.

(A) *Test Case 1.* In this test, we focus on one single file (file ID: 1750155F1954\_C0\_S5) and compare the RMSE performance of different approaches by adding artificial

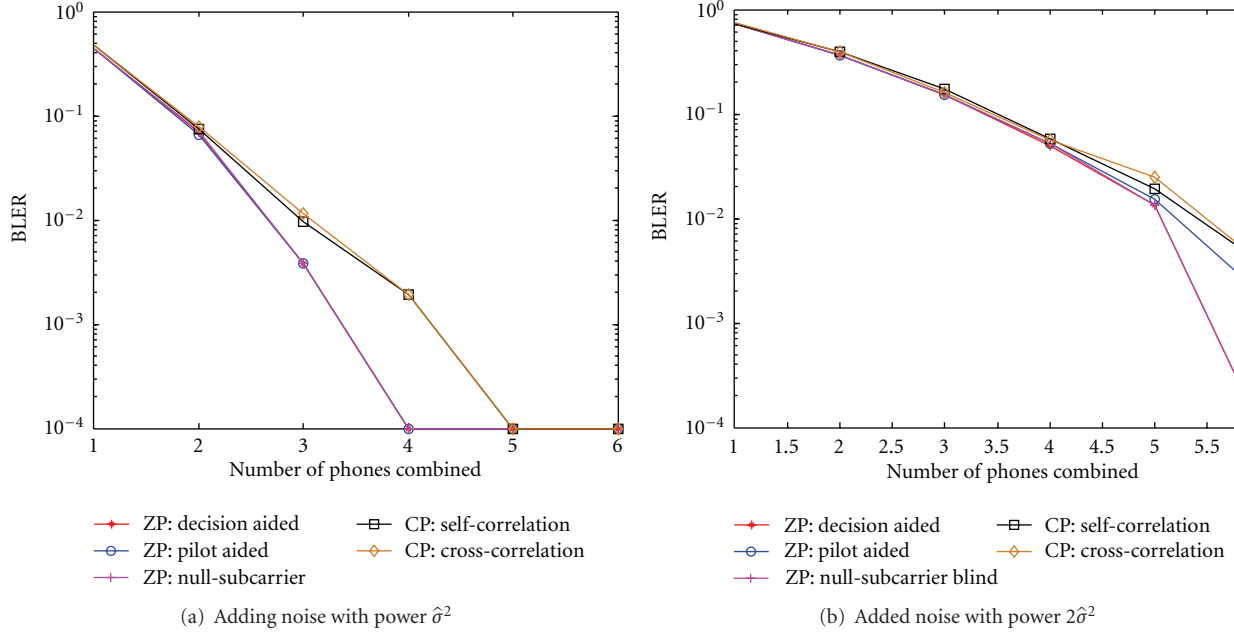


FIGURE 11: MACE10: BLER Performance using different Doppler estimation methods by adding artificial noise to the received signal,  $\hat{\sigma}^2$  denoting the estimated ambient noise power.

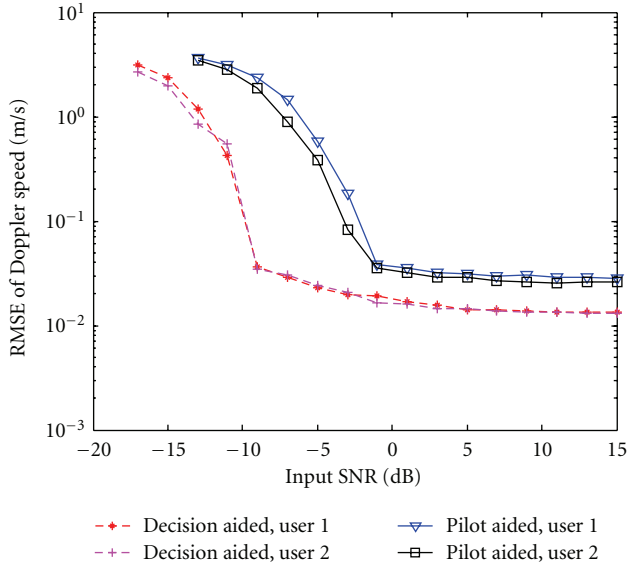


FIGURE 12: Pilot- and decision-aided Doppler scale estimation in a distributed two-user ZP-OFDM system.

noise to the recorded signal. The ground truth of the Doppler scale factor is not available. When computing the RMSE using (20) for each method, we use the estimated Doppler scale of the original file without adding the noise as the ground truth. Figure 10 shows the estimation performance of several approaches. Similar observations as the simulation results in Figures 3 and 5 are found.

(B) *Test Case 2.* In this test, we compare the BLER performance of an OFDM receiver where the resampling operation is carried out with different Doppler scale estimates from different methods.

Due to the relatively high SNR of the recorded signal, we create a semiexperimental data set by adding white Gaussian noise to the received signal. Define  $\hat{\sigma}^2$  as the estimated ambient noise power in the original recorded signal. Figure 11 shows the BLER performance with different Doppler estimation approaches by adding different amount of noises to the received files.

One can see that the methods for ZP-OFDM outperform the methods for CP-OFDM, as the Doppler scale itself is continuously changing from block to block, as illustrated in Figure 8. Another interesting observation is that the null-subcarrier-based blind method has slight performance improvement relative to the pilot- and decision-aided methods. This agrees with the simulation results in Figure 5 that in the high SNR region, the blind estimation method does not suffer an error floor in the multipath channel, hence enjoys a better estimation performance.

## 6. Extension to Distributed MIMO-OFDM

If the transmitters in a multi-input multi-output (MIMO) system are co-located, the Doppler scales corresponding to all transmitters are similar, and hence a single-user blind Doppler scale estimation method would work well, as done in [10]. However, if the transmitters are distributed, for example in a system with multiple single-transmitter users, the Doppler scales for different users could be quite different, even with opposite signs [32]. We now investigate the performance of different Doppler scale estimation methods

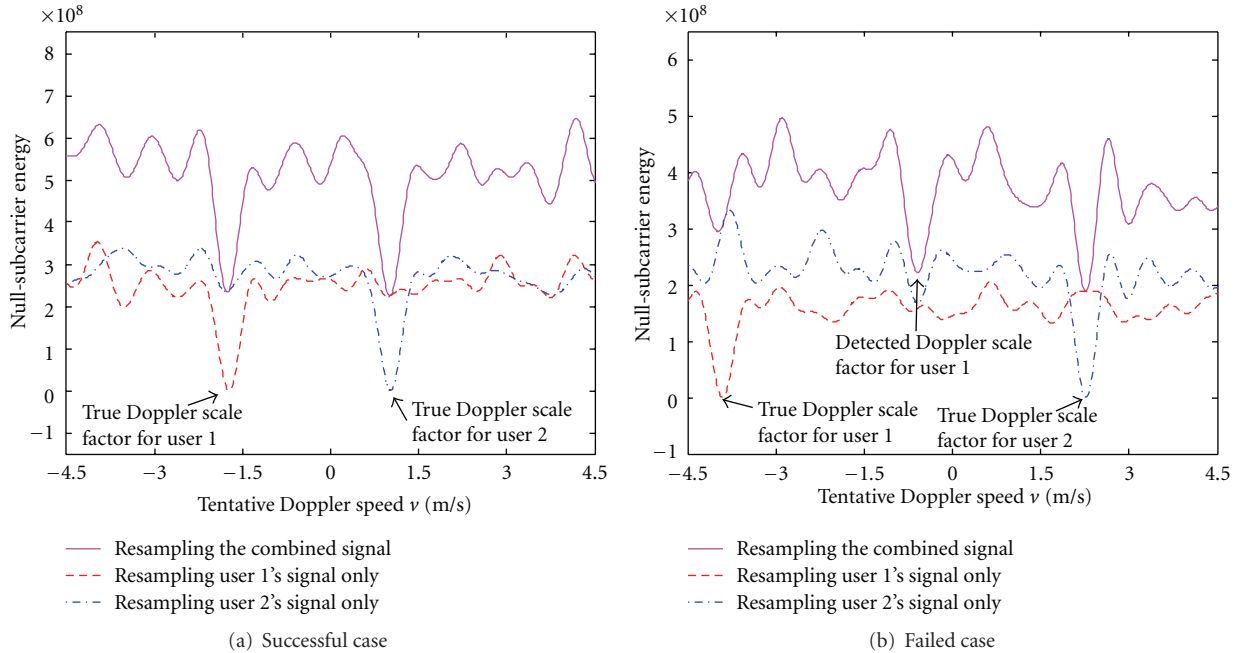


FIGURE 13: Illustration of the objective functions of the null-subcarrier-based method in a two-user system

in the presence of multiuser interference. We will use the ZP-OFDM waveform as the reference design; similar conclusions can be applied to the CP-OFDM preamble. Only simulated data sets are used in the following tests.

**6.1. Pilot- and Decision-Aided Estimation.** We simulate a two-user system. Each user generates a multipath channel according to channel setting 2 independently. The positions of pilot, null, and data subcarriers are the same for different users. The pilot and data symbols of different users are randomly generated and hence are different.

Figure 12 depicts the RMSE performance of the pilot- and decision-aided estimation methods. Compared with the performance in the single-user setting in Figure 5, there is performance degradation and the error floors are higher. However, both methods can achieve RMSE lower than 0.1 m/s at low SNR values. Hence, both methods have robust performance in the presence of multiuser interference.

**6.2. Null-Subcarrier-Based Blind Estimation.** The null-subcarrier-based blind estimation method exploits the transmitted OFDM signal structure. Since all the users share the same positions of null subcarriers, there is a user-association problem even when multiple local minimums are found. We simulate a two-user system where the Doppler speeds of user 1 and user 2 are uniformly distributed within  $[-4.5, -0.5]$  m/s and  $[0.5, 4.5]$  m/s, respectively. *Without adding the ambient noise to the received signal*, Figure 13 demonstrates both successful and failed cases using the objective function in (12). The objective functions in the single-user settings are also included for comparison. One can see that the multiuser interference degrades the estimation performance significantly. Hence, although the blind method developed

for the single user case can be used to colocated MIMO-OFDM as in [10], it is not applicable to distributed MIMO-OFDM where different users have different Doppler scales.

## 7. Conclusion

This paper compared different methods for Doppler scale estimation for a CP-OFDM preamble followed by ZP-OFDM data transmissions. Blind methods utilizing the underlying signalling structure work very well at medium to high SNR ranges, while cross-correlation-based methods can work at low SNR ranges based on the full or partial knowledge of the transmitted waveform. All of these methods are viable choices for practical OFDM receivers. In a distributed multiuser scenario, cross-correlation approaches are more robust against multiuser interference than blind methods.

## Acknowledgments

This work is supported by the ONR Grant N00014-09-1-0704 (PECASE) and the NSF Grant ECCS-1128581. The authors thank Dr. Lee Freitag and his team for conducting the MACE10 experiment.

## References

- [1] I. F. Akyildiz, D. Pompili, and T. Melodia, "Challenges for efficient communication in underwater acoustic sensor networks," *ACM SIGBED Review*, vol. 1, no. 1, pp. 3–8, 2004.
- [2] J.-H. Cui, J. Kong, M. Gerla, and S. Zhou, "The challenges of building scalable mobile underwater wireless sensor networks for aquatic applications," *IEEE Network*, vol. 20, no. 3, pp. 12–18, 2006.

- [3] M. Stojanovic, "Low complexity OFDM detector for underwater acoustic channels," in *OCEANS 2006*, usa, September 2006.
- [4] B. Li, S. Zhou, M. Stojanovic, L. L. Freitag, and P. Willett, "Multicarrier communication over underwater acoustic channels with nonuniform Doppler shifts," *IEEE Journal of Oceanic Engineering*, vol. 33, no. 2, pp. 198–209, 2008.
- [5] F. Qu and L. Yang, "Basis expansion model for underwater acoustic channels?" in *OCEANS 2008*, can, September 2008.
- [6] T. Kang and R. A. Iltis, "Iterative carrier frequency offset and channel estimation for underwater acoustic OFDM systems," *IEEE Journal on Selected Areas in Communications*, vol. 26, no. 9, Article ID 4686804, pp. 1650–1661, 2008.
- [7] G. Leus and P. A. Van Walree, "Multiband OFDM for covert acoustic communications," *IEEE Journal on Selected Areas in Communications*, vol. 26, no. 9, Article ID 4686805, pp. 1662–1673, 2008.
- [8] P. A. V. Walree and G. Leus, "Robust underwater telemetry with adaptive turbo multiband equalization," *IEEE Journal of Oceanic Engineering*, vol. 34, no. 4, Article ID 5299204, pp. 645–655, 2009.
- [9] A. Abdi and H. Guo, "A new compact multichannel receiver for underwater wireless communication networks," *IEEE Transactions on Wireless Communications*, vol. 8, no. 7, pp. 3326–3329, 2009.
- [10] B. Li, J. Huang, S. Zhou et al., "MIMO-OFDM for high-rate underwater acoustic communications," *IEEE Journal of Oceanic Engineering*, vol. 34, no. 4, Article ID 5290161, pp. 634–644, 2009.
- [11] C. R. Berger, S. Zhou, J. C. Preisig, and P. Willett, "Sparse channel estimation for multicarrier underwater acoustic communication: from subspace methods to compressed sensing," *IEEE Transactions on Signal Processing*, vol. 58, no. 3, pp. 1708–1721, 2010.
- [12] P. Ceballos and M. Stojanovic, "Adaptive channel estimation and data detection for underwater acoustic MIMO-OFDM Systems," *IEEE Journal of Oceanic Engineering*, vol. 35, no. 3, Article ID 5530330, pp. 635–646, 2010.
- [13] T. Kang, H. C. Song, W. S. Hodgkiss, and J. Soo Kim, "Long-range multi-carrier acoustic communications in shallow water based on iterative sparse channel estimation," *Journal of the Acoustical Society of America*, vol. 128, no. 6, pp. EL372–EL377, 2010.
- [14] J. Tao, Y. R. Zheng, C. Xiao, and T. C. Yang, "Robust MIMO underwater acoustic communications using turbo block decision-feedback equalization," *IEEE Journal of Oceanic Engineering*, vol. 35, no. 4, Article ID 5634060, pp. 948–960, 2010.
- [15] J. Tao, J. Wu, Y. R. Zheng, and C. Xiao, "Enhanced MIMO LMMSE turbo equalization: algorithm, simulations, and undersea experimental results," *IEEE Transactions on Signal Processing*, vol. 59, no. 8, Article ID 5756490, pp. 3813–3823, 2011.
- [16] K. Tu, D. Fertoni, T. M. Duman, M. Stojanovic, J. G. Proakis, and P. Hursky, "Mitigation of intercarrier interference for OFDM over time-varying underwater acoustic channels," *IEEE Journal of Oceanic Engineering*, vol. 36, no. 2, Article ID 5766772, pp. 156–171, 2011.
- [17] J.-Z. Huang, S. Zhou, J. Huang, C. R. Berger, and P. Willett, "Progressive inter-carrier interference equalization for OFDM transmission over time-varying underwater acoustic channels," *IEEE Journal on Selected Topics in Signal Processing*, vol. 5, no. 8, Article ID 5893908, pp. 1524–1536, 2011.
- [18] H. Wan, R.-R. Chen, J. W. Choi, A. C. Singer, J. C. Preisig, and B. Farhang-Boroujeny, "Markov chain Monte Carlo detection for frequency-selective channels using list channel estimates," *IEEE Journal on Selected Topics in Signal Processing*, vol. 5, no. 8, Article ID 6053992, pp. 1537–1547, 2011.
- [19] A. Song, M. Badiy, V. McDonald, and T. Yang, "Time reversal receivers for high rate multiple-input/multiple-output communication," *IEEE Journal of Oceanic Engineering*, vol. 34, no. 4, pp. 525–538, 2011.
- [20] B. S. Sharif, J. Neasham, O. R. Hinton, and A. E. Adams, "Computationally efficient Doppler compensation system for underwater acoustic communications," *IEEE Journal of Oceanic Engineering*, vol. 25, no. 1, pp. 52–61, 2000.
- [21] S. Yerramalli and U. Mitra, "Optimal resampling of OFDM signals for multiscale-multilag underwater acoustic channels," *IEEE Journal of Oceanic Engineering*, vol. 36, no. 1, Article ID 5732766, pp. 126–138, 2011.
- [22] J. R. Klauder, A. C. Price, S. Darlington, and W. J. Albersheim, "The theory and design of chirp radars," *Bell System Technical Journal*, vol. 39, pp. 745–808, 1960.
- [23] S. Kramer, "Doppler and acceleration tolerances of high-gain, wideband linear FM correlation sonars," *Proceedings of the IEEE*, vol. 55, no. 5, pp. 627–636, 1967.
- [24] J. J. Kroszczyński, "Pulse compression by means of linear-period modulation," *Proceedings of the IEEE*, vol. 57, no. 7, pp. 1260–1266, 1969.
- [25] T. Yang, "Underwater telemetry method using Doppler compensation," U.S. Patent 6512720, 2003.
- [26] J. P. Costas, "A study of a class of detection waveforms having nearly ideal range-Doppler ambiguity properties," *Proceedings of the IEEE*, vol. 72, no. 8, pp. 996–1009, 1984.
- [27] J. G. Proakis, *Digital Communications*, McGraw-Hill, New York, NY, USA, 4th edition, 2001.
- [28] R. Frank, S. Zadoff, and R. Heimiller, "Phase shift pulse codes with good periodic correlation properties (corresp.)," *IRE Transactions on Information Theory*, vol. 8, no. 6, pp. 381–382, 1962.
- [29] S. F. Mason, C. R. Berger, S. Zhou, and P. Willett, "Detection, synchronization, and doppler scale estimation with multicarrier waveforms in underwater acoustic communication," *IEEE Journal on Selected Areas in Communications*, vol. 26, no. 9, Article ID 4686803, pp. 1638–1649, 2008.
- [30] H. Yan, L. Wan, S. Zhou et al., "DSP based receiver implementation for OFDM acoustic modems," *Physical Communication*, vol. 5, no. 1, pp. 22–32, 2012.
- [31] X. Ma, C. Tepedelenlioglu, G. B. Giannakis, and S. Barbarossa, "Non-data-aided carrier offset estimators for OFDM with null subcarriers: identifiability, algorithms, and performance," *IEEE Journal on Selected Areas in Communications*, vol. 19, no. 12, pp. 2504–2515, 2001.
- [32] K. Tu, T. M. Duman, J. G. Proakis, and M. Stojanovic, "Cooperative MIMO-OFDM communications: receiver design for Doppler-distorted underwater acoustic channels," in *Proceedings of the 44th Asilomar Conference on Signals, Systems and Computers (Asilomar '10)*, pp. 1335–1339, Pacific Grove, Calif, USA, November 2010.
- [33] J. Huang, S. Zhou, and P. Willett, "Nonbinary LDPC coding for multicarrier underwater acoustic communication," *IEEE Journal on Selected Areas in Communications*, vol. 26, no. 9, Article ID 4686807, pp. 1684–1696, 2008.

- [34] B. Friedlander, "On the Cramer- Rao bound for time delay and Doppler estimation (corresp.)," *IEEE Transactions on Information Theory*, vol. 30, no. 3, pp. 575–580, 1984.
- [35] X. X. Niu, "Wavelet based approach for joint time delay and doppler stretch measurements," *IEEE Transactions on Aerospace and Electronic Systems*, vol. 35, no. 3, pp. 1111–1119, 1999.